IPP-Report

Max-Planck-Institut für Plasmaphysik

Christian Vogel

Statistische Eigenschaften kompressibler hydrodynamischer und magnetohydrodynamischer Turbulenz

Statistical properties of compressible hydrodynamics and magnetohydrodynamic turbulence

IPP 5/127
April, 2011

TECHNISCHE UNIVERSITÄT MÜNCHEN

Max-Planck-Institut für Plasmaphysik

Statistical properties of compressible hydrodynamic and magnetohydrodynamic turbulence

Christian Vogel

Vollständiger Abdruck der von der Fakultät für Physik der Technischen Universität München zur Erlangung des akademischen Grades eines Doktors der Naturwissenschaften (Dr. rer. nat.) genehmigten Dissertation.

Vorsitzender:		Univ.-Prof. Dr. St. Paul
Prüfer der Dissertation:	1.	Hon.-Prof. Dr. S. Günter
	2.	Univ.-Prof. Dr. A. Burkert

Die Dissertation wurde am 31.05.2010 bei der Technischen Universität München eingereicht und durch die Fakultät für Physik am 01.03.2011 angenommen.

Abstract

In this work, statistical properties of compressible hydrodynamic and magnetohydrodynamic turbulence are studied using direct numerical simulations. The properties of turbulent flows change when average flow velocities within the turbulence exceed the speed of sound in the medium. High flow velocities lead to the formation of shocks, and some of the base assumptions of turbulence theories of incompressible fluids no longer hold. This work presents a systematic study of the influence of flow parameters such as the sonic Mach number and the Alfvén Mach number on low-order statistical properties of isotropic, isothermal turbulence. Numerical results for both non-magnetic and magnetic turbulence are presented and compared to model predictions. In addition, this work suggests a turbulent cascade mechanism that is governed by momentum conservation in compressible turbulence.

Kurzfassung

In dieser Arbeit werden statistische Eigenschaften kompressibler hydrodynamischer und magnetohydrodynamischer Turbulenz mit Hilfe direkter numerischer Simulation untersucht. Die Eigenschaften turbulenter Strömungen ändern sich, wenn die mittlere Flussgeschwindigkeit der turbulenten Fluktuationen die Schallgeschwindigkeit des Mediums übersteigt. Die hohen Flussgeschwindigkeiten führen zur Ausbildung von Stoßwellen. Durch diese Stoßwellen werden einige der grundlegenden Voraussetzungen der existierenden Turbulenztheorien für inkompressible Flüssigkeiten hinfällig. Diese Arbeit beschreibt den Zusammenhang statistischer Eigenschaften der kompressiblen Turbulenz mit Strömungsparametern wie der sonischen Machzahl und der Alfvénischen Machzahl. Die Ergebnisse der numerischen Simulationen werden mit den Vorhersagen einiger, auf kompressible Effekte erweiterter Turbulenzmodelle verglichen. Des Weiteren wird die besondere Rolle der Impulserhaltung in kompressibler Turbulenz im Bezug auf selbstähnliche Skalierung von Spektren untersucht.

CONTENTS

1. INTRODUCTION

In the description of fluids the term turbulence describes a complicated state of motion, strongly irregular in time and space. A snapshot-picture of a turbulent flow reveals spatial structures that are present at all sizes. The time evolution of a turbulent flow appears to be non-deterministic and unpredictable, contradicting with the deterministic rules of classical mechanics. On earth, turbulence is observed mainly in electrically neutral fluids and gases. The air in the earth's atmosphere is in turbulent motion, its irregularity and unpredictability is an every-day challenge to local weather forecasts. The motions of water, whether observed on large scales such as oceanic currents or on smaller scales such as stirred tea water in a mug, are in a turbulent state. Since turbulence in fluids plays an important role, physicists have studied the processes that describe and govern turbulence in neutral fluids for quite some time. The equation describing the motion of a neutral and incompressible fluid, the Navier-Stokes equation, has been known since Navier in 1823. However, the solution to this non-linear partial differential equation is still a conundrum. The break-through findings of Kolmogorov and Obukhov in 1941 provide a means of describing fluid turbulence in a statistical sense.

The properties of turbulent flows change when the fluid or gas is electrically conducting. On earth, examples of electrically conducting fluids in turbulent motion are *e.g.* the outer part of the earth's core or the liquid sodium used as a cooling agent in nuclear fission plants. Electrical conductivity of a medium leads to coupling of magnetic-field fluctuations and velocity-fluctuations. Magnetic fields have considerable effect on the properties of turbulent flows. The statistical properties of incompressible magnetohydrodynamic (MHD) turbulence have been described by phenomenologies presented by Iroshnikov and Kraichnan, Goldreich and Sridhar, and others.

In the universe, it is said that 99% of all visible material is ionized gas. Ionized gas, called plasma, is electrically conducting, and most of this matter is in turbulent motion. Examples for turbulent plasma in the extraterrestrial world range from the sun's convection zone and the solar wind in our solar system to large-scale turbulent plasmas in the interstellar medium (ISM). In the description of extraterrestrial plasma, complications arise due to high flow-velocities, compared to the sound speed in the plasma. Supersonic flows, *i.e.* flows in which the average velocity of turbulent fluctuations is significantly higher than the sound speed in the medium, lead to compression of mass-density in the plasma. The density-fluctuations are genuinely coupled to velocity fluctuations. This coupling of fluctuations is likely to change the statistical properties of turbulence condiderably. In the given examples of extraterrestrial plasma, the turbulent motion can thus not be approximated well by what is known about incompressible flows. Compression alters the flow properties.

The perception of turbulence as the mechanism that governs motions in the interstellar medium over a wide range of spatial scales developed after Crovisier and Dickey discovered a power-spectrum for the brightness distribution of the 21-cm line of H1 emission [15]. The scaling-exponent of the power-spectrum resembled the Kolmogorov scaling exponent of incompressible Navier-Stokes turbulence. At the same time, density-clouds in the ISM were found to have filamentary and criss-crossed structure with little resemblance to expected ballistic and uncorrelated clouds [46]. By the late 1980s, turbulence was considered to be the governing mechanism for compression and star formation in the interstellar medium [52]. However, many physical processes determine the motion and properties of the ISM, such as self-gravity, thermal phases, and chemical processes. This work concentrates on the fluid properties and thus on turbulence in a compressible fluid.

Numerical simulations of the hydrodynamic or magnetohydrodynamic (MHD) equations provide the possibility to observe compressible turbulence in action. Direct numerical simulations have been in use for 40 years. Through technological progress and readily available massively-parallel computers, simulations in three spatial dimensions have become possible. The first simulations of supersonic hydrodynamic turbulence at moderately high resolutions were carried out by Passot, Pouquet and Woodward in 1988 [58]. Magnetic-fields were included in supersonic turbulence simulations by Mac Low *et al.* [47] in 1998, and Padoan and Nordlund in 1999 [56].

This work deals with low-order statistical properties of turbulence in neutral gas and plasma at high flow

velocities. Direct numerical simulations at high spatial resolutions are used to simulate supersonic and super-Alfvénic turbulence in a statistically steady-state. The organization of this work is as follows: In Chapter 2, the fluid equations of hydrodynamics and magnetohydrodynamics are introduced as well as the existing turbulence models. An introduction to the models for incompressible fluid turbulence and incompressible MHD turbulence is provided. In addition, some recent modifications to the theories of incompressible turbulence are outlined. These modifications are efforts to include compressible effects into statistical models of turbulence. The end of Chapter 2 shows some analytical work on the equation of motion of a compressible fluid. This analytical work presents an effort to better understand non-linear energy-transfer processes in compressible hydrodynamic and compressible MHD turbulence, by obtaining observable quantities that capture non-linear energy transfer.
A major part of this work consists of the design and implementation of direct numerical simulation codes. The underlying numerical schemes are outlined in Chapter 3. A part of the numerical work was to combine a shock-capturing scheme for the neutral gas with a magnetic field update-scheme that conserves the solenoidal constraint of the magnetic field. The properties of the simulation codes, tested on 2D and 3D settings, are described in detail in Chapter 4. Before the results of this work's numerical studies are presented, an overview of recent observational results and results from recent numerical experiments is given in Chapter 5.
Finally, Chapter 6 presents the results of statistically-stationary turbulence simulations in the supersonic and super-Alfvénic regime. A systematic approach is taken to test the influence of variations of turbulent flow parameters, such as the average sonic Mach number and the average Alfvén Mach number, on the statistical properties of turbulent flows. The results obtained are compared to current phenomenologic model predictions. In addition, evidence for a momentum-led cascade mechanism that governs power-law behavior of power-spectra in compressible turbulence is outlined.

2. TURBULENCE THEORY

In this Chapter, hydrodynamic and magnetohydrodynamic (MHD) turbulence are introduced, starting with the basic Euler and MHD equations. A brief survey of the theory of incompressible turbulence is provided as a basis for the more complex models of compressible turbulence. Finally, the extensions of the models of incompressible turbulence to compressible turbulence are presented.

2.1 Fluid description

The macroscopic behavior of an electrically conducting plasma in a fixed frame of reference can be described by the MHD fluid approximation. Here, macroscopic behavior means the behavior on time scales and length scales much larger than the intrinsic time and length scales of the microscopic constituents of the plasma. The MHD equations in dimensionless form are (for derivation, see *e.g.* [5]):

$$\frac{\partial \rho}{\partial t} = -\nabla \cdot (\rho \mathbf{v}), \tag{2.1}$$

$$\frac{\partial (\rho \mathbf{v})}{\partial t} = -\nabla \cdot \left(\rho \mathbf{v}\mathbf{v}^T\right) - \nabla(p + \frac{1}{2}\mathbf{B}^2) + \nabla \cdot (\mathbf{B}\mathbf{B}^T) + \mathbf{f} + \nabla \cdot \sigma, \tag{2.2}$$

$$\frac{\partial \mathbf{B}}{\partial t} = \nabla \times (\mathbf{v} \times \mathbf{B}) + \eta \nabla^2 \mathbf{B}, \tag{2.3}$$

$$\frac{\partial e}{\partial t} = \nabla \cdot \left(e + p + \frac{1}{2}\mathbf{B}^2\right) + \nabla \cdot [(\mathbf{v} \cdot \mathbf{B})\mathbf{v}]. \tag{2.4}$$

Here $\mathbf{v}$ is the fluid bulk velocity, ρ is the mass density, and $\mathbf{B}$ is the magnetic field. The force per unit mass $\mathbf{f}$ is an external force that may include gravity or other external forces acting on the fluid. In the last term in the momentum equation (2.2), σ denotes the viscous shear stress tensor $\sigma = \sigma_{ij}^{(\mu)}$, a term that includes the fluid viscosity μ. For a Newtonian fluid, that means for a fluid whose viscosity does not depend on the forces acting on the fluid, the shear stress tensor can be written as:

$$\sigma_{ij}^{(\mu)} = \mu \left[(\partial_i v_j + \partial_j v_i) - \frac{2}{3}\delta_{ij} \nabla \cdot \mathbf{v}\right] \tag{2.5}$$

The induction equation (2.3) contains the magnetic resistivity η.
The internal energy e is connected to the thermal pressure p by an equation of state. In thermal equilibrium, pressure p is computed by:

$$p = (\kappa - 1)\left(e - \frac{1}{2}\rho |\mathbf{v}|^2 - \frac{1}{2}|\mathbf{B}|^2\right), \tag{2.6}$$

with the ratio of specific heats $\kappa = c_p/c_V = (f+2)/f$. The specific heat at constant pressure p is c_p, the specific heat at constant volume is c_V. The ratio of specific heats depends of the degrees of freedom f in a gas. The number of degrees of freedom of an ideal monoatomic gas is three, the resulting ratio of specific heats is thus 5/3.
The MHD equations (2.1)-(2.6) are given in dimensionless form. The position, time, and fields are written in multiples of characteristic length l_0, characteristic velocity v_0, and characteristic density ρ_0. In the dimensionless MHD equations, the kinematic viscosity $\nu = \mu_*/(l_0 v_0 \rho_0)$ and the magnetic resistivity $\eta = \eta_*/(l_0 v_0)$ comprise a special meaning. Here, ν and η are dimensionless quantities derived from dimension containing quantities μ_* and η_*. The parameters $1/\nu$ and $1/\eta$ are referred to as Reynolds number Re and magnetic Reynolds number Rm, respectively. The dimensionless Reynolds number characterizes the relative importance of the non-linear advection term over the viscous term in the momentum equations (2.2). A flow becomes turbulent when the Reynolds number exceeds a certain geometry-dependent critical

value $\mathrm{Re}_{\mathrm{crit}}$, at which point non-linear interactions dominate the flow. Below this critical value, the viscous dampening inhibits turbulence and the flow is called laminar. The magnetic Reynolds number accordingly characterizes the relative importance of the advection term over the resistive term in the magnetic induction equation (2.3). Typical Reynolds numbers in turbulent physical systems range from 10^6 in atmospheric clouds to 10^{13} in the convection zone of the sun (see [63] and [9]). The Reynolds number within the cool part of the interstellar medium is of the order of $10^5 - 10^7$ [22]. A compilation of typical magnetic Reynolds numbers can be found in [11], page 7. The Alfvén number B_0/v_0 is set to unity by a proper choice of B_0. The Alfvén number B_0/v_0 expresses the importance of the Lorentz force compared to advection in equation (2.3). Thus the magnetic field $\mathbf{B}$ is given in units of a reference Alfvén speed $v_{\mathrm{A}} = B_0/(4\pi\rho_0)^{1/2}$.
In dealing with an inviscid neutral fluid, the MHD equations (2.1)-(2.6) can be reduced to the Euler equations by omitting magnetic field contributions. The resulting set of equations is:

$$\frac{\partial \rho}{\partial t} = -\nabla \cdot (\rho \mathbf{v}), \tag{2.7}$$

$$\frac{\partial (\rho \mathbf{v})}{\partial t} = -\nabla \cdot \left(\rho \mathbf{v}\mathbf{v}^T\right) - \nabla p + \mathbf{f}, \tag{2.8}$$

$$\frac{\partial e}{\partial t} = \nabla \cdot (e + p)\,. \tag{2.9}$$

The equation of state simplifies to

$$p = (\kappa - 1)\left(e - \frac{1}{2}\rho\,|\mathbf{v}|^2\right). \tag{2.10}$$

When describing either astrophysical plasma or neutral gases, a barotropic relation of the thermal pressure to the mass density is rather common (see [67], page 64):

$$p(\rho) = K\rho^{\gamma}. \tag{2.11}$$

Here K is a constant and γ is the polytropic index. If the fluid is isothermal, than the polytropic index $\gamma = 1$. In the isothermal limit, temperature fluctuations are annihilated quasi-instantaneously by either perfect thermal conductivity, or by efficient radiation transport. For a perfectly isothermal fluid, the set of equations (2.1)-(2.6) reduce to the isothermal MHD equations:

$$\frac{\partial \rho}{\partial t} = -\nabla \cdot (\rho \mathbf{v}), \tag{2.12}$$

$$\frac{\partial (\rho \mathbf{v})}{\partial t} = -\nabla \cdot \left(\rho \mathbf{v}\mathbf{v}^T\right) - \nabla(p + \frac{1}{2}\mathbf{B}^2) + \nabla \cdot (\mathbf{B}\mathbf{B}^T) + \mathbf{f} + \nabla \cdot \sigma, \tag{2.13}$$

$$\frac{\partial \mathbf{B}}{\partial t} = \nabla \times (\mathbf{v} \times \mathbf{B}) + \eta \nabla^2 \mathbf{B}, \tag{2.14}$$

$$p = c_s^2 \rho. \tag{2.15}$$

The pressure p is a function of the mass density, and c_s is the sound speed.
From the set of isothermal MHD equations, the isothermal Navier-Stokes equations that describe the motions of a neutral isothermal gas are derived by omitting the terms with the magnetic field $\mathbf{B}$:

$$\frac{\partial \rho}{\partial t} = -\nabla \cdot (\rho \mathbf{v}), \tag{2.16}$$

$$\frac{\partial (\rho \mathbf{v})}{\partial t} = -\nabla \cdot \left(\rho \mathbf{v}\mathbf{v}^T\right) - \nabla p + \mathbf{f} + \nabla \cdot \sigma, \tag{2.17}$$

$$p = c_s^2 \rho. \tag{2.18}$$

The set of equations describing isothermal MHD and hydrodynamics have been introduced. Before describing turbulence, some important linear solutions to the given sets of equations are introduced.

2.1.1 Linear solutions

The linearized compressible MHD equations support longitudinal and transverse waves. In this context, the transverse waves are shear Alfvén waves. For a homogeneous plasma with density ρ_0, pressure p_0,

and in a homogeneous magnetic field $\mathbf{B}_0$, a small elastic bending of magnetic field lines perpendicular to the magnetic field propagates along the magnetic field with the Alfvén velocity. The Alfvén velocity v_A in one spatial dimension is given by

$$v_\mathrm{A} = B_0/\sqrt{4\pi\rho_0}. \tag{2.19}$$

Two compressible waves can be distinguished: the fast magnetosonic wave, and the slow magnetosonic wave. In the fast magnetosonic wave, both magnetic field $\mathbf{B}^2$ and the density ρ are compressed, while the changes of $\mathbf{B}^2$ and ρ are in phase. The velocity of the fast magnetosonic wave in one space dimension (*e.g.* the x-direction) is given by

$$v^x_\mathrm{fms} = \frac{1}{2}\sqrt{\frac{c_\mathrm{s}^2+\mathbf{B}^2}{\rho} + \sqrt{\left(\frac{c_\mathrm{s}^2+\mathbf{B}^2}{\rho}\right)^2 - \frac{4B_x^2c_\mathrm{s}^2}{\rho}}}. \tag{2.20}$$

The fast magnetosonic wave is fastest for propagations perpendicular to the magnetic field. For propagation parallel to the magnetic field $\mathbf{B}$, the fast magnetosonic wave merges with the shear Alfvén wave when $v_\mathrm{A} > c_\mathrm{s}$.
In the latter case of the two compressible waves, the changes of $\mathbf{B}^2$ and ρ are exactly opposite in phase. Thus, the velocity of the slow magnetosonic wave propagating in the x-direction is:

$$v^x_\mathrm{sms} = \frac{1}{2}\sqrt{\frac{c_\mathrm{s}^2+\mathbf{B}^2}{\rho} - \sqrt{\left(\frac{c_\mathrm{s}^2+\mathbf{B}^2}{\rho}\right)^2 - \frac{4B_x^2c_\mathrm{s}^2}{\rho}}}. \tag{2.21}$$

In the absence of magnetic fields, the fast magnetosonic wave collapses into the longitudinal sound wave, a small density perturbation that propagates isotropically with the speed of sound. The slow wave vanishes. For an ideal gas, the sound speed is given by

$$c_s = \sqrt{\kappa\frac{p}{\rho}}. \tag{2.22}$$

2.1.2 The incompressible limit

In order to give an introduction to turbulence theory, the incompressible hydrodynamic and MHD equations will be introduced, first. Most of the theory and phenomenology of turbulent dynamics is based on the more simple, incompressible case. The compressible turbulence phenomenologies are based on the findings in the incompressible case.
In the incompressible limit, the mass density of each fluid particle is constant along the fluid particle trajectory, and the polytropic index $\gamma \to \infty$. The MHD equations (2.1)-(2.6) reduce to the coupled equations for momentum and magnetic induction

$$\frac{\partial\mathbf{v}}{\partial t} = -(\mathbf{v}\cdot\nabla)\mathbf{v} - \frac{1}{\rho_0}\nabla p - \mathbf{B}\times(\nabla\times\mathbf{B}) + \mathbf{f} + \nabla\cdot\sigma, \tag{2.23}$$

$$\frac{\partial\mathbf{B}}{\partial t} = \nabla\times(\mathbf{v}\times\mathbf{B}) + \eta\nabla^2\mathbf{B}, \tag{2.24}$$

$$\nabla\cdot\mathbf{v} = 0, \tag{2.25}$$

$$\nabla\cdot\mathbf{B} = 0. \tag{2.26}$$

Both the velocity and the magnetic field are solenoidal. The dissipative term in equation (2.23), that includes the shear stress tensor σ, can be rewritten as $\nu\nabla^2\mathbf{v}$, with the dimensionless kinematic viscosity ν. Thermal pressure p is no longer a dynamical variable but a passive quantity.
A neutral incompressible fluid can be described by dropping the terms that contain the magnetic field $\mathbf{B}$. This yields the incompressible Navier-Stokes equation

$$\frac{\partial\mathbf{v}}{\partial t} = -(\mathbf{v}\cdot\nabla)\mathbf{v} - \frac{1}{\rho_0}\nabla p + \mathbf{f} + \nu\nabla^2\mathbf{v}, \tag{2.27}$$

$$\nabla\cdot\mathbf{v} = 0. \tag{2.28}$$

Several quantities are globally conserved in the inviscid and non-resistive case of the incompressible MHD and Navier-Stokes equations. The ideally conserved quantities, also referred to as quadratic invariants, are the basis for current turbulence phenomenologies and are therefore described next.

2.1.3 Global quadratic invariants

The quadratic-conserved quantities constrain the evolution of the turbulent system. In incompressible ideal MHD with closed or periodic boundary conditions, the total energy is globally conserved in the absence of external forces:

$$E_{\mathrm{tot}} := E_{\mathrm{kin}} + E_{\mathrm{mag}} = \int dV \frac{1}{2}(\mathbf{v}^2 + \mathbf{b}^2). \tag{2.29}$$

The scalar product of the ideal momentum equation with the velocity $\mathbf{v}$, added to the induction equation (2.24) multiplied by $\mathbf{B}$, integrating over all space and using Gauss' Theorem leads to

$$\frac{\partial E_{\mathrm{tot}}}{\partial t} = \frac{\partial}{\partial t} \int dV \frac{1}{2}(\mathbf{v}^2 + \mathbf{b}^2) = 0, \tag{2.30}$$

for suitable boundary conditions. Besides the total energy $\frac{1}{2}\left\langle \mathbf{v}^2 + \mathbf{B}^2 \right\rangle$, the magnetic helicity $H^{\mathrm{M}} := \langle \mathbf{A} \cdot \mathbf{B} \rangle$ (where $\mathbf{A}$ is the magnetic vector potential) and the cross helicity $H^{\mathrm{C}} := \langle \mathbf{v} \cdot \mathbf{B} \rangle$ are globally conserved.
For the incompressible Navier-Stokes case of a neutral fluid, the kinetic energy per unit mass $\frac{1}{2}\left\langle \mathbf{v}^2 \right\rangle$ is globally conserved. Also the kinetic helicity $H^{\mathrm{kin}} := \langle \mathbf{v} \cdot \boldsymbol{\omega} \rangle$, a measure for the asymmetry between the vorticity field $\boldsymbol{\omega} := \nabla \times \mathbf{v}$, and the velocity field $\mathbf{v}$, is conserved.
When viscosity and resistivity are included, the quadratic invariants develop in time. In incompressible MHD, the total energy then decays with the total rate of energy dissipation ϵ given by

$$\epsilon := -\frac{dE}{dt} = \int_V dV(\nu \boldsymbol{\omega}^2 + \eta(\nabla \times \mathbf{B})^2). \tag{2.31}$$

The decay rates of both magnetic helicity H^{M} and the cross helicity H^{C} differ from the decay rate of the total energy. Both ideal invariants are expected to decay more slowly than the total energy (see [5], page 75). In incompressible Navier-Stokes turbulence, the kinetic energy decays with the total rate of dissipation

$$\epsilon := -\frac{dE}{dt} = \int_V dV(\nu \boldsymbol{\omega}^2). \tag{2.32}$$

The incompressible quadratic invariants are not globally conserved in ideal compressible hydrodynamics and MHD. Kinetic and magnetic fluctuations can exchange energy with thermal fluctuations. Compression and shocks heat the gas or plasma. Kinetic energy is thus lost and dissipated into heat. Solenoidal and dilatational velocity-fluctuations can exchange energy and can interact with acoustic and thermal fluctuations. The only quadratic inviscid invariants in compressible hydrodynamics are the mass density $\left\langle (\rho)^2 \right\rangle$ and the momentum density $\left\langle (\rho \mathbf{v})^2 \right\rangle$ [22]. The latter quantity is not positive definite and its role in governing the dynamics of compressible turbulence is an open question.

2.2 Energy equation in spectral space and the energy spectrum

The evolution of a turbulent incompressible flow is most easily understood in Fourier space. When Fourier transforming the incompressible Navier-Stokes equation, the terms with differential operators (∇) turn into algebraic terms. The Fourier components of the transformed quantities can be viewed as excitation levels of scales belonging to a wave vector $\mathbf{k}$ in spectral space. Integrated over all spectral angles and in case of a statistically isotropic flow, this yields the excitations of structures with a wave number k or a spatial magnitude of $l = 2\pi/k$. The distribution of squared excitations over the whole range of wave numbers k is referred to as the power spectrum.
The Fourier transform of the incompressible Navier-Stokes equation (2.27) yields (the transform of the Navier-Stokes equation from real to Fourier space is performed in detail by Lesieur [40])

$$\left(\frac{\partial}{\partial t} + \nu k^2\right) \hat{v}_i(\mathbf{k}) = -\frac{i}{2} P_{ijm}(\mathbf{k}) \int_V \int_V \hat{v}_j(\mathbf{p}) \hat{v}_m(\mathbf{q}) \delta(\mathbf{k} - \mathbf{p} - \mathbf{q}) d^3p \; d^3q. \tag{2.33}$$

The partial time derivative of a component of the Fourier-space velocity field is given by the projection P_{ijm} of the right hand integral. The integral can be interpreted as triads of modes belonging to wave vectors $\mathbf{p}$, $\mathbf{q}$, and $\mathbf{k}$ that interact and exchange energy. The projection tensor P_{ijm} is defined as

$$P_{ijm}(\mathbf{k}) := 2k_m \delta_{ij} - 2k_i \frac{k_j k_m}{k^2}. \tag{2.34}$$

The operator P_{ijm} projects a vector onto the plane perpendicular to the wave vector $\mathbf{k}$ and thus conserves the solenoidality constraint of the incompressible velocity-field. The pressure term $-\nabla p$ provides for this projection, and pressure p is thus eliminated from the equation in Fourier space.
The energy-evolution equation can be derived from (2.33) by constructing the pair correlation function $\left\langle \hat{v}_i(\mathbf{k})\hat{v}_i(\mathbf{k}')\right\rangle$, where $\mathbf{k}' := -\mathbf{k}$, and computing the partial time derivative. The energy-evolution equation of the incompressible Navier-Stokes equation is

$$\left(\frac{\partial}{\partial t} + \nu k^2\right)\left\langle \hat{v}_i(\mathbf{k})\hat{v}_i(\mathbf{k}')\right\rangle = -\frac{1}{2}P_{ijm}(\mathbf{k})\int_V\int_V \mathrm{Im}\left[\langle \hat{v}_i(\mathbf{k})\hat{v}_j(\mathbf{p})\hat{v}_m(\mathbf{q})\rangle\right] d^3p\; d^3q. \tag{2.35}$$

The imaginary part of the triple correlation $\langle\hat{v}\hat{v}\hat{v}\rangle$ is proportional to the Dirac delta function $\delta(\mathbf{k}+\mathbf{p}+\mathbf{q})$. Thus, only triads with $\mathbf{k}+\mathbf{p}+\mathbf{q}=0$ are involved in non-linear energy transfer. From equation (2.35), the ideal conservation of kinetic energy can be derived by integrating over all wave vectors $\mathbf{k}$ in a shell of wave number k:

$$\frac{d}{dt}\int_0^\infty E(k)dk + 2\nu\int_0^\infty k^2E(k)dk = 0. \tag{2.36}$$

Here, $E(k) := \frac{1}{2}\left\langle |v(k)|^2\right\rangle$ is the kinetic energy spectrum. Equation (2.36) shows that the specific kinetic energy is conserved by the nonlinear terms of the Navier-Stokes equations and dissipated by viscous interactions.
In the case of incompressible MHD without a mean magnetic field, the Fourier-transformed momentum and induction equations are (see for example [73]):

$$\left(\frac{\partial}{\partial t} + \nu k^2\right)\hat{v}_i(\mathbf{k}) = -\frac{i}{2}P_{ijm}(\mathbf{k})\int_V\int_V\left[\hat{v}_j(\mathbf{p})\hat{v}_m(\mathbf{q}) - \hat{b}_j(\mathbf{p})\hat{b}_m(\mathbf{q})\right]\delta(\mathbf{k}-\mathbf{p}-\mathbf{q})d^3p\; d^3q, \tag{2.37}$$

$$\left(\frac{\partial}{\partial t} + \eta k^2\right)\hat{b}_i(\mathbf{k}) = -i\bar{P}_{ijm}(\mathbf{k})\int_V\int_V \hat{v}_j(\mathbf{p})\hat{b}_m(\mathbf{q})\delta(\mathbf{k}-\mathbf{p}-\mathbf{q})d^3p\; d^3q, \tag{2.38}$$

where P_{ijm} is defined in (2.34), and $\bar{P}_{ijm} := k_j\delta_{im} - k_m\delta_{ij}$. Like the Navier-Stokes case, only triads of wave vectors lead to a change in the according Fourier components of the fields. In the momentum equation (2.37), the Fourier components of magnetic field fluctuation $\hat{b}_j(\mathbf{p})\hat{b}_m(\mathbf{q})$ can exchange energy with the velocity Fourier component $\hat{v}_i(\mathbf{k})$, when the three wave vectors $\mathbf{p}$, $\mathbf{q}$, and $\mathbf{k}$ form a triangle. The temporal changes of the magnetic field components in (2.38) are caused by interactions with modes $\hat{v}_j(\mathbf{p})\hat{b}_m(\mathbf{q})$.
The according energy evolution equations are constructed analogously to the neutral fluid case, from the pair correlation functions $\left\langle \hat{v}_i(\mathbf{k})\hat{v}_i(\mathbf{k}')\right\rangle$ and $\left\langle \hat{b}_i(\mathbf{k})\hat{b}_i(\mathbf{k}')\right\rangle$. From the resulting set of energy evolution equations, it can be shown that the total energy $E_{\mathrm{tot}}(k) := \frac{1}{2}\left\langle v^2(k)\right\rangle + \frac{1}{2}\left\langle b^2(k)\right\rangle$ is conserved by the nonlinear energy transfer.

2.3 Turbulence phenomenologies

Turbulence phenomenologies are usually closely linked to quadratic invariants. Quadratic invariants set the constraints for the evolution of the system, such as energy conservation. They provide physical arguments for the explanation of the statistical ensemble behavior of turbulence within a certain range of spatial scales. In incompressible turbulent flows, kinetic energy at large spatial scales is transfered to smaller and smaller spatial scales. At sufficiently high Reynolds numbers, large structures become unstable and energetically less favorable. They break up into smaller structures and thus transfer their energy subsequently to smaller and smaller structures. This phenomenon is referred to as the Richardson cascade. At the smallest scales, kinetic energy is dissipated by viscous interaction and transformed into heat. For scales much larger than dissipative scale lengths, kinetic energy is almost globally conserved.

2.3.1 The Kolmogorov scaling prediction

Based on the Richardson cascade, a phenomenological model for incompressible Navier-stokes turbulence was suggested by Kolmogorov [33]. The statistical ensemble behavior of turbulent fluctuations within the range of conserved kinetic energy can be described by the Kolmogorov phenomenology (see *e.g.* [26]).

Kolmogorov's hypotheses includes that turbulent structures of sizes that are larger than those affected by viscous dissipation, but smaller than scales that are affected by the physical boundary conditions, reveal a universal statistical form, a function of the size of the turbulent structure. Those spatial scales are called inertial range. At a given turbulent structure of size l and velocity v_l, the rate of change of kinetic energy is proportional to v_l^2 divided by the characteristic time scale. The characteristic time scale is the time it takes the fluctuation at scale l to transfer its energy, and is assumed to be the cascade time scale $\tau_{\text{cas}} := l/v_l$. This leads to the following dimensional considerations based on the total rate of dissipation ϵ

$$\epsilon \sim \frac{v_l^2}{\tau_{\text{cas}}} \sim \frac{v_l^3}{l}, \tag{2.39}$$

$$\rightarrow v_l \sim (\epsilon l)^{1/3}. \tag{2.40}$$

The total rate of dissipation has the dimensions $[\epsilon] = [l^2]/[t^3]$. The eddy energy v_l^2 is related to the energy spectrum as

$$v_l^2 \sim kE(k), \rightarrow v_l \sim l^{-1/2}E^{1/2}(k), \tag{2.41}$$

where k is the wave number related to the structure of size l by $k = 2\pi/l$. The energy spectrum has dimensions $[E_k] = [l^3]/[t^2]$. A combination of the scaling relations (2.40) and (2.41) yields a scaling for the energy

$$E^{1/2}(k) \sim \epsilon^{1/3} l^{5/6}. \tag{2.42}$$

By taking the square of relation (2.42) and introducing a constant C_{K}, the Kolmogorov constant, the Kolmogorov scaling relation for the kinetic energy spectrum is obtained

$$E(k) = C_{\text{K}} \epsilon^{2/3} k^{-5/3}. \tag{2.43}$$

The Kolmogorov energy spectrum (2.43) predicts a universal scaling-law for the excitation levels of kinetic energy in the inertial range of Navier-Stokes turbulence. The constant C_{K} was experimentally found to be of the order of 1.6. The universal scaling behavior of the kinetic energy spectrum in the inertial range has been verified in many experiments on turbulent systems (for an overview, see [68]). For wave numbers above a certain wave number k_{d}, called the Kolmogorov wave number, viscous dissipation dampens the turbulent eddies and the energy spectrum drops rapidly. The range of wave numbers above k_{d} is referred to as the dissipation range because dissipative forces dominate over inertial forces (see *e.g.* [26], page 91). The wave number k_{d} is defined as the scale at which the dissipation rate is equal to the non-linear transfer rate. The Kolmogorov wave number k_{d} is obtained by combining the Kolmogorov energy spectrum (2.43) and the definition of the total rate of dissipation (2.36):

$$k_{\text{d}} = \left(\frac{\epsilon}{\nu^3}\right)^{1/4}. \tag{2.44}$$

Besides the prediction for power-law behavior of the energy spectrum, the Kolmogorov theory entails a prediction for structure functions of velocity-increments. The longitudinal structure function of the p-th order is defined as the root-mean-square (RMS) of velocity increments as a function of longitudinal displacement l, to the power of p (see *e.g.* [26]):

$$S_p(l) := \left\langle [\delta v_{\parallel}]^p \right\rangle, \qquad \text{with } \delta v_{\parallel} = [\mathbf{v}(\mathbf{x}+\mathbf{l}) - \mathbf{v}(\mathbf{x})] \cdot \mathbf{l}/l. \tag{2.45}$$

The assumption of self-similarity is the assumption that in the infinite Reynolds-number limit all small-scale statistical properties are uniquely determined by the scale l and the total rate of dissipation ϵ. Through dimensional analysis, the scaling properties of longitudinal structure functions with the displacement l are obtained:

$$S_p(l) \sim (\epsilon l)^{p/3}. \tag{2.46}$$

For the 3rd order structure function $S_3(l)$, an exact scaling prediction can be derived using the Kármán-Howarth-Monin-relation (see [26]):

$$S_3(l) = -\frac{4}{5}\epsilon l. \tag{2.47}$$

This exact result is called the 4/5th law. The scaling relation of the velocity structure functions, measured both experimentally and in numerical simulations, deviates from the scaling relation (2.46). This deviance becomes marked at higher orders ([1]). This can be explained by the intermittent character of turbulence. Intermittency describes the spatial (or temporal) inhomogeneity of *e.g.* energy dissipation rate, vorticity, or other flow observables. Spatial and temporal inhomogeneity of turbulence contradicts with the hypothesis of self-similarity. Various models have been suggested to reflect the intermittent character of turbulence (see [26], pages 127-194).

2.3.2 The Iroshnikov-Kraichnan scaling prediction

For incompressible MHD turbulence, the influence of the magnetic field and the according Alfvén waves change the scaling properties of the inertial range. Small-scale fluctuations are affected by locally larger-scale magnetic fields. Small-scale fluctuations can be regarded as shear-Alfvén waves that interact with shear-Alfvén waves moving in the opposite direction along the larger-scale magnetic field-lines. During this interaction time, the Alfvén-waves scatter. The non-linear terms represent the coupling of the interacting Alfvén wave-packages. The coupling strength is determined by the ratio of the strength of the small-scale fluctuations over the locally mean velocity-field strength and magnetic-field strength, experienced by the small-scale fluctuations. This ratio is small. The interaction time is the Alfvén time $\tau_{\mathrm{A}} := l/v_{\mathrm{A}}$, where v_{A} is the Alfvén velocity defined in equation (2.19). The Alfvén time τ_{A} is shorter than the eddy-eddy interaction time τ_{cas} that is applied in the non-magnetic case. That is due to the fact that the interaction time is proportional to the inverse of the propagation speed of interacting Alfvén waves. Thus the interaction time is proportional to the inverse of kB_0, where B_0 is the local mean magnetic field experienced by the smaller scale Alfvén waves. Iroshnikov [31] and Kraichnan [35] introduced the according energy-transfer time in the magnetic case

$$\tau_{\mathrm{cas}}^{\mathrm{IK}} \sim (\tau_l)^2/\tau_{\mathrm{A}}. \tag{2.48}$$

The energy flux across the inertial range is assumed to be constant, so that the total rate of dissipation associated with the spectral energy is

$$E(k)/\tau_{\mathrm{cas}}^{\mathrm{IK}}(k) \sim \epsilon. \tag{2.49}$$

Combining equations (2.48) and (2.49) yields a prediction for the incompressible MHD energy spectrum

$$E(k) \sim C_{\mathrm{IK}}(\epsilon v_{\mathrm{A}})^{1/2} k^{-3/2}. \tag{2.50}$$

The Iroshnikov-Kraichnan scaling relation for the total energy is flatter than the Kolmogorov spectral-scaling due to the factor τ_l/τ_{A}. In contrast to the Kolmogorov energy spectrum, the Iroshnikov-Kraichnan total-energy spectrum is not a universal function of the total rate of dissipation, but also depends on the macroscopic magnetic field. The IK scaling prediction for the total-energy spectrum has been found to apply to 2D-MHD turbulence in direct numerical simulations [6]. However, in three dimensional MHD turbulence, the IK scaling-law has not been verified unambiguously by experiment or numerical simulation. One of the weaknesses of this model is the assumption of isotropy, since locally large-scale magnetic-field structures lead to local anisotropy.

2.3.3 The Goldreich-Sridhar scaling prediction

Shebalin *et al.* [64] found in 2D numerical simulations of incompressible MHD turbulence that, with or without a mean magnetic field, an initially isotropic distribution of excitations is rendered anisotropic due to a difference in energy-transfer processes in directions parallel and perpendicular to a mean magnetic-field orientation, associated with the fluctuation. The local anisotropy in initially globally isotropic turbulence, due the difference in the energy-transfer mechanism, gave rise to an alternative way of predicting an inertial-range scaling-law for the total energy.
Goldreich and Sridhar [29], [69] were the first to distinguish between the parallel and perpendicular extent ($l_\perp$ and $l_\parallel$) of an eddy of size l with regard to the orientation of the wave vector associated with the mean magnetic-field orientation experienced by this eddy. The spatial extent of the eddy perpendicular to the magnetic wave vector shrinks due to the turbulent energy transfer to smaller perpendicular scales. For the parallel component, the process of turbulent transport of energy to smaller scales is reduced. This

effect leads to a stretching of eddies in the course of the cascade process, until a critical balance of stretching is reached. For the perpendicular component of turbulent MHD fluctuations, the Goldreich-Sridhar phenomenology predicts the inertial-range scaling-law of the energy spectrum to be

$$E_{k_\perp} \sim \epsilon^{2/3} k_\perp^{-5/3}. \tag{2.51}$$

The energy spectrum for the parallel component is

$$E_{k_\parallel} \sim \epsilon v_{\mathrm{A}}^{-1} k_\parallel^{-2}. \tag{2.52}$$

The energy spectrum for the parallel component follows from the one for the perpendicular component by the critical balance condition $k_\parallel E_{k_\parallel} \sim k_\perp E_{k_\perp}$ and $l_\parallel \sim l_\perp^{2/3}$. There is today widespread agreement that, in globally isotropic MHD turbulence, the inertial-range scaling is dominated by the perpendicular part of the Goldreich-Sridhar scaling-law. The scaling exponent of the Goldreich-Sridhar prediction thus agrees with the Kolmogorov scaling-law of equation (2.43). The scaling law of total energy for the inertial-range dynamics of incompressible MHD turbulence, subject to a strong mean magnetic field, remains a point of contention in the field.

2.3.4 Scaling prediction for the residual energy

The difference between the magnetic energy and the kinetic energy is called residual energy. Although the residual energy is not ideally conserved in incompressible MHD turbulence, it is observed to follow a power law in the inertial range [5]. The residual energy is defined as

$$E_{\mathrm{res}} = \int_V dV \frac{1}{2} |\mathbf{v}^2 - \mathbf{b}^2|. \tag{2.53}$$

At small scales, the velocity fluctuations and the magnetic fluctuations are expected to reach equipartition, *i.e.* comparable levels of excitation of the squared velocity fluctuations and the magnetic fluctuations. For spatial scales larger than the dissipative scales, the residual spectrum reflects a balance of local to non-local energy transfer within the MHD turbulence. From dimensional arguments, the balance of local and non-local energy transfer leads to a power-law prediction for the residual-energy spectrum of the form ([5], page 106):

$$E_{\mathrm{res}}(k) \sim (\epsilon / v_{\mathrm{A}}) k^{-2}. \tag{2.54}$$

However, Müller and Grappin [50] propose a scaling relation of the residual-energy spectrum with the kinetic-energy spectrum, so that $E_{\mathrm{res}}(k) \sim k E_{\mathrm{kin}}^2(k)$. In isotropic MHD turbulence, this leads to a prediction of the residual-energy spectrum that is steeper than that of equation (2.54) :

$$E_{\mathrm{res}}(k) \sim k^{-7/3}. \tag{2.55}$$

In high-resolution numerical experiments, Müller and Grappin [50] obtained a scaling exponent for the residual energy spectrum that agrees with the prediction of 7/3.

2.4 Effects of compressibility

The assumption of incompressibility in turbulent flows of neutral fluids is valid, when the RMS velocity is significantly smaller than the sound speed. The sonic Mach number $\mathcal{M}_{\mathrm{s}}$ is a measure of compressibility, here defined as the RMS velocity over the sound speed:

$$\mathcal{M}_{\mathrm{s}} := \frac{\langle \mathbf{v}^2 \rangle^{\frac{1}{2}}}{c_{\mathrm{s}}} \tag{2.56}$$

The incompressible limit in neutral turbulence corresponds to $\mathcal{M}_{\mathrm{s}} \ll 1$. In MHD, the incompressible limit is valid where both the sonic Mach number and the Alfvén Mach number, defined as

$$\mathcal{M}_{\mathrm{A}} := \frac{\langle \mathbf{v}^2 \rangle^{\frac{1}{2}}}{v_{\mathrm{a}}}, \tag{2.57}$$

are considerably smaller than one. For turbulent flows with $\mathcal{M}_\mathrm{s} \geq 1$ and/or $\mathcal{M}_\mathrm{A} \geq 1$, compressible effects must be taken into account.
In compressible flows, the velocity field can be split into compressible and solenoidal parts by a Helmholtz decomposition ($\mathbf{v} = \mathbf{v}_\perp + \mathbf{v}_{||}$) (see *e.g.* [22]). The compressible part $\mathbf{v}_{||}$ is longitudinal and curl-free ($\nabla \times \mathbf{v}_{||} = 0$) and the solenoidal part $\mathbf{v}_\perp$ is rotational and divergence-free ($\nabla \cdot \mathbf{v}_\perp = 0$). The two components are coupled and exchange energy. Compressible flows lead to an exchange between kinetic energy and density fluctuations, and kinetic energy is not conserved in compressible hydrodynamic turbulence.
Compressible velocity fluctuations exchange energy with sound waves. In supersonic flows, sound waves can steepen into shock waves. Shock waves are finite-amplitude fluctuations that steepen into a jump, forming a thin transition layer that is moving faster than the according linear group velocity of the underlying wave. This transition layer can be viewed as a local plane. Upstream and downstream of the shock plane, the flow quantities u are assumed to be homogeneous. The flow quantities can be regarded as stationary (thus $\frac{\partial u}{\partial t} = 0$) in the transition layer's system of reference. The relation of the downstream to upstream properties, called the jump conditions, can be derived by integrating the conservation laws (2.7)-(2.9) over a volume that extends both upstream and downstream. For an ideal gas, the jump conditions are called the Rankine-Hugoniot relations (see for example [67]). The relation of the upstream to downstream mass-density and velocity expressed by the upstream and downstream pressure is

$$\frac{\rho_\mathrm{down}}{\rho_\mathrm{up}} = \frac{1 + \frac{\kappa+1}{\kappa-1}\frac{p_\mathrm{down}}{p_\mathrm{up}}}{\frac{\kappa+1}{\kappa-1} + \frac{p_\mathrm{down}}{p_\mathrm{up}}} = \frac{v_\mathrm{up}}{v_\mathrm{down}}. \tag{2.58}$$

While the pressure ratio can reach infinite values, the compression ratio $\rho_\mathrm{down}/\rho_\mathrm{up}$ is limited by

$$\frac{\rho_\mathrm{down}}{\rho_\mathrm{up}} < \frac{\kappa+1}{\kappa-1}. \tag{2.59}$$

For an ideal gas with a ratio of specific heats of $\kappa = 5/3$, the compression ratio is thus limited to 4. The limitation of the density ratio downstream and upstream of the shock does not apply to shocks in an isothermal medium. Isothermality applies when the gas in the downstream region is cooled rapidly to the temperature in the upstream region, that means when the cooling happens on time scales much smaller than the fluid-dynamic time scales. When the temperature relation $T_\mathrm{down}/T_\mathrm{up} = 1$ is applied, the isothermal jump condition is

$$\frac{\rho_\mathrm{down}}{\rho_\mathrm{up}} = \left(\frac{v_\mathrm{up}}{c_\mathrm{s}}\right)^2. \tag{2.60}$$

Here, c_s is the constant isothermal sound speed. The relation (2.60) shows that the density ratio is determined by the square of the upstream sonic Mach number of the flow. The density contrast for an isothermal shock can reach arbitrarily high values, determined by the upstream sonic Mach number.
Magnetic fields lead to the more complex de-Hoffmann-Teller jump conditions, which additionally require that the normal component of the magnetic field with regard to the shock plane is conserved across the shock (see for example [5]). The according ratio of pressures in the case of an adiabatic equation of state is

$$\frac{p_\mathrm{down}}{p_\mathrm{up}} = \frac{\frac{\kappa+1}{\kappa-1}\frac{\rho_\mathrm{down}}{\rho_\mathrm{up}} - 1 + \frac{[B_\mathrm{t}]^2}{2p_\mathrm{up}}\left(\frac{\rho_\mathrm{down}}{\rho_\mathrm{up}-1}\right)}{\frac{\kappa+1}{\kappa-1} - \frac{\rho_\mathrm{down}}{\rho_\mathrm{up}}}. \tag{2.61}$$

Here, B_t denotes the tangential vector component of the magnetic field. The brackets $[B_\mathrm{t}]$ denote the difference of the quantity from its downstream value to its upstream value. The ratio of the tangential vector components of the magnetic field upstream and downstream to the shock are described by:

$$\frac{B_{t,\mathrm{down}}}{B_{t,\mathrm{up}}} = \frac{m\ v_{n,\mathrm{up}} - B_n^2}{m\ v_{n,\mathrm{down}} - B_n^2}. \tag{2.62}$$

Here, m is the momentum density, a constant across the shock, and B_n is the magnetic-field vector-component normal to the shock plane. This relation allows for two cases for the tangential vector component of the magnetic field. In the first case, the downstream value of the tangential-component of the magnetic-field is bigger than its upstream value. This causes the magnetic field in the downstream

region to be bent away from the normal vector to the plane. In the second case, the downstream value of B_t is smaller than its upstream value, and the magnetic field is bent towards the normal vector to the plane. These two cases correspond to the two compressive MHD modes, the fast magnetosonic wave and the slow magnetosonic wave, described in equations (2.20) and (2.21). The two cases are thus called fast shocks and slow shocks, respectively.
Shock phenomena are highly dissipative. By conserving momentum density m (upstream to downstream) and greatly increasing the mass density ρ_{down}, kinetic energy is clearly not conserved. Kinetic energy is efficiently turned into heat (in the adiabatic case) or lost through radiative dissipation (in the isothermal case). Shock fronts are two-dimensional structures. Their 2D, plane-like spatial extent covers all spatial length-scales in a compressible turbulent system. That means that shocks couple to velocity fluctuations on all spatial scales. This is the fundamental difference to incompressible fluid turbulence, where in the inertial range, dissipative effects do not play a considerable role. Thus there is *a priori* no reason to expect self-similar scaling in any range of the energy spectrum of compressible turbulence. The predictions of self-similar scaling in the incompressible case are based on global ideal energy conservation, which is destroyed by compressible effects.

2.5 Scaling laws for compressible turbulence

The simplest system of purely compressional turbulence is Burgers' turbulence for a one-dimensional system, governed by Burgers' equation

$$\frac{\partial v_x}{\partial t} + v_x \frac{\partial v_x}{\partial x} = \nu \frac{\partial^2 v_x}{\partial x^2}. \tag{2.63}$$

Here, v_x is the one-dimensional velocity, ν is the finite viscosity. In this system, fluid elements catch up with preceding ones, evolving into a saw-tooth-like spatial function of uncorrelated shocks. The finite viscosity leads to dissipation at the shock fronts. An analytical inertial-range spectral scaling-relation has been obtained for the Burgers' shock-turbulence by Kida [32]. The self-similar scaling exponent is -2 for this system. The three-dimensional Burgers' equations are often regarded as a high sonic Mach number limit for compressible hydrodynamic turbulence, even though shocks in hydrodynamic turbulence are expected to be correlated (see *e.g.* Elmegreen and Scalo [22]). Following this argument, in the high Mach number limit of compressible hydrodynamic turbulence, the power spectrum of velocity fluctuation is predicted to be

$$E(k) \sim k^{-2}. \tag{2.64}$$

This scaling prediction only accounts for shocks, not for eddies. It provides little insight into regimes where both rotational and compressional structures are important. In transonic and mildly-supersonic hydrodynamic turbulence, with sonic Mach numbers ranging from 1 to 20, both rotational and compressional flows contribute to turbulence. Additionally, in Burgers' turbulence, density fluctuations are passively advected, while in hydrodynamic turbulence they are genuinely coupled to velocity modes.

2.5.1 The Fleck model

To incorporate density fluctuations into predictions for self-similar correlated power spectra, Fleck proposed a model for compressible hydrodynamic turbulence [25] in 1996. The phenomenological model is based on two arguments, proposed much earlier by von Weizsäcker in 1951 [74] and Lighthill in 1955 [44]. Von Weizsäcker describes the observed density fluctuations in neutral interstellar clouds as a hierarchy of consecutive cloud sizes and cloud densities, analogous to a hierarchy of turbulent eddies in incompressible fluid turbulence. He assumes that every large cloud consists of a certain number of smaller clouds. The smaller clouds themselves consist of even smaller clouds until the smallest clouds with velocities smaller than the sound speed are reached. The according hierarchy of clouds have densities ρ_ν and average gas velocities v_ν. Here, ν is an index that takes integral values and increases with cloud size l_ν. Von Weizsäcker connects the density of a cloud of size l to the size of this cloud by equation

$$\frac{\rho_\nu}{\rho_{\nu+1}} = \left(\frac{l_\nu}{l_{\nu+1}}\right)^{-3\alpha_\nu} = f^{-1}. \tag{2.65}$$

Here, the parameter α_ν describes the degree of compression at the step ν. f is the associated volume filling factor. Assuming self-similarity, the parameter α_ν is independent of the scale step ν and equation (2.65) describes a scaling-law for the density fluctuations of compressible neutral gas turbulence. In the case of perfect isotropic compression in three dimensions, α takes the value 1, in perfect one-dimensional compression $\alpha = 1/3$, and α is zero in the incompressible limit.
The second argument of the Fleck model is based on the assumption of Lighthill that the total viscous rate of dissipation of energy in a compressible fluid is $\rho v^3/l$. This is also the energy transfer rate per unit volume and is assumed to be constant. Combining the two arguments, Fleck proposes the following set of scaling relations:

$$\rho \sim l^{-3\alpha}, \tag{2.66}$$

$$N \sim l^{1-3\alpha}, \tag{2.67}$$

$$M \sim l^{3-3\alpha}, \tag{2.68}$$

$$v \sim l^{1/3+\alpha}, \tag{2.69}$$

$$E(k) \sim k^{-5/3-2\alpha}. \tag{2.70}$$

N is the column density, M the mass and $E(k)$ is the power spectrum of the velocity fluctuations. In the incompressible limit $\alpha = 0$, the scaling relation for the power spectrum of the velocity fluctuations reveals a Kolmogorov-like scaling with a scaling exponent of $-5/3$. With growing compression, *i.e.* with growing average sonic Mach numbers ($\alpha := \alpha(\mathcal{M}_\mathrm{s})$), the Fleck model predicts a steepening of the velocity power-spectrum. In the limit of an infinitely compressed density, α takes the value of 1 and the scaling-exponent of the velocity power-spectrum is $-11/3$.
On the basis of the Fleck model and the argument of a constant energy-transfer rate per unit volume, Kritsuk *et al.* [36] propose a universal scaling of the density-weighted velocity $\rho^{1/3}v$. The power spectrum of the density-weighted velocity is predicted to scale with a Kolmogorov power-law slope of $-5/3$, independent of the degree of compression and thus independent of the average sonic Mach number of the flow. In addition to the agreement of the spectral scaling of the density-weighted velocity, a Kolmogorov scaling of the second order structure function was restored for this quantity. Combining the Fleck-model predictions with an assumed universal scaling of the density-weighted velocity, the following scaling predictions result:

$$\rho \sim l^{-3\alpha}, \tag{2.71}$$

$$\frac{1}{2}\left\langle v^2 \right\rangle \sim k^{-5/3-2\alpha}, \tag{2.72}$$

$$\frac{1}{2}\left\langle \rho^{2/3} v^2 \right\rangle \sim k^{-5/3}, \tag{2.73}$$

$$\frac{1}{2}\left\langle \rho v^2 \right\rangle \sim k^{-5/3+\alpha}. \tag{2.74}$$

Equations (2.72)-(2.74) are scaling relations for the velocity power-spectrum, the power spectrum of the density-weighted velocity, and the kinetic-energy spectrum. With an increase of degree of compression, the difference in the scaling exponents of the three quantities should increase. The ratio of the according spectral exponents is thus predicted to increase by 2α in the case of velocity power-spectrum *vs.* density-weighted velocity, and by α in the case of the ratio of the scaling exponent of the density-weighed velocity *vs.* the kinetic-energy scaling-exponent. The difference between the scaling exponent of the velocity power-spectrum and the one of the kinetic-energy spectrum is predicted to increase by 3α.
A larger degree of compression reflects a broadening of the mass-density probability density function (PDF). In isothermal hydrodynamics, the density PDF is predicted to follow a lognormal distribution (see *e.g.* [72]),

$$P\left(\ln\frac{\rho}{\rho_0}\right) = \frac{1}{\sigma\sqrt{2\pi}} \exp\left[-\frac{1}{2}\left(\frac{\ln\frac{\rho}{\rho_0}}{\sigma}\right)^2\right] \tag{2.75}$$

P is the probability for the logarithmic mass-density $\ln(\rho/\rho_0)$ to occur. Padoan proposes [55] that the width of the probability distribution of the logarithmic density $\sigma_{\ln\rho}$ reflects the degree of compression and can be expressed as a function of the sonic Mach number

$$\sigma^2_{\ln\rho} = \ln(1 + b^2\mathcal{M}_\mathrm{s}^2). \tag{2.76}$$

Here, b is a parameter, modeling a first-order linear relation between the width of the density PDF of the linear mass-density ρ and the sonic Mach number in the form $\sigma = b\mathcal{M}_\mathrm{s}$. A fit to experimental data from the interstellar medium yields $b \approx 0.5$ [55]. At higher average sonic Mach numbers, broader density PDFs are predicted. The broader density PDFs should, following the Fleck model, also be reflected in the difference of the scaling exponents of the velocity power-spectra and the kinetic-energy spectra.

2.5.2 Scaling-law predictions based on the ratio of specific heats

An alternative approach to account for compressibility in hydrodynamic turbulence was suggested by Shivamoggi [65] in 1992. He parametrizes the rescaling of the isentropic equations governing the motions of a compressible fluid:

$$\mathbf{x} = \mathbf{x}'/\lambda, \qquad t = t'\lambda^{\alpha/3-1}, \qquad \mathbf{v} = \mathbf{v}'/\lambda^{\alpha/3}. \tag{2.77}$$

Here, $\mathbf{x}$, $\mathbf{v}$, and t are the position vector, velocity vector, and scalar time in the base equations. The scale index is λ, and α is a free parameter. The set of governing equations are formally invariant under rescaling (2.77), by the choice of:

$$\rho = \rho'/\lambda^{2\alpha/3(\kappa-1)}, \qquad p = p'/\lambda^{2\alpha\kappa/3(\kappa-1)}, \qquad \nu = \nu'/\lambda^{[2\alpha+(\kappa-1)(\alpha+3)]/3(\kappa-1)}. \tag{2.78}$$

Here, κ denotes the ratio of specific heats, ν is the kinematic viscosity.
Shivamoggi's prediction for the scaling of the kinetic energy spectrum is based on the invariance of the total rate of dissipation ϵ under scale transformations. The main assumption is that the total rate of dissipation is invariant under scaling transformation (2.77). Using the scale transformation (2.77), the total rate of dissipation ϵ changes according to:

$$\epsilon = \epsilon'\lambda^{1-\alpha-2\alpha/3(\kappa-1)}. \tag{2.79}$$

The total rate of dissipation is invariant under rescaling (2.79) by the choice:

$$\alpha = \frac{3(\kappa-1)}{3\kappa-1}. \tag{2.80}$$

The scaling relations for the velocity and density increments can be rewritten in the form

$$v(l) \sim l^{\frac{(\kappa-1)}{3\kappa-1}}, \tag{2.81}$$

$$\rho(l) \sim l^{\frac{2(\kappa-1)^2}{3\kappa-1}}. \tag{2.82}$$

The ratio of specific heats κ of the fluid can be replaced phenomenologically by $1/\mathcal{M}_\mathrm{s}^2$. Combining the two scaling relations and assuming a constant kinetic-energy transfer per unit volume, Shivamoggi predicts self-similar scaling of the kinetic-energy spectrum as a function of the ratio of specific heats

$$\frac{1}{2}\left\langle \rho v^2 \right\rangle \sim \rho_0^{\frac{\kappa-1}{3\kappa-1}} c_\mathrm{s}^{-\frac{2}{3\kappa-1}} \epsilon^{\frac{2\kappa}{3\kappa-1}} k^{-\frac{5\kappa-1}{3\kappa-1}}. \tag{2.83}$$

Here, c_s is the sound speed. In the isothermal limit $\kappa \to 1$, this scaling relation reduces to

$$\frac{1}{2}\left\langle \rho v^2 \right\rangle \sim c_\mathrm{s}^{-1}\epsilon k^{-2} \tag{2.84}$$

Shivamoggi's scaling relation for the kinetic energy is steeper than the Kolmogorov scaling and contradicts with the Fleck prediction, where the kinetic-energy scaling is predicted to be flatter than the Kolmogorov scaling. The steepening of the spectrum is physically explained by the shocks acting as a sink for turbulent energy, as they turn energy into heat or efficiently radiate it away in the isothermal case.

2.5.3 Scaling-laws for compressible MHD

The influence of the magnetic field in compressible turbulence and the according changes in self-similar scaling of power spectra is not well understood. In addition to the sonic Mach number $\mathcal{M}_\mathrm{s}$, the Alfvén Mach number $\mathcal{M}_\mathrm{A}$ is a parameter that determines the properties of scaling. An attempt to predict

compressible MHD self-similar scaling was brought forward by Shivamoggi in 2008 [66]. His arguments are based on the Iroshnikov-Kraichnan and Goldreich-Sridhar models for incompressible MHD. In the MHD case, the compressibility is parameterized by the ratio of specific heats κ. The argument follows that for compressible hydrodynamic turbulence spectra in Chapter 2.5.2. The main assumption is, as in the hydrodynamic case, the invariance of the total rate of dissipation under scale transformations (2.77). The prediction for the total energy spectrum, based on the IK spectrum, is given by

$$E(k_\perp) \sim \rho_0^{\frac{\kappa-1}{2\kappa-1}} c_\mathrm{s}^{-\frac{2}{2\kappa-1}} \epsilon^{\frac{\kappa}{2\kappa-1}} k_\perp^{-\frac{3\kappa-1}{2\kappa-1}}. \tag{2.85}$$

Here, c_s is the sound speed, and κ is the ratio of specific heats. The compressible extension of the Goldreich-Sridhar energy spectrum is given by

$$E(k_\perp) \sim \rho_0^{\frac{\kappa-1}{3\kappa-1}} c_\mathrm{s}^{-\frac{2}{3\kappa-1}} \epsilon^{\frac{2\kappa}{3\kappa-1}} k_\perp^{-\frac{5\kappa-1}{3\kappa-1}}. \tag{2.86}$$

In the infinite-compressibility limit ($\kappa \to 1$), the compressible extensions of the IK and GS spectra take the form

$$E(k_\perp)_\mathrm{IK} \sim c_\mathrm{s}^{-2} \epsilon k_\perp^{-2}, \tag{2.87}$$

$$E(k_\perp)_\mathrm{GS} \sim c_\mathrm{s}^{-1} \epsilon k_\perp^{-2}. \tag{2.88}$$

The spectral scaling in compressible MHD is predicted to be steeper than in the incompressible limit, with a spectral scaling exponent of -2 in the infinite-compressibility limit.

2.6 Momentum density, a candidate for self-similar scaling in compressible turbulence

We propose an alternative way of predicting self-similar scaling of power spectra in compressible hydrodynamic and MHD turbulence, based on the momentum density $\rho\mathbf{v}$. Momentum is an inviscid quadratic invariant of the compressible hydrodynamic equations. In addition, momentum conservation governs the upstream and downstream properties of hydrodynamic and magnetohydrodynamic shock waves. In this section we show that the evolution equation of the Fourier components of the momentum density provides a reasonable argument for self-similar scaling of the momentum power-spectrum.
The ideal isothermal hydrodynamic equations in component form are given by

$$\frac{\partial \rho}{\partial t} + \frac{\partial (\rho v_i)}{\partial x_i} = 0, \tag{2.89}$$

$$\frac{\partial (\rho v_i)}{\partial t} + \frac{\partial (\rho v_i v_m)}{\partial x_m} + \frac{\partial p}{\partial x_i} = 0. \tag{2.90}$$

Here, v_i is the i-th component of the velocity vector in real space, ρ is the mass density, and p is the scalar thermal pressure. The pressure is connected to the mass density by the isothermal equation of state, so that

$$p = c_\mathrm{s}^2 \cdot \rho. \tag{2.91}$$

Applying the divergence operator $\nabla\cdot$ to equation (2.90), one obtains:

$$\frac{\partial}{\partial x_i}\left(\frac{\partial (\rho v_i)}{\partial t}\right) + \frac{\partial^2 (\rho v_i v_m)}{\partial x_i \partial x_m} + \Delta p = 0. \tag{2.92}$$

The partial time and space derivative can be interchanged, the spatial derivative of the momentum density is inserted from equation (2.89). This yields

$$-\frac{\partial^2 \rho}{\partial t^2} + \frac{\partial^2 (\rho v_i v_m)}{\partial x_i \partial x_m} + \Delta p = 0. \tag{2.93}$$

The Fourier transform of equation (2.93) is

$$-\frac{\partial^2}{\partial t^2}\mathcal{F}(\rho) - k_i k_m \mathcal{F}(\rho v_i v_m) - k^2 \mathcal{F}(p) = 0, \tag{2.94}$$

or

$$\mathcal{F}(p) = -\frac{1}{k^2}\frac{\partial^2}{\partial t^2}\mathcal{F}(\rho) - \frac{k_i k_m}{k^2}\mathcal{F}(\rho v_i v_m). \tag{2.95}$$

In equation (2.95) the Fourier transform of the thermal pressure is expressed in terms of the Fourier transforms of the non-linear term and the mass-density term.
A direct Fourier transformation of the momentum continuity equation (2.90) leads to

$$\frac{\partial}{\partial t}\mathcal{F}(\rho v_i) + ik_m\mathcal{F}(\rho v_i v_m) + ik_i\mathcal{F}(p) = 0. \tag{2.96}$$

Combining equation (2.95) and equation (2.96) to eliminate the pressure term yields:

$$\frac{\partial}{\partial t}\mathcal{F}(\rho v_i) = -ik_m\mathcal{F}(\rho v_i v_m) - ik_i\left(-\frac{k_j k_m}{k^2}\mathcal{F}(\rho v_j v_m) - \frac{1}{k^2}\frac{\partial^2}{\partial t^2}\mathcal{F}(\rho)\right). \tag{2.97}$$

Combining the non-linear terms in equation (2.97) leads to

$$\frac{\partial}{\partial t}\mathcal{F}(\rho v_i) = -i\left[k_m\delta_{ij} - k_i\frac{k_j k_m}{k^2}\right]\mathcal{F}(\rho v_j v_m) + i\frac{k_i}{k^2}\frac{\partial^2}{\partial t^2}\mathcal{F}(\rho). \tag{2.98}$$

The projection operator of the non-linear term in equation (2.98) can be replaced by the projection operator P_{ijm} that was defined for the incompressible case in equation (2.34). Additionally, the momentum terms ρv_i are replaced by m_i, denoting the i-th component of the momentum vector. We obtain

$$\frac{\partial}{\partial t}\mathcal{F}(m_i) = -\frac{i}{2}P_{ijm}\mathcal{F}(m_j v_m) + i\frac{k_i}{k^2}\frac{\partial^2}{\partial t^2}\mathcal{F}(\rho). \tag{2.99}$$

Now, the Fourier transform of the non-linear term is evaluated. Let L be the length of one side of a periodic box with a volume $V = L^3$. The Fourier series expansion of the individual terms m_i and v_i yield [40]

$$m_i(\mathbf{x}) = \frac{(2\pi)^3}{L^3}\sum_{\mathbf{k}}\hat{m}_i(\mathbf{k})e^{i\mathbf{k}\cdot\mathbf{x}}, \tag{2.100}$$

and

$$v_i(\mathbf{x}) = \frac{(2\pi)^3}{L^3}\sum_{\mathbf{k}}\hat{v}_i(\mathbf{k})e^{i\mathbf{k}\cdot\mathbf{x}}. \tag{2.101}$$

The hat denotes the Fourier components of the according quantity. The Fourier transform $\mathcal{F}(m_j u_m)$ can be expressed by

$$\begin{aligned}
\mathcal{F}(m_j v_m) &= \frac{1}{2\pi}\int_V m_j(\mathbf{x})v_m(\mathbf{x})e^{-i\mathbf{k}\cdot\mathbf{x}}d^3x && (2.102)\\
&= \frac{(2\pi)^3}{L^6}\int_V\sum_{\mathbf{p}}\sum_{\mathbf{q}}\hat{m}_j(\mathbf{p})e^{i\mathbf{p}\cdot\mathbf{x}}\hat{v}_m(\mathbf{q})e^{i\mathbf{q}\cdot\mathbf{x}}e^{-i\mathbf{k}\cdot\mathbf{x}}d^3x && (2.103)\\
&= \frac{(2\pi)^3}{L^6}\sum_{\mathbf{p}}\sum_{\mathbf{q}}\hat{m}_j(\mathbf{p})\hat{v}_m(\mathbf{q})\int_V e^{i\mathbf{p}\cdot\mathbf{x}}e^{i\mathbf{q}\cdot\mathbf{x}}e^{-i\mathbf{k}\cdot\mathbf{x}}d^3x && (2.104)\\
&= \frac{(2\pi)^3}{L^6}\sum_{\mathbf{p}}\sum_{\mathbf{q}}\hat{m}_j(\mathbf{p})\hat{v}_m(\mathbf{q})\int_V e^{-i(\mathbf{k}-\mathbf{p}-\mathbf{q})\cdot\mathbf{x}}d^3x && (2.105)\\
&= \frac{(2\pi)^3}{L^3}\sum_{\mathbf{p}}\sum_{\mathbf{q}}\hat{m}_j(\mathbf{p})\hat{v}_m(\mathbf{q})\delta(\mathbf{k}-\mathbf{p}-\mathbf{q}) && (2.106)
\end{aligned}$$

In the limit of an infinitely extended box with $V \to \infty$, the Fourier transform of the non-linear term can be rewritten in the form [40]

$$\mathcal{F}(m_j v_m) = \int_{\mathbb{R}^3}\int_{\mathbb{R}^3}\hat{m}_j(\mathbf{p})\hat{v}_m(\mathbf{q})\delta(\mathbf{k}-\mathbf{p}-\mathbf{q})d^3p\ d^3q. \tag{2.107}$$

Inserting this formulation of the Fourier transform of the non-linear term into the evolution equation of the Fourier components of the momentum density (2.99) leads to

$$\boxed{\frac{\partial}{\partial t}(\hat{m}_i)(\mathbf{k}) = -\frac{i}{2}P_{ijm}\int_{\mathbb{R}^3}\int_{\mathbb{R}^3}\hat{m}_j(\mathbf{p})\hat{v}_m(\mathbf{q})\delta(\mathbf{k}-\mathbf{p}-\mathbf{q})d^3p\ d^3q + i\frac{k_i}{k^2}\frac{\partial^2}{\partial t^2}(\hat{\rho}(\mathbf{k})).} \tag{2.108}$$

In equation (2.108), only two terms contribute to time changes of the Fourier components of momentum density. One contribution comes from the nonlinear term, where only triads in Fourier space can add to the integral and thus to the time change of the momentum density. The second contribution comes from the mass density. The triad interactions of momentum and velocity belonging to wave vectors $\mathbf{p}$ and $\mathbf{q}$ can interact and exchange with the momentum belonging to wave vector $\mathbf{k}$. The second partial-time derivative of the mass-density structure belonging to wave vector $\mathbf{k}$ serves as a sink or source for changes to the momentum density. The spectral distribution of momentum among scales is thus determined by a triad interaction part, and a wave-vector $\mathbf{k}$-dependent mass-density part. The former influence indicates self-similarity, while the spectral scaling properties of the latter term must be determined by numerical experiments. The density contribution to the momentum change is furthermore expected to depend on the realization of the flow, that means on the RMS Mach number of the turbulence.
The momentum equation in Fourier space for the ideal isothermal MHD equations can be derived by repeating the above formalism based on the equations

$$\frac{\partial\rho}{\partial t} + \frac{\partial(\rho v_i)}{\partial x_i} = 0, \tag{2.109}$$

$$\frac{\partial(\rho v_i)}{\partial t} + \frac{\partial(\rho v_i v_m)}{\partial x_m} + \frac{\partial(p+\frac{1}{2}b^2)}{\partial x_i} - \frac{\partial(b_i b_m)}{\partial x_m} = 0, \tag{2.110}$$

$$\frac{\partial(b_i)}{\partial t} + \frac{\partial(v_i b_m)}{\partial x_m} - \frac{\partial(b_i v_m)}{\partial x_m} = 0. \tag{2.111}$$

The Fourier transform of the total pressure $p+1/2b^2$ is obtained by applying the divergence operator $\nabla\cdot$ to the real space momentum equation (2.110):

$$\frac{\partial}{\partial x_i}\left(\frac{\partial(\rho v_i)}{\partial t}\right) + \frac{\partial^2(\rho v_i v_m)}{\partial x_i \partial x_m} + \Delta(p+\frac{1}{2}b^2) - \frac{\partial^2(b_i b_m)}{\partial x_i \partial x_m} = 0. \tag{2.112}$$

Exchanging the time and spatial derivative in the first term, inserting the definition of the mass conservation (2.109), and applying the Fourier transform $\mathcal{F}$ leads to

$$-\frac{\partial^2}{\partial t^2}\mathcal{F}(\rho) - k_i k_m \mathcal{F}(\rho v_i v_m) - k^2\mathcal{F}(p+\frac{1}{2}b^2) + k_i k_m \mathcal{F}(b_i b_m) = 0, \tag{2.113}$$

or

$$\mathcal{F}(p+\frac{1}{2}b^2) = -\frac{1}{k^2}\frac{\partial^2}{\partial t^2}\mathcal{F}(\rho) - \frac{k_i k_m}{k^2}\mathcal{F}(\rho v_i v_m) + \frac{k_i k_m}{k^2}\mathcal{F}(b_i b_m). \tag{2.114}$$

The Fourier transformed MHD momentum equation (2.110) is

$$\frac{\partial}{\partial t}\mathcal{F}(\rho v_i) = -ik_m\mathcal{F}(\rho v_i v_m) - ik_i\mathcal{F}(p+\frac{1}{2}b^2) + ik_m\mathcal{F}(b_i b_m). \tag{2.115}$$

The pressure term in equation (2.115) is replaced by the definition of the Fourier transform of the total pressure (2.114)

$$\frac{\partial}{\partial t}\mathcal{F}(\rho v_i) = -ik_m\mathcal{F}(\rho v_i v_m) - ik_i\left(-\frac{k_j k_m}{k^2}\mathcal{F}(\rho v_j v_m) + \frac{k_j k_m}{k^2}\mathcal{F}(b_j b_m) - \frac{1}{k^2}\frac{\partial^2}{\partial t^2}\mathcal{F}(\rho)\right) + ik_m\mathcal{F}(b_i b_m). \tag{2.116}$$

Sorting terms into nonlinear momentum terms and magnetic terms leads to

$$\frac{\partial}{\partial t}\mathcal{F}(m_i) = -\frac{i}{2}P_{ijm}\mathcal{F}(m_j v_m) + \frac{i}{2}P_{ijm}\mathcal{F}(b_j b_m) + i\frac{k_i}{k^2}\frac{\partial^2}{\partial t^2}\mathcal{F}(\rho). \tag{2.117}$$

The Fourier transform of the non-linear terms is carried out according to the non-magnetic case. The resulting inviscid momentum equation in Fourier space is

$$\boxed{\frac{\partial}{\partial t}(\hat{m}_i)(\mathbf{k}) = -\frac{i}{2}P_{ijm}\int_{\mathbb{R}^3}\int_{\mathbb{R}^3}\left[\hat{m}_j(\mathbf{p})\hat{v}_m(\mathbf{q}) - \hat{b}_j(\mathbf{p})\hat{b}_m(\mathbf{q})\right]\delta(\mathbf{k}-\mathbf{p}-\mathbf{q})d^3p\ d^3q + i\frac{k_i}{k^2}\frac{\partial^2}{\partial t^2}(\hat{\rho}(\mathbf{k})).} \tag{2.118}$$

The RHS integral in equation (2.118) provides contributions to momentum changes if the wave vectors $\mathbf{k}$, $\mathbf{p}$, and $\mathbf{q}$ form a triangle. In addition to the contributions obtained in the non-magnetic case of equation (2.108), magnetic-field modes can lead to a change in the momentum field. Again, the second time-derivative of the mass-density structures that belong to a wave vector $\mathbf{k}$ acts as a sink or source for momentum change. As in the non-magnetic case, the non-linear triads indicate self-similar transport of momentum, while the k-dependent density-contribution has to be determined numerically.

3. NUMERICAL SCHEME

In the course of this work a simulation code has been developed to solve the equations of compressible hydrodynamics and compressible MHD. The numerical methods that the code employs are described in this Chapter. The numerical work performed in this context was to extend a 2D formulation of a semidiscrete central-difference scheme to three spatial dimensions. In addition, a constrained transport scheme for the divergence-free update of the magnetic field was incorporated into the base scheme. The resulting numerical scheme is a forward-in-time central-in-space hybrid scheme. A similar approach was taken by Grauer *et al.* and is used in the *RACOON* code [18].

3.1 Kurganov-Tadmor in three space dimensions

The numerical scheme is based on a one-dimensional semidiscrete formulation of a central-difference scheme developed by Kurganov and Tadmor [39]. The scheme can be viewed as a higher-order extension to the Lax-Friedrich method of solving hyperbolic partial differential equations. A two-dimensional extension of the Kurganov-Tadmor scheme was developed by Balbas and Tadmor [2] and used to solve the compressible 2D-MHD equations. A simple dimension-by-dimension approach allowed for a straightforward extension to three spatial dimensions.
The scheme consists of three steps: (1) spatial reconstruction of point values of the conserved quantities at the centers of the cell surfaces, (2) computation of fluxes at the cell interfaces, and (3) time integration of the resulting set of ordinary differential equations. First, the Kurganov-Tadmor (KT) flux definition is introduced.
The total time derivative of the cell averages of the hydrodynamic quantities $\bar{\mathbf{u}}$ in three space dimensions is computed *via* the Kurganov-Tadmor flux definition,

$$\frac{\mathrm{d}\bar{\mathbf{u}}_{i,j,k}}{\mathrm{d}t} = -\frac{\mathbf{H}^x_{i+\frac{1}{2},j,k}(t) - \mathbf{H}^x_{i-\frac{1}{2},j,k}(t)}{\Delta x} - \frac{\mathbf{H}^y_{i,j+\frac{1}{2},k}(t) - \mathbf{H}^y_{i,j-\frac{1}{2},k}(t)}{\Delta y} - \frac{\mathbf{H}^z_{i,j,k+\frac{1}{2}}(t) - \mathbf{H}^z_{i,j,k-\frac{1}{2}}(t)}{\Delta z}. \quad (3.1)$$

The numerical flux vectors $\mathbf{H}$ in the x-, y-, and z-directions are defined as

$$\mathbf{H}^x_{i+\frac{1}{2},j,k}(t) = \frac{\mathbf{f}^x(\mathbf{u}^{\mathrm{West}}_{i+1,j,k}(t)) + \mathbf{f}^x(\mathbf{u}^{\mathrm{East}}_{i,j,k}(t))}{2} - \frac{a^x_{i+\frac{1}{2},j,k}}{2}\left[\mathbf{u}^{\mathrm{West}}_{i+1,j,k} - \mathbf{u}^{\mathrm{East}}_{i,j,k}\right], \quad (3.2)$$

$$\mathbf{H}^y_{i,j+\frac{1}{2},k}(t) = \frac{\mathbf{f}^y(\mathbf{u}^{\mathrm{South}}_{i,j+1,k}(t)) + \mathbf{f}^y(\mathbf{u}^{\mathrm{North}}_{i,j,k}(t))}{2} - \frac{a^y_{i,j+\frac{1}{2},k}}{2}\left[\mathbf{u}^{\mathrm{South}}_{i,j+1,k} - \mathbf{u}^{\mathrm{North}}_{i,j,k}\right], \quad (3.3)$$

$$\mathbf{H}^z_{i,j,k+\frac{1}{2}}(t) = \frac{\mathbf{f}^z(\mathbf{u}^{\mathrm{Bottom}}_{i,j,k+1}(t)) + \mathbf{f}^z(\mathbf{u}^{\mathrm{Top}}_{i,j,k}(t))}{2} - \frac{a^z_{i,j,k+\frac{1}{2}}}{2}\left[\mathbf{u}^{\mathrm{Bottom}}_{i,j,k+1} - \mathbf{u}^{\mathrm{Top}}_{i,j,k}\right]. \quad (3.4)$$

where vectors $\mathbf{f}$ denote the flux-function vector of the hydrodynamic part of the base equations (2.12)-(2.14). The flux-function vector in x-direction for the isothermal MHD equations is for example given by

$$\mathbf{f}^x = \begin{pmatrix} \rho v_x \\ \rho v_x^2 + p + 1/2(-b_x^2 + b_y^2 + v_z^2) \\ \rho v_x v_y - b_x b_y \\ \rho v_x v_z - b_x b_z \end{pmatrix}. \quad (3.5)$$

The quantities $\mathbf{u}^{\mathrm{East}}$, $\mathbf{u}^{\mathrm{West}}$ *etc.* denote the vector of the reconstructed point values of the conserved quantities at the cell interfaces. The local maximum speeds of propagation a^x, a^y, and a^z at the cell

interfaces are estimated by

$$a^x_{i+\frac{1}{2},j,k} = \max\left\{\rho\left(\frac{\partial \mathbf{f}}{\partial \mathbf{u}}(\mathbf{u}^{\text{West}}_{i+1,j,k})\right), \rho\left(\frac{\partial \mathbf{f}}{\partial \mathbf{u}}(\mathbf{u}^{\text{East}}_{i,j,k})\right)\right\} \tag{3.6}$$

where $\rho(A)$ is the maximum of the magnitude of the eigenvalues of the Jacobian matrix A. This semidiscrete formulation of total time derivatives of the conserved quantities is independent of the choice of the specific reconstruction method used to obtain point values u at the cell interfaces. The particular choice of the reconstruction method used in the KT code is described in detail below.

3.1.1 Spatial point value reconstruction

Point values of the conserved quantities are interpolated to the cell interfaces *via* a 3rd order central weighted essentially non-oscillatory (CWENO) scheme of Levy *et al.* [41], extending the 2D formulation of Balbas [2] to three spatial dimensions. The cell averages of the hydrodynamic quantities of each cell reside in the cell center. The cell averages are the basis for the point value reconstruction at the surrounding interfaces in the East, West, North, South, Top, and Bottom directions.
In CWENO, the point value of one conserved quantity u at a position inside the spatial cell interval

$$I_{i,j,k} = \left[x_{i-\frac{1}{2},j,k}, x_{i+\frac{1}{2},j,k}\right], \left[y_{i,j-\frac{1}{2},k}, y_{i,j+\frac{1}{2},k}\right], \left[z_{i,j,k-\frac{1}{2}}, z_{i,j,k+\frac{1}{2}}\right],$$

is computed from cell averages using piecewise quadratic polynomials $p(x_i, y_j, z_k)$. The polynomials are convex combinations of the two linear polynomials $P_{\text{L}}(x, y, z)$ and $P_{\text{R}}(x, y, z)$, and the quadratic central polynomial $P_{\text{C}}(x, y, z)$. In the x-direction, holding y and z fixed, the polynomial is given by

$$p_i(x, y_j, z_k) := w_{\text{L}} \cdot P_{\text{L}}(x, y_i, z_k) + w_{\text{C}} \cdot P_{\text{C}}(x, y_i, z_k) + w_{\text{R}} \cdot P_{\text{R}}(x, y_i, z_k), \qquad \sum_{i\in\{\text{L,C,R}\}} w_i = 1, \tag{3.7}$$

The linear polynomials conserve the cell averages $\bar{u}_{i-1,j,k}$, $\bar{u}_{i,j,k}$ and $\bar{u}_{i,j,k}$, $\bar{u}_{i+1,j,k}$. They are defined by:

$$P_L(x, y_i, z_k) = \overline{u}_{i,j,k} + \frac{\overline{u}_{i,j,k} - \overline{u}_{i-1,j,k}}{\Delta x} \cdot (x - x_i), \tag{3.8}$$

$$P_R(x, y_i, z_k) = \overline{u}_{i,j,k} + \frac{\overline{u}_{i+1,j,k} - \overline{u}_{i,j,k}}{\Delta x} \cdot (x - x_i). \tag{3.9}$$

The central quadratic parabola, holding y and z fixed is:

$$\begin{aligned} P_C(x, y_i, z_k) \quad = \quad & \overline{u}_{i,j,k} - \frac{1}{12}(\overline{u}_{i-1,j,k} - 2\overline{u}_{i,j,k} + \overline{u}_{i+1,j,k}) - \frac{1}{12}(\overline{u}_{i,j-1,k} - 2\overline{u}_{i,j,k} + \overline{u}_{i,j+1,k}) \\ & - \frac{1}{12}(\overline{u}_{i,j,k-1} - 2\overline{u}_{i,j,k} + \overline{u}_{i,j,k+1}) + \frac{\overline{u}_{i+1,j,k} - \overline{u}_{i-1,j,k}}{2\Delta x} \cdot (x - x_i) \\ & + \frac{\overline{u}_{i-1,j,k} - 2\overline{u}_{i,j,k} + 2\overline{u}_{i+1,j,k}}{\Delta x}^2 \cdot (x - x_i)^2 \end{aligned} \tag{3.10}$$

The central parabola is determined so as to satisfy the conservation of the cell averages $\bar{u}_{i-1,j,k}$, $\bar{u}_{i,j,k}$ and $\bar{u}_{i+1,j,k}$. The two additional correction terms in equation (3.10) in the directions transverse to the reconstruction guarantee third order accuracy when the point value u is computed from the surrounding cell averages. The non-linear weights w_i in equation (3.7) are chosen such as to provide for non-oscillatory behavior of the reconstruction in the vicinity of steep gradients. They are:

$$w_i = \frac{\alpha_i}{\sum_m \alpha_m}, \quad \text{with} \quad \alpha_i = \frac{c_i}{(\epsilon + IS_i)^2}, \tag{3.11}$$

where c_i is any symmetric choice of linear weights (*e.g.* $c_{\text{L}} = c_{\text{R}} = 1/4$, and $c_{\text{C}} = 1/2$). ϵ is a small parameter (*e.g.* 10^{-6}) that prevents the denominator from vanishing. The non-linear smoothness indicators IS_i provide a local measure of the steepness of the polynomial and are given by

$$IS_{\text{L}} = (\bar{u}_{i,j,k} - \bar{u}_{i-1,j,k})^2, \qquad IS_{\text{R}} = (\bar{u}_{i+1,j,k} - \bar{u}_{i,j,k})^2 \tag{3.12}$$

$$IS_{\text{C}} = \frac{13}{3}(\bar{u}_{i+1,j,k} - 2\bar{u}_{i,j,k} + \bar{u}_{i-1,j,k})^2 + \frac{1}{4}(\bar{u}_{i+1,j,k} - \bar{u}_{i-1,j,k})^2. \tag{3.13}$$

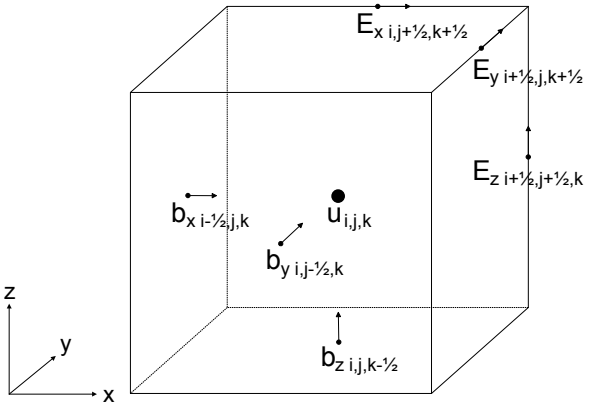

Fig. 3.1: The location of cell averages in a grid cell. The hydrodynamic quantities $\mathbf{u}_{i,j,k}$ are located at the center of the cell. The cell averages of the magnetic-field components are located at staggered positions $-\frac{1}{2}$. The line averages of the components of the electric-field flux vector are located at the cell edges.

In the vicinity of strong gradients, the central smoothness indicator and the smoothness indicator in the direction of the discontinuity become very large. The corresponding non-linear weights become very small and the reconstruction switches to second-order.
In a system of equations, the choice of the smoothness indicators influences the grid viscosity of the system. The various conserved quantities can develop steep gradients and discontinuities at different grid points. Computing the smoothness indicators for each quantity individually forces the scheme to use different stencils at the same grid points for the conserved quantities. This leads to both an increase in grid viscosity and to the onset of spurious oscillations. Choosing a single quantity for all the conserved quantities showed to result in a smaller grid viscosity. In the KT code, the density is chosen as the leading quantity for the computation of the smoothness indicators because the density field develops the most pronounced gradients. A detailed discussion of the usage of smoothness indicators in systems of equations is described by Levy *et al.* [41].
The point values $u^{\mathrm{East}}_{i,j,k}$, $u^{\mathrm{West}}_{i,j,k}$ at the cell interfaces, required by the Kurganov-Tadmor flux formulation (3.2) take the explicit form:

$$\begin{aligned} u^{\mathrm{East}}_{i,j,k}(t^n) :=& p^n_i(x_{i+\frac{1}{2}}, y_j, z_k) = \frac{1}{2} w_{\mathrm{L}} \left(3\bar{u}_{i,j,k} - \bar{u}_{i-1,j,k}\right) \\ &+ \frac{1}{12} w_{\mathrm{C}} \left(5\bar{u}_{i+1,j,k} + 12\bar{u}_{i,j,k} - \bar{u}_{i-1,j,k} - \bar{u}_{i,j-1,k} - \bar{u}_{i,j+1,k} - \bar{u}_{i,j,k-1} - \bar{u}_{i,j,k+1}\right) \\ &+ w_{\mathrm{R}} \left(\bar{u}_{i+1,j,k} + \bar{u}_{i,j,k}\right) \end{aligned} \tag{3.14}$$

$$\begin{aligned} u^{\mathrm{West}}_{i,j,k}(t^n) :=& p^n_i(x_{i-\frac{1}{2}}, y_j, z_k) = \frac{1}{2} w_{\mathrm{L}} \left(\bar{u}_{i,j,k} + \bar{u}_{i-1,j,k}\right) \\ &+ \frac{1}{12} w_{\mathrm{C}} \left(-\bar{u}_{i+1,j,k} + 12\bar{u}_{i,j,k} + 5\bar{u}_{i-1,j,k} - \bar{u}_{i,j-1,k} - \bar{u}_{i,j+1,k} - \bar{u}_{i,j,k-1} - \bar{u}_{i,j,k+1}\right) \\ &+ w_{\mathrm{R}} \left(-\bar{u}_{i+1,j,k} + 3\bar{u}_{i,j,k}\right) \end{aligned} \tag{3.15}$$

The interface point values in the y-direction (and the z-direction) are computed accordingly, holding x and z (respectively x and y) fixed.

3.1.2 Numerical method for the magnetic field

The KT base scheme has been demonstrated to produce spurious magnetic monopoles in two-dimensional non-symmetric test simulations [2]. The magnetic-field components must therefore be treated differently. Generally, three possible ways of computing the magnetic-field update have been developed in the past and are described and compared by Tóth in [71]. The methods available are projection methods, constrained

transport, and update of the magnetic field *via* its vector potential. The KT code uses a constrained transport method for the magnetic-field update as this numerical method automatically calculates a divergence-free update of the magnetic field rather than correcting spurious monopoles after they appear. A possible way of combining a constrained transport method with a central-difference scheme is described by Ziegler [78]. For this work, it has been adapted to the requirements and settings of the Kurganov-Tadmor base scheme in 2D and 3D.
In constrained transport, the cell averages of the magnetic-field components reside at the cell interfaces at staggered positions $-\frac{1}{2}$ (see Fig. 3.1). From a finite-volume discretization of the induction equation, the total time derivative of the magnetic-field components is given by

$$\frac{\mathrm{d}}{\mathrm{d}t} b^x_{i-\frac{1}{2},j,k} = -\frac{\bar{E}^z_{i-\frac{1}{2},j+\frac{1}{2},k} - \bar{E}^z_{i-\frac{1}{2},j-\frac{1}{2},k}}{\Delta y} + \frac{\bar{E}^y_{i-\frac{1}{2},j,k+\frac{1}{2}} - \bar{E}^y_{i-\frac{1}{2},j,k-\frac{1}{2}}}{\Delta z}, \tag{3.16}$$

$$\frac{\mathrm{d}}{\mathrm{d}t} b^y_{i,j-\frac{1}{2},k} = \frac{\bar{E}^z_{i+\frac{1}{2},j-\frac{1}{2},k} - \bar{E}^z_{i-\frac{1}{2},j-\frac{1}{2},k}}{\Delta x} - \frac{\bar{E}^x_{i,j-\frac{1}{2},k+\frac{1}{2}} - \bar{E}^x_{i,j-\frac{1}{2},k-\frac{1}{2}}}{\Delta z}, \tag{3.17}$$

$$\frac{\mathrm{d}}{\mathrm{d}t} b^z_{i,j,k-\frac{1}{2}} = -\frac{\bar{E}^y_{i+\frac{1}{2},j,k-\frac{1}{2}} - \bar{E}^y_{i-\frac{1}{2},j,k-\frac{1}{2}}}{\Delta x} + \frac{\bar{E}^x_{i,j+\frac{1}{2},k-\frac{1}{2}} - \bar{E}^x_{i,j-\frac{1}{2},k-\frac{1}{2}}}{\Delta y}, \tag{3.18}$$

where $\bar{E}$ are the line-averaged electric-field components defined at the cell edges. It can be shown, that by calculating the divergence of this definition of the time rate of change of the magnetic-field components, these terms pairwise cancel out. The time rate of change of the divergence of the magnetic field is zero. Therefore, when the divergence of the magnetic field is zero initially, it remains zero over time by the constrained transport update.
The next step is to find approximations to the electric-field components defined at the cell edges. By transforming the induction equation into divergence form with the antisymmetric flux tensor

$$\frac{\partial}{\partial t}\mathbf{b} = -\nabla \times \mathbf{E} = \nabla \cdot \begin{pmatrix} 0 & E_z & -E_y \\ -E_z & 0 & E_x \\ E_y & -E_x & 0 \end{pmatrix}, \tag{3.19}$$

and constructing numerical electric fluxes $\mathbf{E}^x$, $\mathbf{E}^y$, and $\mathbf{E}^z$ from the Kurganov-Tadmor flux formulation, electric-flux approximations at the cell interfaces are obtained. The numerical electric-flux vectors read as

$$\mathbf{E}^x_{i+\frac{1}{2},j,k} = \frac{1}{2}\left[\begin{pmatrix} 0 \\ -E_z \\ E_y \end{pmatrix}^{\mathrm{West}}_{i+1,j,k} + \begin{pmatrix} 0 \\ -E_z \\ E_y \end{pmatrix}^{\mathrm{East}}_{i,j,k}\right] - \frac{a^x_{i+\frac{1}{2},j,k}}{2}\left[\begin{pmatrix} b_x \\ b_y \\ b_z \end{pmatrix}^{\mathrm{West}}_{i+1,j,k} - \begin{pmatrix} b_x \\ b_y \\ b_z \end{pmatrix}^{\mathrm{East}}_{i,j,k}\right],$$

$$\mathbf{E}^y_{i,j+\frac{1}{2},k} = \frac{1}{2}\left[\begin{pmatrix} E_z \\ 0 \\ -E_x \end{pmatrix}^{\mathrm{South}}_{i,j+1,k} + \begin{pmatrix} E_z \\ 0 \\ -E_x \end{pmatrix}^{\mathrm{North}}_{i,j,k}\right] - \frac{a^y_{i,j+\frac{1}{2},k}}{2}\left[\begin{pmatrix} b_x \\ b_y \\ b_z \end{pmatrix}^{\mathrm{South}}_{i,j+1,k} - \begin{pmatrix} b_x \\ b_y \\ b_z \end{pmatrix}^{\mathrm{North}}_{i,j,k}\right],$$

$$\mathbf{E}^z_{i,j,k+\frac{1}{2}} = \frac{1}{2}\left[\begin{pmatrix} -E_y \\ E_x \\ 0 \end{pmatrix}^{\mathrm{Bottom}}_{i,j,k+1} + \begin{pmatrix} -E_y \\ E_x \\ 0 \end{pmatrix}^{\mathrm{Top}}_{i,j,k}\right] - \frac{a^z_{i,j,k+\frac{1}{2}}}{2}\left[\begin{pmatrix} b_x \\ b_y \\ b_z \end{pmatrix}^{\mathrm{Bottom}}_{i,j,k+1} - \begin{pmatrix} b_x \\ b_y \\ b_z \end{pmatrix}^{\mathrm{Top}}_{i,j,k}\right]. \tag{3.20}$$

The electric-field flux vectors $\mathbf{E}^{\mathrm{West}}$, $\mathbf{E}^{\mathrm{East}}$, etc. are computed by using the definition of the electric field

$$\mathbf{E}^{\mathrm{West}} = -\mathbf{v}^{\mathrm{West}} \times \mathbf{b}^{\mathrm{West}}.$$

From the components of the electric-field flux vector defined at the cell interfaces, the edge-centered electric-field components are reconstructed using a 2nd order interpolation.

$$\bar{E}^x_{i,j-\frac{1}{2},k-\frac{1}{2}} = \frac{1}{16}\left(-6E^y_{zi,j-\frac{1}{2},k} + E^y_{zi,j-\frac{1}{2},k+1} - 3E^y_{zi,j-\frac{1}{2},k-1} + 6E^z_{yi,j,k-\frac{1}{2}} - E^z_{yi,j+1,k-\frac{1}{2}} + 3E^z_{yi,j-1,k-\frac{1}{2}}\right) \tag{3.21}$$

$$\bar{E}^y_{i-\frac{1}{2},j,k-\frac{1}{2}} = \frac{1}{16}\left(6E^x_{zi-\frac{1}{2},j,k} - E^x_{zi-\frac{1}{2},j,k+1} + 3E^x_{zi-\frac{1}{2},j,k-1} - 6E^z_{xi,j,k-\frac{1}{2}} + E^z_{xi+1,j,k-\frac{1}{2}} - 3E^z_{xi-1,j,k-\frac{1}{2}}\right) \tag{3.22}$$

$$\bar{E}^z_{i-\frac{1}{2},j-\frac{1}{2},k} = \frac{1}{16}\left(-6E^x_{yi-\frac{1}{2},j,k} + E^x_{yi-\frac{1}{2},j+1,k} - 3E^x_{yi-\frac{1}{2},j-1,k} + 6E^y_{xi,j-\frac{1}{2},k} - E^y_{xi+1,j-\frac{1}{2},k} + 3E^y_{xi-1,j-\frac{1}{2},k}\right) \tag{3.23}$$

The line-averaged electric-field components defined at the cell edges are then used for the magnetic-field update equations (3.16)-(3.18).
The magnetic-field components used in the electric-field flux vectors (3.20) are reconstructed point values at the positions West, East, *etc.* . These point values have to be reconstructed from cell averages that are defined at staggered positions $-\frac{1}{2}$. This is done *via* a diagonal CWENO reconstruction. For example, the point values b^{West}_y, defined at $(i-\frac{1}{2},j,k)$ are reconstructed from their surrounding cell averages $\bar{b}_y$, located at $(i,j-\frac{1}{2},k)$ as

$$\begin{aligned} b^{\mathrm{West}}_{yi,j,k}(t^n) &= \frac{w_{\mathrm{DL}}}{2}\left(3\bar{b}_{yi,j-\frac{1}{2},k} - \bar{b}_{yi+1,j-\frac{3}{2},k}\right) \\ &+ \frac{w_{\mathrm{DC}}}{12}\left(5\bar{b}_{yi-1,j+\frac{1}{2},k} + 12\bar{b}_{yi,j-\frac{1}{2},k} - \bar{b}_{yi+1,j-\frac{3}{2},k} - \bar{b}_{yi+1,j+\frac{1}{2},k} - \bar{b}_{yi-1,j-\frac{3}{2},k} - \bar{b}_{yi,j-\frac{1}{2},k-1} - \bar{b}_{yi,j-\frac{1}{2},k+1}\right) \\ &+ \frac{w_{\mathrm{DR}}}{2}\left(\bar{b}_{yi-1,j+\frac{1}{2},k} + \bar{b}_{yi,j-\frac{1}{2},k}\right). \end{aligned} \tag{3.24}$$

Here, w_{DL}, w_{DC}, and w_{DR} are the nonlinear weights in diagonal direction. Correspondingly, the x- and z-components of the magnetic field are reconstructed at the cell interfaces.
The time rates of change of the conserved quantities at a time t^n are given by equations (3.1) and (3.16)-(3.18). The last step in the numerical scheme is the time integration of the update equations.

3.1.3 Time integration

The full set of ordinary differential equations of the conserved quantities is integrated in time using a 3rd order Runge-Kutta scheme. The particular choice that is used in the KT-code is a 3rd order Heun scheme. The code employs

$$\begin{aligned} u^{(1)} &= u^{(0)} + \frac{1}{3}\Delta t\ C\left[u^{(0)}\right] \\ u^{(2)} &= u^{(0)} + \frac{2}{3}\Delta t\ C\left[u^{(1)}\right] \\ u^{n+1} &= u^{(0)} + \frac{1}{4}\Delta t\ \left(C\left[u^{(0)}\right] + 3\ C\left[u^{(2)}\right]\right), \end{aligned} \tag{3.25}$$

with $u^{(0)} := u^n$. The supporting points in time are at $+\frac{1}{3}\Delta t$ and $+\frac{2}{3}\Delta t$. Thereby, the time integration helps to prevent the scheme from producing local under- and overshots, when compared to time-integration schemes that use supporting points at $+\frac{1}{2}\Delta t$ and $+1\Delta t$. The time step Δt is restricted by the Courant–Friedrichs–Lewy (CFL) criterion. As the base scheme computes maximum speeds of propagation, the global maximum of the local maximum speeds of propagation can be used to compute the time step as

$$\Delta t = \frac{C}{\sqrt{(\max(a^x_{i,j,k}))^2 + (\max(a^y_{i,j,k}))^2 + (\max(a^z_{i,j,k}))^2}}, \tag{3.26}$$

where $C < 1$ is the Courant number. The time step is dynamically allocated at each time step. The local maximum speed of propagation is defined in general form by equation (3.6) for a general set of coupled hyperbolic partial differential equations. In a given set of equations, it can be computed using physical information of the simulated system, knowing which physical phenomenon exhibits the highest speed of

propagation. In the case of isothermal hydrodynamics, the local maximum speed of propagation is the sound speed plus the absolute value of the local flow velocity in the according space direction:

$$a_{\mathrm{s}}^{x} = c_{\mathrm{s}} + |v_x|\,, \tag{3.27}$$

where c_{s} is the sound speed. In the case of MHD, the local maximum speed of propagation can be computed from the speed of the fast magnetosonic wave plus the absolute value of the local flow velocity as

$$a_{\mathrm{fms}}^{x} = \frac{1}{2}\sqrt{\frac{c_{\mathrm{s}}^2 + \mathbf{B}^2}{\rho} + \sqrt{\left(\frac{c_{\mathrm{s}}^2 + \mathbf{B}^2}{\rho}\right)^2 - \frac{4B_x^2 c_{\mathrm{s}}^2}{\rho}}} + |v_x|\,. \tag{3.28}$$

The local maximum speeds of propagation in the other space directions y and z are computed similarly. The base equations do not account for the viscous term in the momentum equation, nor for the resistive term in the induction equation. Viscosity and resistivity are introduced on a numerical level and are determined by the spatial reconstruction method. A detailed measurement of the numerical viscosity for the 1D and 2D Navier-Stokes equations, solved with 3rd order CWENO is described by Zhang *et al.* in [76].

3.2 Forcing

To maintain statistically steady-state turbulence, the constant energy loss due to grid viscosity and compressional losses has to be compensated for by injecting energy into the system. A random driving force is applied to the system to add energy at large scales. This random driving force is determined by a Ornstein-Uhlenbeck process in spectral space and is based on a method described by Schmidt *et al.* [62]. The coefficients of the Fourier transform of the velocity driving force $\hat{\mathbf{f}}(\mathbf{x})$ are computed by approximating the following stochastic differential equation:

$$\mathrm{d}\hat{\mathbf{f}}_v(\mathbf{k},t) = -\hat{\mathbf{f}}_v(\mathbf{k},t)\frac{\Delta t}{T} + F_v^0 \sum_{j,l,m}\left(\frac{2\sigma^2(\mathbf{k})}{T}\right)\delta(\mathbf{k}-\mathbf{k}_{j,l,m})\mathcal{P}_\zeta(\mathbf{k})\cdot d\mathcal{W}_t. \tag{3.29}$$

The parameter F_v^0 controls the amplitude of the velocity force, $\sigma(\mathbf{k})$ controls the spectral range and profile of the force, and $\mathcal{W}$ is the Wiener vector. The projection operator

$$\mathcal{P}_\zeta(\mathbf{k}) = \zeta\delta_{ij} + (1-2\zeta)\frac{k_i k_j}{k^2}, \tag{3.30}$$

controls the ratio of compressible to solenoidal forcing. Here, ζ is the spectral compressible *vs.* solenoidal weight. For $\zeta = 1$ the Wiener vector is projected perpendicular to $\mathbf{k}$ and the force becomes purely solenoidal. For $\zeta < 1$, the parallel component of $\hat{\mathbf{f}}_v$ to $\mathbf{k}$ is the compressional part of the force. The correlation time T is set to L/V, where L is the forcing length scale and V is the mean flow velocity of this length scale's fluctuations.
The Fourier coefficients of the magnetic-field force $\hat{\mathbf{f}}_b(\mathbf{k})$ are computed by

$$\mathrm{d}\hat{\mathbf{f}}_b(\mathbf{k},t) = -\hat{\mathbf{f}}_b(\mathbf{k},t) + F_b^0 \sum_{j,l,m}\left(\frac{2\sigma^2(\mathbf{k})}{T}\right)\delta(\mathbf{k}-\mathbf{k}_{j,l,m})\mathcal{P}_{\mathrm{mag}}(\mathbf{k})\cdot d\mathcal{W}_{b,t}, \tag{3.31}$$

where the magnetic projection operator $\mathcal{P}_\zeta$ always projects the Wiener vector perpendicular to both $\hat{\mathbf{f}}_v$ and $\mathbf{k}$. Thus, the forcing does not add cross-helicity to the turbulence [75], and the external forces satisfy

$$\hat{\mathbf{f}}_b(\mathbf{k},t)\cdot\hat{\mathbf{f}}_v(\mathbf{k},t) = 0. \tag{3.32}$$

The parameter F_b^0 controls the amplitude of the magnetic-field force. The forcing method described allows for control over magnetic to kinetic energy-injection ratio, the mean total-energy injection, and the solenoidal versus dilatational force for the kinetic energy.

4. CODE PROPERTIES

In this Chapter the properties of the KT-code are described. Besides the code's scaling properties, the shock-capturing capability and the convergence of the code are demonstrated. Finally, the results of benchmarking studies against current state-of-the-art astrophysical codes are presented. In the benchmarking, a high sonic Mach number test-problem of decaying hydrodynamic and MHD turbulence is solved. The results from the chosen test-problem are good indicators for the capabilities of the presented KT-code to simulate highly compressible turbulence.

4.1 Parallelization and scaling

The resolution of direct numerical simulations of turbulence determines the numerical viscosity and thereby the separation of scales in the turbulent system. The separation of scales is defined as the spectral width between scales that are affected by *e.g.* the forcing or the boundaries on the one hand, and the dissipation scales on the other hand. Achieving high spatial resolution is therefore not only important to keep the discretization error small, but also influences the physical behavior of the system. Parallelization, the distribution of the computational domain over a number of processes, makes the computation of high-resolution simulations possible.
The KT-code is MPI parallel, using a two-dimensional decomposition of the computational grid. The 2D decomposition is commonly referred to either as the pencil decomposition or column decomposition. It is used when the number of processes comes close to, or even exceeds, the number of grid cells in one spatial dimension. In two of the three space dimensions the grid is divided and distributed over the processes. The third dimension resides entirely within each process. The number of ghost cells, the cells that are only needed for the local computation of the first real edge grid cells, is two in the case of the hydrodynamic KT-code and four in the case of the MHD KT-code. The difference in number of ghost cells stems from the enlarged numerical stencil of the constrained transport scheme of the MHD code (the ghost-cells are described in detail in Appendix B). The ghost-cell values are determined during each Runge-Kutta time-step according to the edge grid-values of the neighboring processes' edge cells. Figure 4.1 depicts how the KT-code's parallelization is organized.
The scaling describes the function of the speedup in computation time when increasing the number of

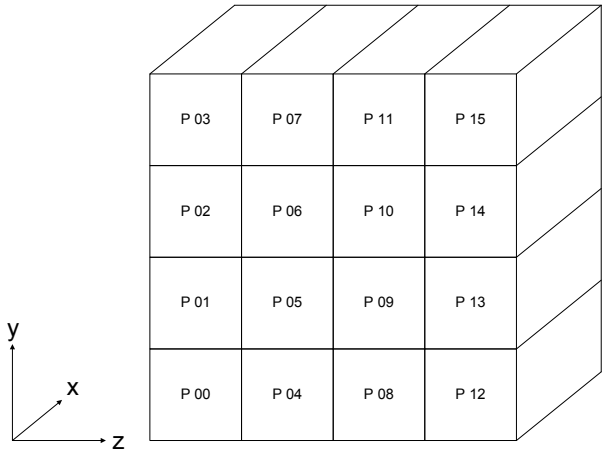

Fig. 4.1: KT-code's column decomposition of the computational domain. In this example of 16 processes (labeled P00-P15), the domain is distributed over a 4×4 grid of processes in the y- and z-directions. The x-direction is handled completely by each process.

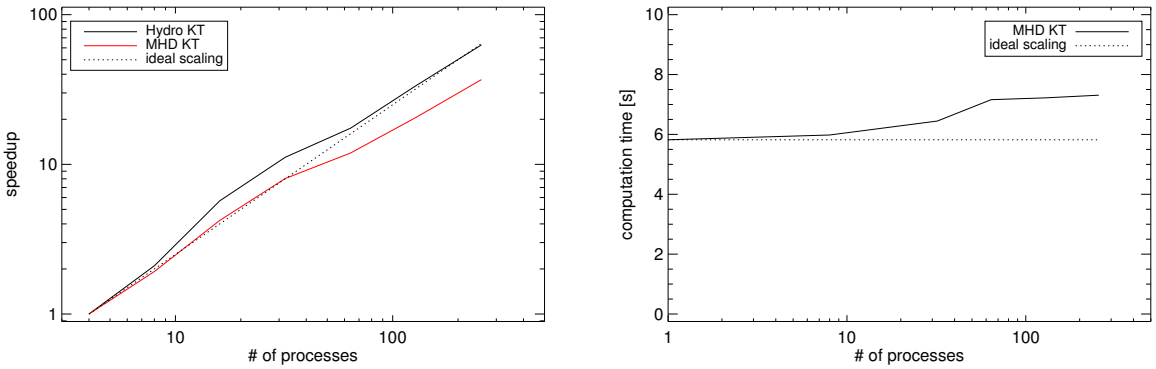

Fig. 4.2: Scaling of the Hydro KT and MHD KT-code. The plot to the left shows the speedup when computing a fixed time interval in a 256^3 simulation with an increasing number of processes. The right-hand plot shows the computation time of a single time-step when the total number of grid cells per process is held constant.

processes. The number of ghost cells is critical in determining the scaling behavior of the code. Each process computes the values of the real grid cells as well as the values of the ghost cells. At fixed resolution, the total number of ghost cells increases with the number of processes, and thus the measured scaling deviates from the ideal scaling. Additionally, the MPI communication effort increases with the number of processes used for a given total resolution, as the edge-located real grid-cells are copied to the neighboring processes' ghost cells. The scaling behavior of the KT-code is shown in Figure 4.2 for both the hydrodynamic case and the MHD case. The speedup is measured for a constant grid resolution of 256^3, varying the number of processes from 4 to 256. Ideally, the computation time is reduced by half when the number of processes is doubled. The initially faster-than-ideal speedup results from an improved usage of cache when the number of cells computed by one individual process decreases. In order to avoid this effect, the Figure 4.2 also shows the time used for computing a single time step when each process computes a constant number of grid cells. The resolution is thus increased according to the number of processors, going from 64^3 for one process to $512 \times 512 \times 256$ for 256 processes. For a code that scales perfectly, the computation time for a single time step would be constant. An increased effort of communication and ghost cell computation is reflected in the $\sim 20\%$ increase in computation time (see RHS of Figure 4.2).
Both plots show a sudden change of scaling behaviour between 32 processes and 64 processes. This change is not an effect of the code but due to the architecture of the parallel computer that was used to measure the scaling behavior. Up to 32 processes are computed in single thread mode, meaning that one physical CPU (consisting of two logical CPUs) computes one process. For 64 processes and larger, one logical CPU computes one process. The code's scaling behavior is thus best reflected in the measured scaling ranging from 64 to 256 processes. In this range of processes, the code's speedup is very close to the ideal scaling.

4.2 Convergence test

The convergence of the KT-code in three spatial dimensions is tested by simulating a 3D analytically-known solution to the ideal MHD equations using an adiabatic equation of state. The test problem is a nonlinear self-similar expansion of a magnetized plasma ball proposed by Lou, Rosner, and Ulmschneider [45].
The basic MHD equations in the adiabatic case and in Gaussian units are

$$\partial_t \rho + \nabla \cdot (\rho \mathbf{v}) = 0, \tag{4.1}$$

$$\partial_t (\rho \mathbf{v}) + \nabla \cdot \left[\rho \mathbf{v}\mathbf{v}^T + \left(p + \frac{1}{8\pi} |\mathbf{B}|^2 \right) I - \frac{1}{4\pi} \mathbf{B}\mathbf{B}^T \right] = 0, \tag{4.2}$$

$$\partial_t e + \nabla \cdot \left[\left(e + p + \frac{1}{8\pi} |\mathbf{B}|^2 \right) \mathbf{v} - \frac{1}{4\pi} (\mathbf{v} \cdot \mathbf{B}) \mathbf{B} \right] = 0, \tag{4.3}$$

$$\partial_t \mathbf{B} + \nabla \times \mathbf{E} = 0. \tag{4.4}$$

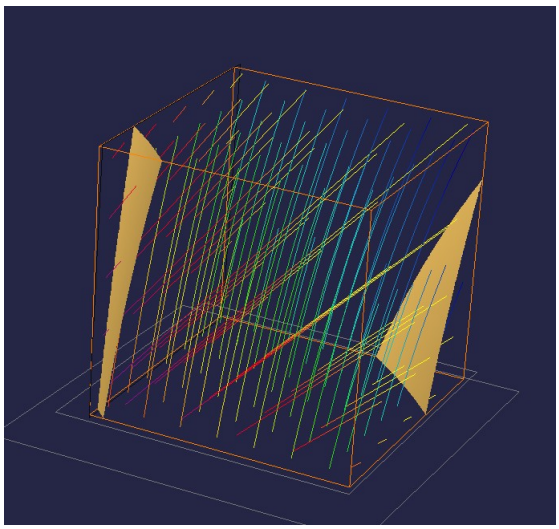

Fig. 4.3: The domain of the convergence-test calculations at $t = 1,000$ s. Illustrated are the density isosurfaces, the magnetic field and the momentum.

The set of equations (4.1)-(4.4) is given in standard notation of the magnetic field $\mathbf{B}$, the mass density ρ, the total energy density e, the velocity $\mathbf{v}$, and the electric field $\mathbf{E} = -\mathbf{v} \times \mathbf{B}$. Thermal pressure p is computed from an ideal gas equation of state

$$p = (\kappa - 1)\left(e - \frac{1}{2}\rho\left|\mathbf{v}\right|^2 - \frac{1}{8\pi}\left|\mathbf{B}\right|^2\right), \tag{4.5}$$

with the ratio of specific heats $\kappa = 4/3$.
In Cartesian coordinates, the evolution of the magnetized plasma ball is

$$\rho = \phi^{-3}\frac{2F_0^2}{\alpha\pi}\left\{7\frac{x^2+y^2}{\phi^2}\left[\frac{r^2}{\phi^2} - a^2\right]^2 + a^6\right\}, \tag{4.6}$$

$$\mathbf{v} = \phi^{-1}\left[\frac{\eta\phi - 2\alpha}{\phi}\right]^{\frac{1}{2}}\begin{pmatrix} x \\ y \\ z \end{pmatrix}, \tag{4.7}$$

$$\mathbf{b} = \frac{2F_0(\zeta^2 - a^2)}{\phi^2 r^2}\left[(\zeta^2 - a^2)\begin{pmatrix} xz \\ yz \\ z^2 \end{pmatrix} - (3\zeta^2 - a^2)\begin{pmatrix} -xz \\ -yz \\ x^2 + y^2 \end{pmatrix}\right], \tag{4.8}$$

$$p = \phi^{-3}\frac{F_0^2}{\pi}\left[(5a^2 - 7\zeta^2)(\zeta^2 - a^2)^2\zeta^2(1 - \frac{z^2}{r^2}) + a^6(a^2 - \zeta^2)\right], \tag{4.9}$$

where F_0 and a are positive constants, α and η are constants of integration, and r is the radius. ζ is the radius divided by ϕ and ϕ is a function of the time t. Time t can be obtained numerically from

$$t - t_0 = \frac{1}{\eta}\sqrt{\phi(\eta\phi - 2\alpha)} + \frac{2\alpha}{\eta\sqrt{\eta}}\log(\sqrt{\eta\phi} + \sqrt{\eta\phi - 2\alpha}). \tag{4.10}$$

Test calculation parameters are chosen to be $a = 125,000$ cm, $F_0 = 3 \cdot 10^{-18}$ gauss cm^{-4}, $\alpha = 2 \cdot 10^{-5}$ s^{-2}, and $\eta = 4 \cdot 10^{-5}$ s^{-2}. The spatial domain of the calculation is a cube with an edge length of $80,000$ cm. The center of the cube is located at $x = 140,000$ cm, $y = 140,000$ cm, and $z = 160,000$ cm. The calculation starts at $t_0 = 1,000$ s and ends at $t_{\text{final}} = 1,025$ s. For the given set of parameters the flow velocity is estimated as $v \sim 30$ cm s^{-1}, the density $\rho \sim 0.01$ g cm^{-3}, the magnetic field $b \sim 35$ gauss and the gas pressure $p \sim 100$ dyne cm^{-2}. Figure 4.3 illustrates the density, the magnetic field and the momentum of the plasma ball in the computational domain at $t = 1,000$ s. The physical variables at the boundaries are calculated using the analytic solution. Due to the 3rd order Runge Kutta time integration, the analytical solution at the boundaries is calculated at each Runge Kutta step. The test setup is repeated for spatial resolutions ranging from 32^3 up to 512^3. Due to the dynamic time-step allocation

of the numerical scheme, the number of time-steps needed to reach the final time t_{final} doubles with the resolution. A total number of seven time-steps is needed to compute the time evolution of the flow from t_0 to t_{final} at 32^3 resolution. 137 steps are needed to resolve the same time interval at 512^3 resolution. For each run, the maximum relative deviance of the numerical solution from the analytically obtained solution is computed at time t_{final}. Besides the maximum relative deviance, the mean absolute deviance normalized to the value of the quantity is calculated. The normalized mean absolute deviance is referred to as the mean relative deviance. In addition to the deviances for a fixed time-interval run, the errors of a single time-step are measured.

4.2.1 Results of the convergence test

The mean relative deviance of the KT-code's scheme converges with the order of approximately 3 for a single time step and approximately 2.6 for the whole time interval (see LHS of Figures 4.4 and 4.5). This result matches the expected order of convergence, because the 3rd order CWENO reconstruction of point values is the limiting factor. The slightly lower order of convergence in the maximum relative deviance (illustrated on the RHS of Figures 4.4 and 4.5), compared to the mean relative deviance can be explained by the way the ghost-cell values at the boundaries are set at the intermediate Runge Kutta steps. The ghost-cell values are set using the analytical solution, while grid cells located near the boundaries are evolved by the numerical scheme. An artificial, though small, discontinuity is maintained between the first simulated real grid cells and the neighboring ghost-cells. In the vicinity of discontinuities, the smoothness indicators of the CWENO scheme reduce the order of the reconstruction from 3rd order to 2nd order, thus an artificial reduction of the order of convergence is maintained at the computational domain boundaries.
When the constrained transport scheme is used to update the magnetic field, the step of averaging of the electric-field flux at the edges of the grid introduces an additional source of error, effectively reducing the order of convergence by approximately 0.2 compared to a pure Kurganov-Tadmor scheme.
At the lowest resolution, the normalized mean relative deviance varies from 10^{-5} to 10^{-6}. At the highest

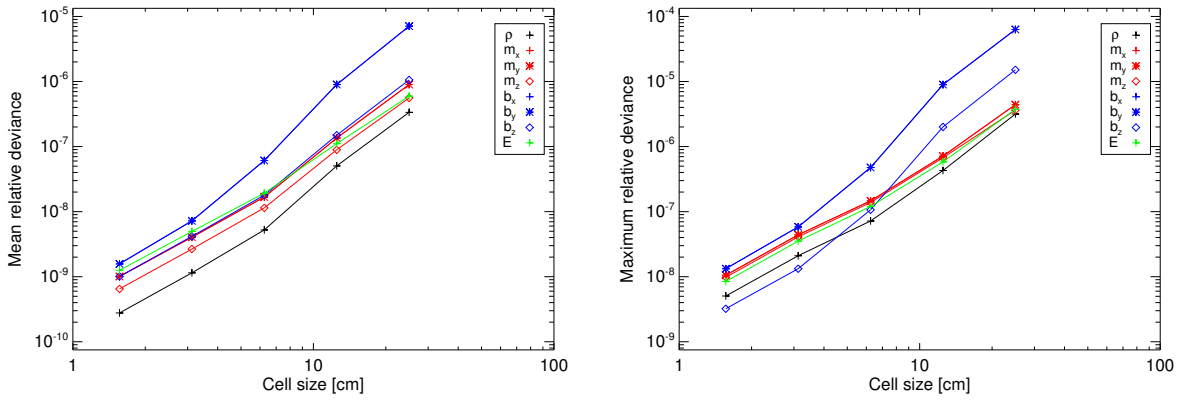

Fig. 4.4: Mean and maximum relative deviation *vs.* grid cell size dx for a fixed time interval. The order of convergence is approximately 2.6 for the mean relative deviance and approximately 2.3 for the maximum relative deviance.

resolution, the mean relative deviance does not exceed 10^{-8}. For a single time-step, the mean relative deviance does not exceed 10^{-10} at the highest resolution. The maximum relative error does not show the same convergence behavior due to the erroneous effect of the analytical boundary values.

In order to evaluate the effect of constrained transport on the convergence behavior of the full hybrid scheme, the convergence is also tested using the base Kurganov-Tadmor scheme for the full set of equations (4.1)-(4.4). Any spurious magnetic monopoles are small compared to the magnitude of the magnetic field, because the magnetized plasma ball is a smooth solution, showing no discontinuities. The pure KT algorithm shows slightly lower errors and a slightly higher order of convergence ($O(\Delta x) \approx 3.2$ for a single time-step). At the same time, the erroneous divergence of the magnetic field reaches values of 10^{-6}. The constrained transport scheme keeps the maximum of the divergence of the magnetic fields

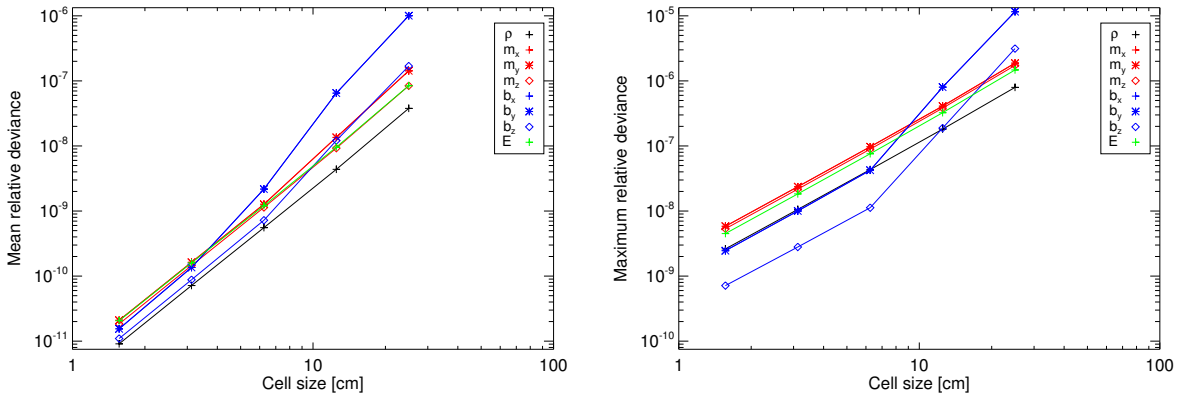

Fig. 4.5: Mean and maximum relative deviation *vs.* grid cell size dx for a single time step. The order of convergence is approximately 3 for the mean relative deviance and approximately 2.1 for the maximum relative deviance.

as low as $2 \cdot 10^{-15}$.

4.3 Shock-capturing in 2D test-problems

One of the main important properties of compressible codes is the ability of the numerical scheme to capture shock-waves. A jump of *e.g.* the mass density has to be maintained over time, propagating through the computational domain. The discretization of a discontinuous function is prone to lead to numerical artifacts, often leading to spurious oscillations of the shocked quantity in the vicinity of the shock front. Over time, the distinct jump is also prone to be smeared out spatially by the numerical scheme. In order to demonstrate the shock capturing ability of the KT-code, the shock evolution in a standard two-dimensional MHD test problem, the Orszag-Tang vortex [2], is analyzed. The Orszag-Tang vortex is a supersonic eddy with initially homogeneous mass density, that decays over time. An adiabatic equation of state is used to allow for mass-density fluctuations to steepen into shocks. The initial state of the system is set to:

$$\begin{pmatrix} \rho \\ v_x \\ v_y \\ v_z \\ b_x \\ b_y \\ b_z \\ p \end{pmatrix} = \begin{pmatrix} c_{\mathrm{O}} \\ \sin 2\pi y \\ \sin 2\pi x \\ 0 \\ -\sin 2\pi y \\ \sin 4\pi x \\ 0. \\ \frac{1}{2} c_{\mathrm{O}}^{1/2} \end{pmatrix}. \tag{4.11}$$

The constant $c_{\mathrm{O}} = 5^2/(6^2\pi)$, is chosen as proposed by Mignone [48]. The ratio of specific heats is chosen to be $\kappa = 5/3$, for an ideal gas. The initial state is chosen to provide an initial thermal to magnetic pressure of $10/3$. The time t is given in units of the initial average sound-speed. The test problem is solved on a $[0,1] \times [0,1]$ grid with periodic boundary conditions. Results are shown for a spatial resolution of 1024^2. Orszag-Tang simulations at lower resolution have been carried out to test the influence of the grid viscosity.

The supersonic flow leads to shocks. Figure 4.6 shows the distribution of the mass density shortly after the density fluctuations have steepened into shocks. Figure 4.7 displays the 1D-cut for the values of the mass density, the velocity components, and the magnetic-field components, respectively. A one-dimensional cut through the results at $y = 0.75$ and $t = 0.4$ is used to depict the jumps of the downstream to upstream values of the flow quantities. Two shock fronts of the density can be seen at $x = 0.12$, and at $x = 0.67$. The mass-density shock at $x = 0.67$ is a jump from 0.17 to 0.37 within four grid points in x-direction. The solution left and right to the shock front is smooth, showing no spurious oscillations. The x-component of the velocity jumps from a value of -0.23 to a value of -1.1 within the same range

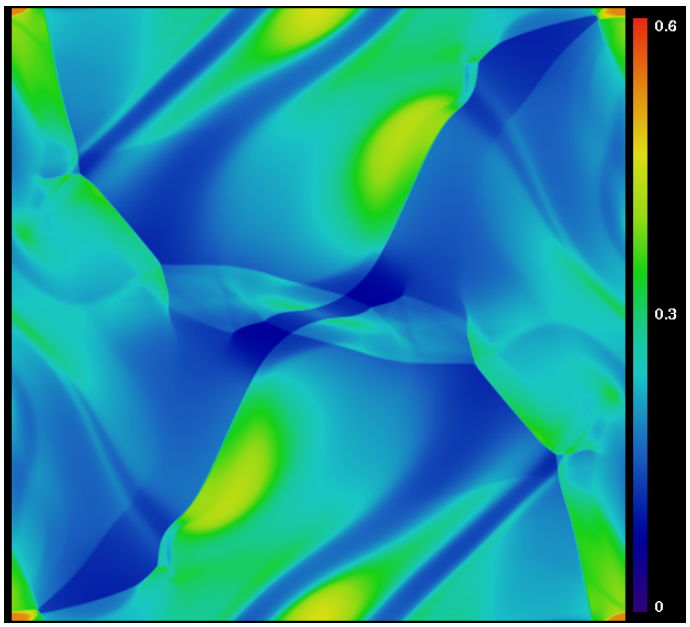

Fig. 4.6: Mass density at $t = 0.4$ in the Orszag-Tang vortex. The density shocks are thin transition layers where the mass density jumps from the upstream to the downstream value.

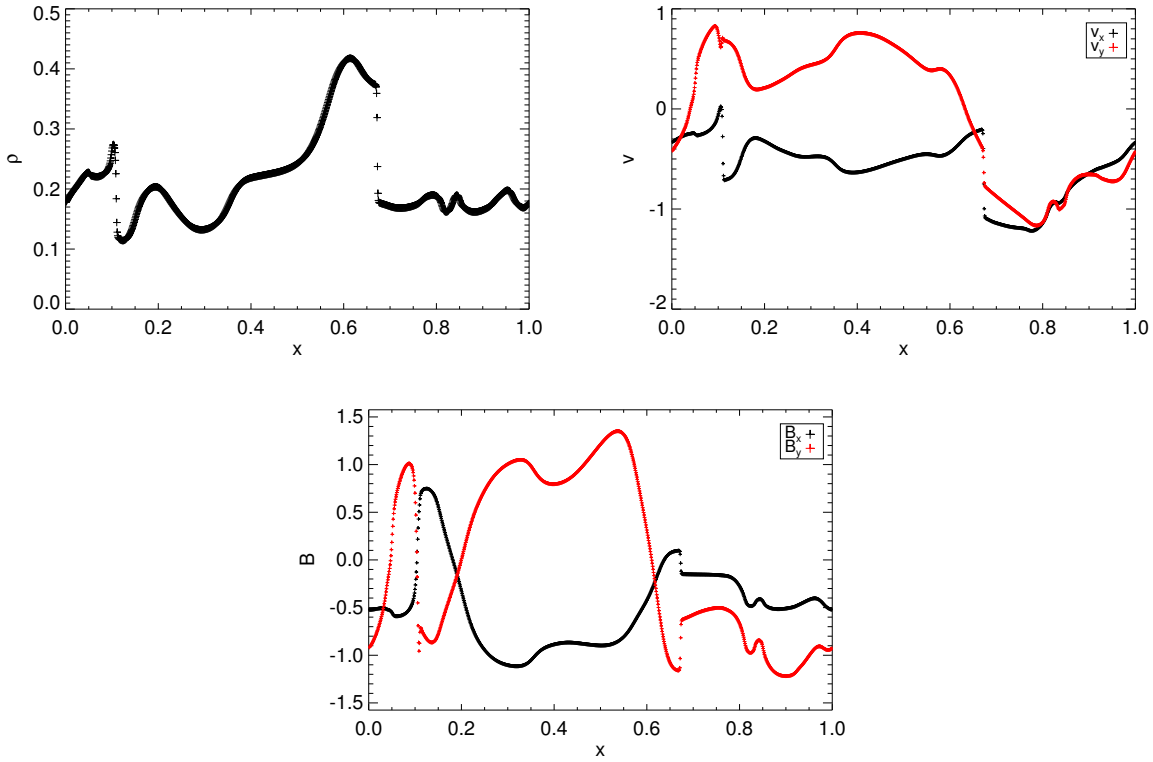

Fig. 4.7: 1D-cut through the Orszag-Tag vortex at $t = 0.4$, $y = 0.75$. The plots show the spacial distribution of the density field and the components of the velocity field and the magnetic field. At the discontinuity at $x = 0.67$, the flow quantities jump from the upstream to downstream value.

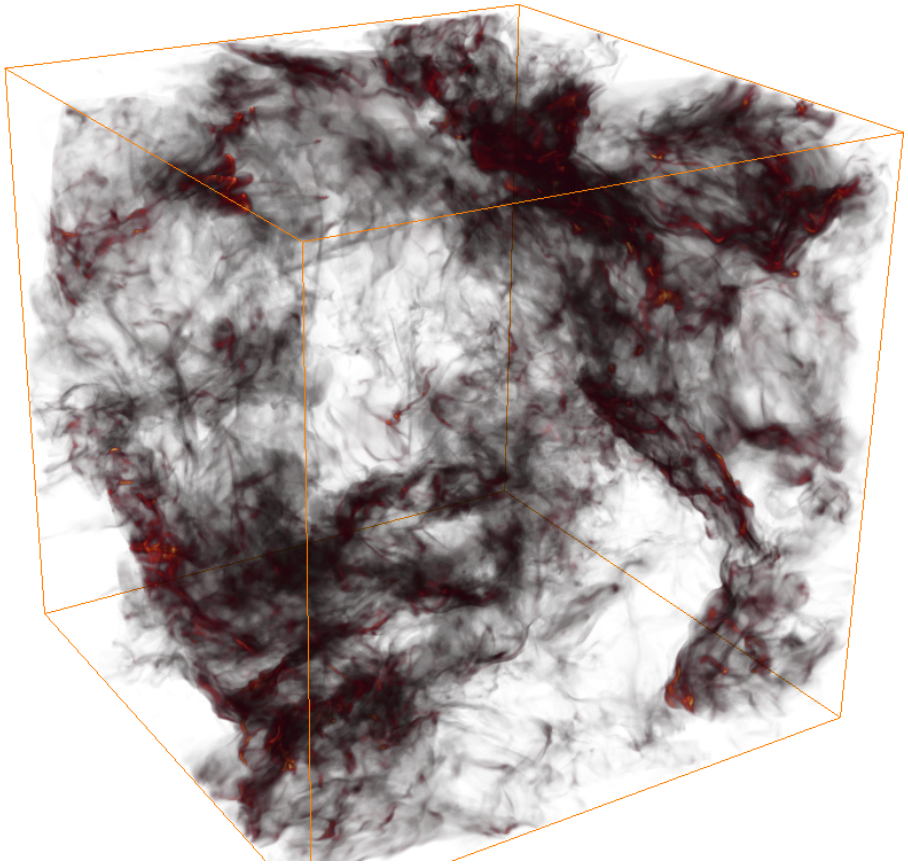

Fig. 4.8: The density field in the MHD star-formation test problem, resolution of 1024^3, after 0.2 dynamical times. The average sonic Mach number is approximately 8. The bright yellow regions correspond to a mass-density above 10^3, while the transparent parts indicate a mass-density as low as 10^{-3}.

of grid points, while the y-component jumps from -0.4 to -0.77. Also the magnetic-field components show a discontinuity at $x = 0.67$. While the x-component change is negative and changes from 0.1 to -0.15, the y-component change of the magnetic field is positive (from -1.15 to -0.62).
Following the evolution of the flow in time, the shock fronts propagate through the system until turbulence sets in and dissipates the flow energy, eventually. During the propagation of shocks, the steepness of the gradients of the flow quantities is maintained, and not smeared-out by the numerical scheme.
The Orszag-Tang vortex tests also reveals that the magnetic field is maintained divergence-free, even in the vicinity of shocks. The measured maximum divergence of the magnetic field is kept as low as 10^{-12}.

4.4 Benchmarking - star formation test problem

The KT-code has been benchmarked against current cutting-edge hydro and MHD codes, simulating 3D decaying turbulence. The initial condition of the test-problem is fully developed Mach 9 turbulence, studied with and without magnetic field. The turbulence decays over approximately two dynamical times, *i.e.* flow-crossing times. The equation of state is isothermal, resolutions of 256^3, 512^3, and 1024^3 have been tested for both the hydro and the MHD case. The boundary conditions are periodic in three spatial dimensions, the average mass-density is one, and the sound speed is set to one. The time is given in units of the sound speed. For the initial data snapshot, the time is set to $t = 0$.

For each run, 10 snapshots in equidistant time-intervals are taken in order to compare the evolution of the flow among the solvers. Figure 4.8 shows the spatial mass-density distribution after 0.2 flow crossing times (*i.e.* $t = 0.02$ in units of sound speed) of the decaying MHD simulation result of the KT-code. For data analysis purposes, power spectra, structure functions, density PDFs, and box averages are computed for each snapshot. The codes that have participated in the benchmarking are:

- ENZO
- FLASH
- RAMSES
- PPML
- ZEUS
- PHANTOM
- KT

All codes participating in this benchmarking study are grid codes, with the exception of PHANTOM, which is a Smoothed Particle Hydrodynamics (SPH) code. The codes chosen for this study provide a cross-section of the numerical schemes currently used in the field. PPML, ENZO, and FLASH are based on piecewise parabolic methods (PPM). RAMSES is an unsplit Godunov-scheme with adaptive-mesh refinement (AMR). Zeus is a widely used astrophysical code whose HD and MHD algorithms are based on the method of finite-differences on a staggered mesh. Further description of the codes can be found in [53], [27], [70], [51], [60].
By comparing results from the test-problems, advantages and disadvantages of the various numerical approximation methods are revealed. The comparison also helps to understand which numerical artifacts are produced and how they affect the evolution of the flow. The physically meaningful part of the solution can be identified, supporting the reliability into the simulation results of statistically stationary turbulence in Chapter 6.
The KT-code test-simulations have been carried out on a IBM Power6 575 computer. Table 4.1 shows the number of processors and the according computational effort of the simulation runs.

Run	# of processors	computation time
Hydro 256^3	64	0 days:4h:34min
Hydro 512^3	256	0 days:19h:8min
Hydro 1024^3	1024	2 days:23h:58min
MHD 256^3	64	0 days:5h:21min
MHD 512^3	256	0 days:21h:50min
MHD 1024^3	1024	5 days:10h:29min

Tab. 4.1: Number of processes and computational resources for the benchmarking simulation runs.

4.4.1 Results of the decaying hydrodynamic turbulence

In the absence of magnetic fields, the initial flow at a sonic Mach number of 9 decays to a Mach 2 turbulence within two flow-crossing times. Figure 4.9 shows power spectra at four 1024^3 snapshots for the velocity, the mass-density, the density-weighted velocity $|\rho^{1/3}v|^2$ and kinetic-energy $|\rho^{1/2}v|^2$. The power spectra of the captured quantities are shown in compensated plots, *i.e.* multiplied by k^a with the compensation exponent a. The compensation exponents are 2, 5/3, and 3/2, respectively. The density power-spectra are uncompensated.

The spectrum on top of the lines corresponds to the initial data snapshot at t_0. As the turbulence decays over time, the energy is gradually dissipated and the according power-spectra contain less and less energy. It can be referred from *e.g.* the kinetic-energy spectra that the dissipative length-scale sets in at $k \approx 30$ or $\log(k/k_{\min}) \approx 1.5$. In the dissipation range of scales with $k > 30$, the power spectra fall off steeply. The functional shape of this fall-off is determined by the grid viscosity of the numerical scheme. In the range of $2 < k < 30$, all spectra display a power-law scaling, an approximately straight line in the log-log plots. Within the scaling range, the power-spectra follow the functional relation:

$$E(k) \sim k^{-\beta}. \tag{4.12}$$

Here, E(k) is used as the general term of a 1D power spectrum of a flow quantity.
While the velocity power-spectra become flatter over time (showing a scaling-exponent of $\beta \approx 2$, initially),

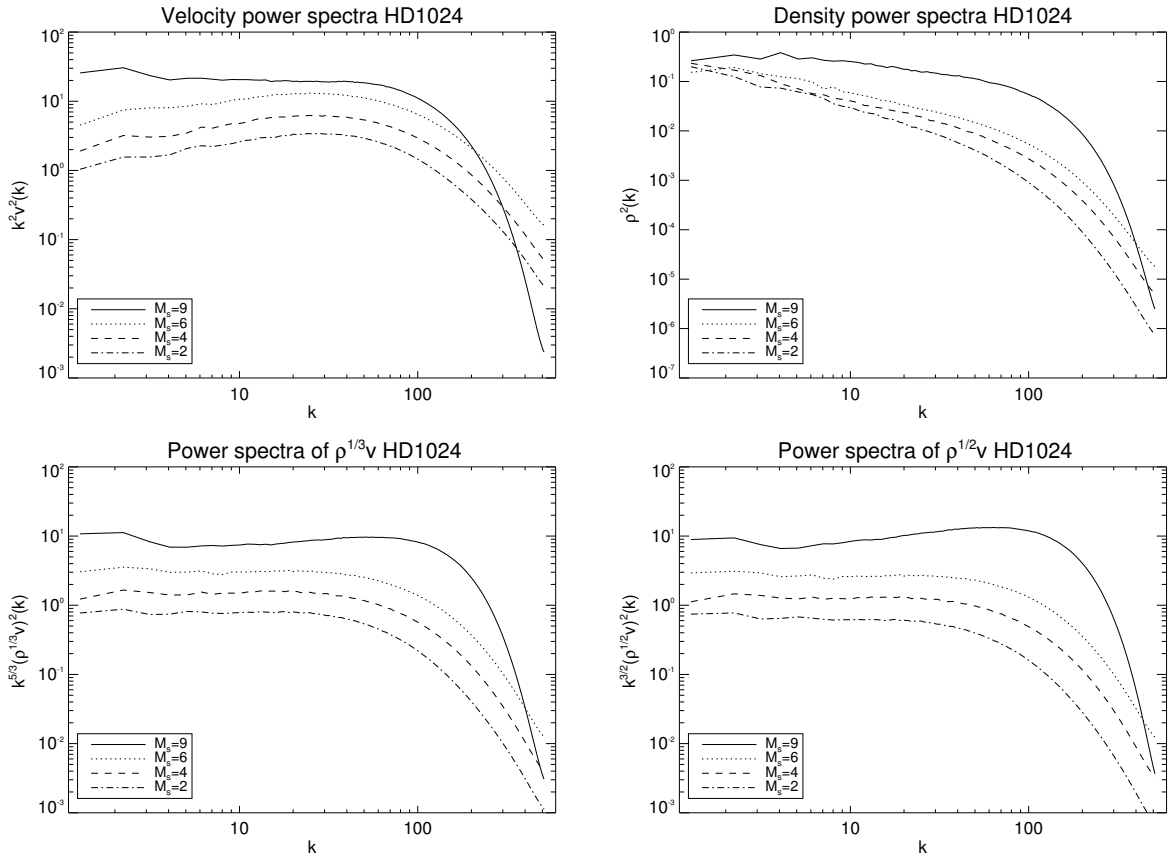

Fig. 4.9: Power spectra of the velocity, the mass-density, the density-weighted velocity, and the kinetic-energy spectra at 4 snapshots from $t_0 = 0.0$ to $t_f = 0.2$. The density power-spectra are uncompensated, the velocity spectra are compensated with k^2. The power-spectra of the density-weighted velocity are compensated with $k^{5/3}$ and the kinetic-energy spectra are compensated with $k^{3/2}$.

the kinetic energy spectra become steeper. The power-spectra of the density-weighted velocity show no obvious change of the scaling-exponent over time. The mass-density power-spectra also show a scaling behavior in the spectral range $2 < k < 30$. With decreasing RMS Mach number, the density power-spectra become steeper. The obtained scaling behavior is present in the results of the other grid codes as well. However, the scaling of snapshot-spectra does not contain statistical relevant information, since the spectra are not time averaged. Additionally, the turbulence is decaying and not statistically stationary.

4.4.2 Results of the decaying MHD turbulence

In the case of decaying MHD turbulence, the initially fully-developed Mach 9 turbulence also decays rapidly to a sonic Mach number of 2, within two flow-crossing times. In addition to the power spectra of the hydrodynamic quantities described in Chapter 4.4.1, the magnetic-energy spectra are measured. The spectral shape of the power spectra is shown in Figure 4.10. The compensation factors of the spectra correspond to those of the hydrodynamic case.

The kinetic energy shows a spectral fall-off for wave-numbers greater than 30 and a self-similar range for $2 < k < 30$. In the near-dissipation range of wave-numbers $10 < k < 30$, power spectra show a bump, a flatter scaling than in the range of wave-numbers $2 < k < 10$. This bump is referred to as bottleneck phenomenon. The power spectra indicate that the bottleneck phenomenon is more prominent in the MHD case than in the hydro case. This bottleneck phenomenon is present in most of the compressible codes and is attributed to the way that numerical viscosity scales with the wave-number k in the dissipation range. According to Falkovich [23], the bottleneck phenomenon is more pronounced when dissipation grows faster than k^2. The KT-codes' dissipation is determined by the numerical viscosity of the central-difference scheme and grows faster than k^2. This can be derived from the comparison of the velocity power-spectra of all participating codes (see Figure 4.12). The numerical dissipation of the

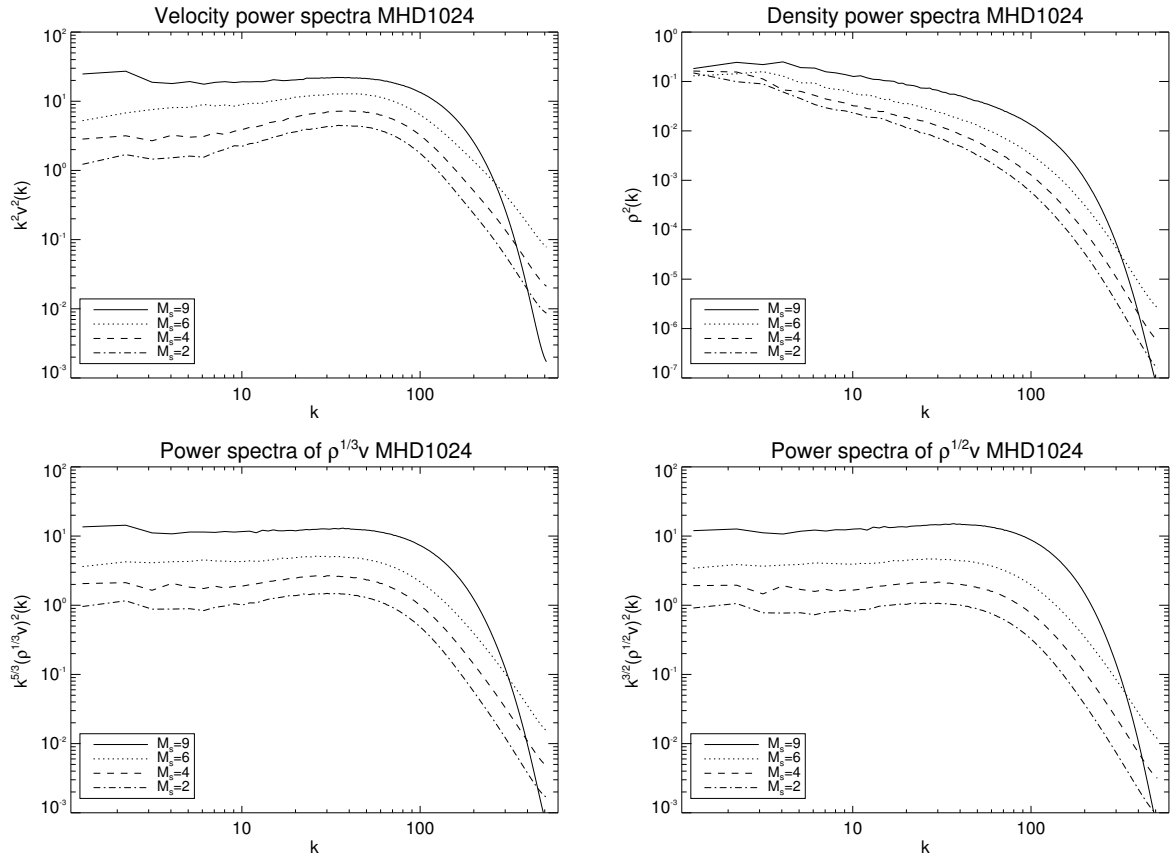

Fig. 4.10: Power spectra of the velocity, density, density-weighted velocity and kinetic energy at 4 snapshots from $t_0 = 0.0$ to $t_f = 0.2$. The mass-density spectra are uncompensated, the velocity power-spectra are compensated with k^2. The power spectra of the density-weighted velocity are compensated with $k^{5/3}$ and the kinetic-energy spectra are compensated with $k^{3/2}$.

KT-code is similar to the dissipation of the PPM codes and the Zeus code. That means that numerical dissipation grows faster than k^4, which is the measured scaling of the numerical dissipation of the PPM schemes [36].

Figure 4.11 shows four snapshots of power spectra of the magnetic field. The power spectra of the magnetic field do not display a power-law scaling. The magnetic energy-density is largest for large scales ($1 < k < 4$) and drops off more and more steeply towards smaller scales.

A comparison of the velocity power-spectra at one given snapshot among the solvers is a good basis for comparing the various numerical approximation methods. Figure 4.12 shows the effective velocity-bandwidth of 256^3 results of the codes at snapshot $t = 0.01$. The velocity power-spectra are divided by the reference solution. The reference solution is the result at $t = 0.01$ of the 1024^3-run of the ENZO code. The spectra are plotted *vs.* $\log(k/k_{\min})$. In the range of large scales, with $\log(k/k_{\min}) < 0.5$, most of the codes produce velocity power-spectra with good agreement to the reference solution. However, the PHANTOM code shows a marked deviation from the reference solution. Since PHANTOM it is a SPH code, this effect will not be discussed further. In the range of $0.5 < \log(k/k_{\min}) < 0.9$, the RAMSES code and the KT-code reveal a flattening of the spectrum, which can be attributed to the bottleneck phenomenon. Numerical dissipation affects scales where $\log(k/k_{\min}) > 0.9$. For the KT-code, the functional form of the dissipation-scale spectrum corresponds well to those of the RAMSES and Zeus codes. The KT-code's dissipative fall-off is slightly steeper than the fall-off of the spectra of the PPML codes. The resulting effective bandwidth indicates that the power spectra obtained by the KT-code are comparable to those obtained by computationally more expensive Riemann solvers such as RAMSES or the ENZO code.

While single snapshot-data allows a comparison of spectral properties of the schemes, the time evolution of ensemble averages allow a comparison of time-evolution properties of the codes. A comparison among solvers of the evolution of the square of total vorticity (or enstrophy) and the square of the total curl

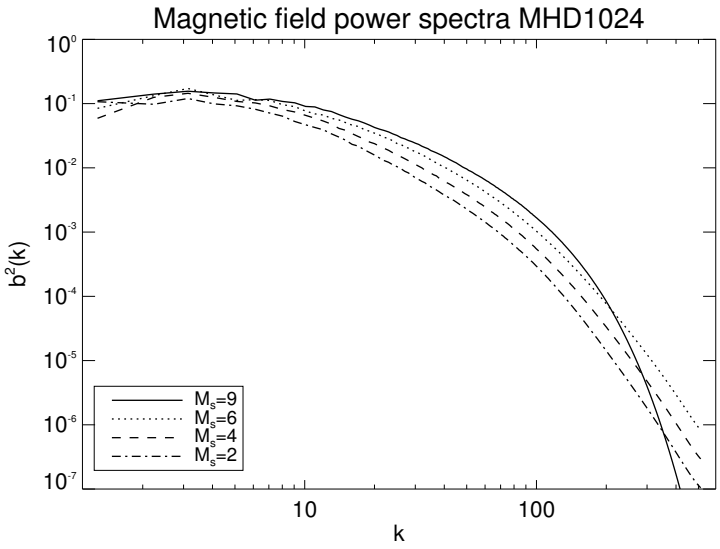

Fig. 4.11: Uncompensated power spectra of the magnetic field at 4 snapshots, from $t_0 = 0.0$ to $t_f = 0.2$

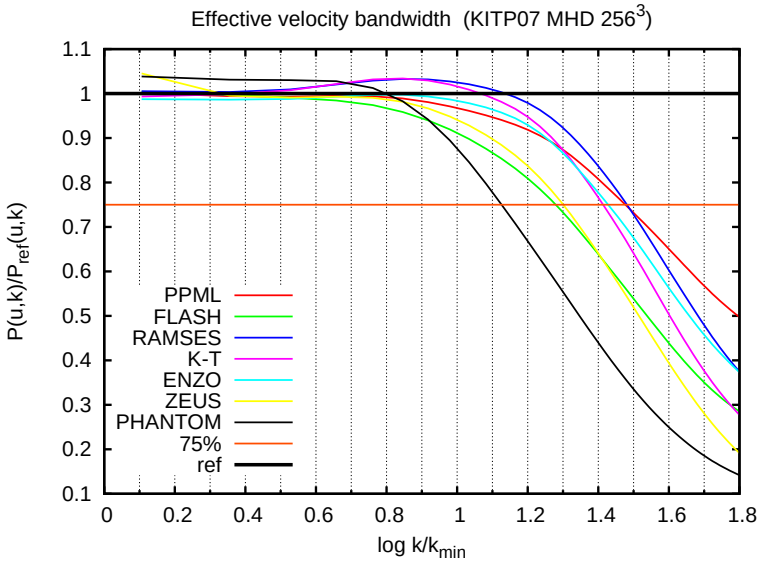

Fig. 4.12: Effective velocity bandwidth of the participating codes' simulation results at $t = 0.1$ (Courtesy of A. Kritsuk, yet unpublished KITP07 star-formation benchmarking results).

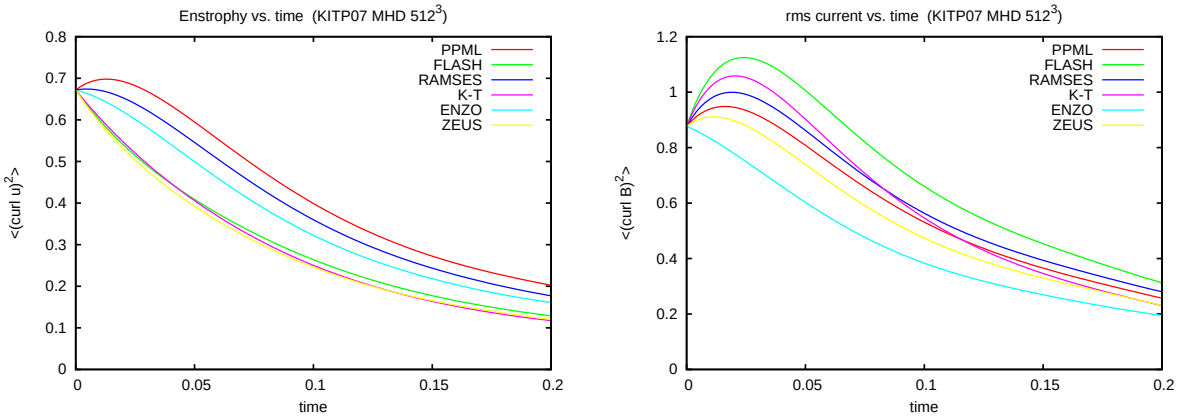

Fig. 4.13: Enstrophy and RMS current $\nabla \times \mathbf{b}$ *vs.* time (Courtesy of A. Kritsuk, yet unpublished KITP07 star-formation benchmarking results).

of the magnetic field $\nabla \times b$ (or RMS current) are shown in Figure 4.13. The ensemble average of the enstrophy decays from 0.66 to $0.1 - 0.2$ at the final snapshot. While for most of the codes the decay begins immediately, the PPML code produces an initial increase in enstrophy. The KT-code evolves the enstrophy comparably to the ZEUS and FLASH codes. In the RMS current evolution on the right hand side of Figure 4.13, most codes initially increase the RMS current. The KT results show an initial increase of this quantity, possibly due to initial conversion of small-scale solenoidal velocity modes to small-scale dilatational velocity modes, caused by the finite-difference scheme.

5. OVERVIEW - RESULTS FROM OBSERVATION AND SIMULATION

Here, a brief overview of the current state of understanding of compressible turbulence that has developed over the past 20 years is provided. In addition to results of numerical simulations, some significant observational discoveries of compressible turbulence in the extraterrestrial world are described. The observational results are mainly based on observation of the interstellar medium. The interstellar medium can be seen as a laboratory for supersonic turbulence over a wide range of spatial scales. The average sonic Mach numbers range from transonic ($\mathcal{M}_\mathrm{s} \approx 1$) in the warm phase of the ISM to highly supersonic ($\mathcal{M}_\mathrm{s} = 5 - 20$) in molecular clouds [3], indicating the compressible nature of interstellar turbulence.
Velocity power-spectra are obtained experimentally by measuring *H 1* emission [17], *H 1* absorption [16], CO emission [4], and Infrared Astronomy Satellite-measured 100μ emission [61]. In 2D maps, the obtained power-spectra were found to have power-law slopes[1] around -2.8 to -3.2. These slopes are obtained from 2D data, where the expected Kolmogorov power-law slope for the velocity-power spectrum in 2D spectra is $-8/3$ or -2.666. One of the major sources of systematic error is the dependence of the obtained scaling-exponents on the velocity-channel width, which is dependent on the resolution [22]. 1D power-spectra, obtained on azimuthal profiles of *H 1* emission in galaxies, have been reported to show slopes in the range of $-5/3$ on large scales to $-8/3$ on small scales ([21], [20]). The transition in the scaling exponent is explained by the transition from 3D to 2D geometry according to the line-of-sight thickness of the *H 1* layer.
More recent results indicate a steeper spectral-scaling of velocity power-spectra in the interstellar medium. Chepurnov *et al.* [12] report a 3D-velocity spectral-index of -3.87 ± 0.11, based on the analysis of *H 1* emission in the Milky Way. The injection scale is reported to be at approximately 180pc, and the steeper velocity power-spectrum is related to shock-domination in the turbulence.
In the measurement of structure function scaling, the $\Delta v - R$ has been established [3]. The $\Delta v - R$ measurements are a good approximation to 2nd order structure functions (see equation (2.45)). Recent surveys of giant molecular clouds (GMC), a constituent of the ISM, have resulted in structure function scaling exponents of $0.5 - 0.65$ [30], and thus larger than the spectral index predicted by the Kolmogorov structure-function exponent of $1/3$. However, higher-order scaling exponents of structure functions are difficult to obtain from observational data.
The deviation of the obtained structure-function scaling-exponents is often explained by the intermittent nature of turbulence, which is closely related to the fractal dimension of the most singular dissipative structures [19]. In incompressible Navier-Stokes turbulence, the most dissipative structures are filaments. The according fractal dimension of the most dissipative structures is thus $D = 1$ (D denotes the fractal dimension). In incompressible MHD, the most dissipative structures were found to be current sheets, and thus $D = 2$ [49]. For supersonic turbulence, regardless of whether hydrodynamic or MHD, shocks are assumed to be the most singular dissipative structures. Since shock fronts are structured like planes, the dimension of those most dissipative structures is associated with $D = 2$ [7], [54], like in the incompressible MHD case.
Direct numerical simulations of ideal, compressible hydrodynamic and MHD turbulence have been carried out with increasingly larger spatial-resolutions since Passot in 1988 [58]. Numerical simulation allows for capturing the full dynamics of compressible turbulence over multiple dynamical times. A limitation of simulations is the unknown influence of the unresolved scales. At resolutions of 512^3, Reynolds numbers of up to $\mathrm{Re} \approx 6000$ are achieved [13], while the according Reynolds number of interstellar turbulence in the cool part of the ISM is of the order of $\mathrm{Re} \approx 10^5 - 10^7$ [22]. In the chaotic star-forming clouds, the Reynolds number exceeds 10^8 and the magnetic Reynolds number is $\mathrm{Rm} > 10^{16}$. Thus, the results of direct numerical simulations cannot realistically be interpreted as describing interstellar turbulence directly. The unresolved scales in simulations may dramatically change the physical picture. This fact renders the finding of universal scaling properties all the more critical, that means scaling properties that are not affected by the resolution and thus the Reynolds number of the numerical simulations.

[1] By convention, power-law slopes denote the spectral scaling exponent including the minus sign. When spectral scaling exponents are described, the β in $E(k) \sim k^{-\beta}$ is stated without the minus sign.

In numerical simulations of ideal and isothermal hydrodynamics in the transonic regime, self-similar scaling of velocity power-spectra was found to agree with the Kolmogorov prediction, and $\beta = 5/3$ [59]. However, in numerical simulations of compressible hydrodynamics in the supersonic regime, power-law scaling of velocity power-spectra was found to be steeper than the Kolmogorov scaling prediction. For high-resolution simulations (1024^3) of solenoidally driven compressible and isothermal turbulence, Kritsuk *et al.* report a scaling-exponent of the power-spectrum of velocity fluctuations of $\beta = 1.95 \pm 0.02$, at $\mathcal{M}_\mathrm{s} = 6$ [36]. This high-resolution simulation suggests a Kolmogorov-like scaling of the density-weighted velocity ($\rho^{1/3}\mathbf{v}$). The according power-spectrum is reported to scale as $\beta = 1.69 \pm 0.02$, and the low-order structure functions of the density-weighted velocity increments scale as predicted by the Kolmogorov phemonenology.

Magnetic fields have been included in numerical studies of compressible MHD turbulence since 1999. Some numerical experiments yield a scaling exponent of the velocity power-spectrum that is independent of the sonic Mach number. Boldyrev reports $\beta \approx 1.74$, at $\mathcal{M}_\mathrm{s} = 10$ and $\mathcal{M}_\mathrm{A} = 3$, in line with Boldyrev's model for compressible MHD turbulence ([8], [7]). Kowal and Lazarian report an influence of the sonic Mach number on steepening velocity power-spectra in compressible MHD, based on results of 512^3-simulations. In sub-Alfvénic MHD turbulence, they obtain a scaling exponent of $\beta = 1.70 \pm 0.05$ at $\mathcal{M}_\mathrm{A} = 0.7$ and $\mathcal{M}_\mathrm{s} = 0.7$. At $\mathcal{M}_\mathrm{A} = 0.7$ and $\mathcal{M}_\mathrm{s} = 7$, they obtain $\beta = 2.14 \pm 0.05$ [34]. In addition, they report a Kolmogorov-like scaling of the density-weighted velocity power-spectrum, independent from the sonic Mach number.

In a recent comparison of velocity-power spectra among three different codes, Padoan *et al.* [57] report scaling exponents between $\beta = 1.9$ (Stagger code) and $\beta = 2.2$ (Zeus code) for a supersonic and super-Alfvénic MHD turbulence at $\mathcal{M}_\mathrm{s} = 10$. The obtained scaling-exponents appear to differ strongly, dependent on the numerical method that was used to simulate isothermal MHD turbulence. The lower-order finite-difference code, the Zeus code, yields steeper velocity power-spectra than the higher order Stagger code.

Kritsuk *et al.* report on the influence of the Alfvén Mach number on the scaling exponent of velocity power-spectra, based on supersonic ($\mathcal{M}_\mathrm{s} = 10$) 512^3-simulations with a PPML-solver [37]. In the strongly super-Alfvénic regime of $\mathcal{M}_\mathrm{A} \approx 10$, the scaling exponent agrees with the non-magnetic case, and $\beta \approx 1.94$. In the mildly super-Alfvénic regime around $\mathcal{M}_\mathrm{A} \approx 3$, a scaling exponents of $\beta \approx 1.62$ is reported. At $\mathcal{M}_\mathrm{A} \approx 1$, they report $\beta \approx 1.51$. The increase of the relative strength of the magnetic-field fluctuations is reported to lead to a flattening of the velocity power-spectra.

Several numerical studies on the width σ of the mass-density PDFs (see equation (2.76)) have been published over the last decade. Both solenoidally and dilatationally driven turbulence have been investigated. In isothermal hydrodynamic turbulence, Federrath *et al.* report a strong dependence of the model parameter b on the forcing type [24]. They obtain $b = 0.36 \pm 0.03$ in solenoidally driven $\mathcal{M}_\mathrm{s} \approx 5.3$ turbulence and $b = 1.05 \pm 0.19$ in compressibly driven $\mathcal{M}_\mathrm{s} \approx 5.6$ turbulence. The applied forcing method strongly influences the observed width of the density PDF. In solenoidally driven MHD turbulence, the obtained Mach-number dependency parameter ranges from $b \approx 0.5$ [55] and $b = 0.38 - 0.41$ in the super-Afvénic regime [43], to $b \approx 0.5$ in the sub-Alfvénic regime [42]. A systematic influence of the Alfvén Mach number on the width of the density PDFs within a single numerical study has not yet been reported.

A systematic study of the influence of the sonic Mach number on the scaling of velocity structure-functions has been carried out by Padoan *et al.* [54]. In numerical studies of super-Alfvénic MHD turbulence, the sonic Mach number has been varied from subsonic ($\mathcal{M}_\mathrm{s} = 0.3$) to highly supersonic ($\mathcal{M}_\mathrm{s} = 10$). They show that the dimension of most dissipative structures grows continuously from $D \approx 1$ in the subsonic regime to $D \approx 2$ in the highly-supersonic regime.

It is difficult to draw a clear conclusion, based on the reported results. Most of the numerical studies concentrate on a limited area of sonic and Alfvén Mach number space. Thus, a comparison of the reported scaling-exponents and density-PDFs is impossible. A further source of complication stems from the fact that not only does the resolution affect the reported turbulence properties, but also the numerical method of the used solvers. In this work, a systematic approach is used to test the influence of the sonic-Mach number and the Alfvén Mach number on the low-order statistical properties of hydrodynamic and MHD turbulence. The next Chapter presents this approach and the results concerning turbulence properties, subject to the parameters $\mathcal{M}_\mathrm{s}$ and $\mathcal{M}_\mathrm{A}$.

6. RESULTS

In this Chapter, the results of numerical simulations of supersonic isothermal turbulence are presented. First, the scaling properties of supersonic hydrodynamic turbulence are described. Special emphasis is put on the dependency of spectral scaling of power-spectra and the shape of mass-density PDFs on the degree of compression, determined by the RMS sonic Mach number $\mathcal{M}_\mathrm{s}$. The numerical experiments test the validity of compressible cascade models such as the Fleck model. This work also presents numerical evidence gathered from the KT code results for a momentum-led cascade. The implications of a momentum-led cascade include a self-similar scaling of power-spectra within supersonic hydrodynamic turbulence.
The second part of the Chapter describes numerical results of self-similar scaling of power-spectra in supersonic and super-Alfvénic MHD turbulence. Here, the influence of the sonic Mach number $\mathcal{M}_\mathrm{s}$ and the Alfvénic Mach number $\mathcal{M}_\mathrm{A}$ on the statistical properties are investigated. This part of the work includes results from high-resolution (1024^3) simulations of compressible MHD turbulence. Finally, numerical evidence for universal scaling of flow quantities such as total energy within highly compressible MHD turbulence is presented.

6.1 Compressible isothermal hydrodynamic turbulence

Compressible effects become important for turbulence in supersonic flows. In the subsonic regime, the flow can be described well by incompressible Navier-Stokes turbulence (see [5], page 183). Low-order statistical scaling properties are in-line with the according Kolmogorov turbulence-model. The numerical experiments of this work cover the range between the mildly-supersonic (or transonic) regime and the highly-supersonic regime. The amplitude of the Ornstein-Uhlenbeck forcing in equation (3.29) determines the RMS sonic Mach number. The Fleck model is tested by varying the forcing amplitude in steps that cover a Mach number range of $\mathcal{M}_\mathrm{s} \approx 1$ to $\mathcal{M}_\mathrm{s} \approx 5.5$. At each Mach number step, the flow evolves for multiple dynamical times to obtain statistically steady-state information, capturing several hundred spectral snapshots per Mach number. In compressible turbulence, it is customary to define the dynamical time as the flow-crossing time. The flow-crossing time reflects the average flow-velocity and is defined as $t_\mathrm{d} = L/\mathcal{M}_\mathrm{s}$, with L being the dimensionless side-length of the computational domain [36].
The Mach-number scan covers approximately 25 flow-crossing times at a spatial resolution of 512^3. A total number of 2500 spectral snapshots are obtained. In order to assess the influence of resolution (and thus the Reynolds number of the flow), the results from several dynamical times of a 1024^3 run at a fixed Mach number are provided and investigated in detail. Both 512^3 and 1024^3 runs are forced solenoidally at large scales ($2 \leq k \leq 3$). The parameters of the runs are outlined in Table 6.1. Figure 6.1 shows a

run	hydro 512^3	hydro 1024^3
dynamical times	25	3
sonic Mach number $\mathcal{M}_\mathrm{s}$	1-5.5	2.8
# of snapshots	2500	500
# of processes	256	512
Forcing	solenoidal	solenoidal
Forcing range	$2 \leq k \leq 3$	$2 \leq k \leq 3$

Tab. 6.1: Overview of the parameters in hydrodynamic turbulence simulation runs.

cut through the density-field and the absolute value of the velocity-field of a Mach 3 turbulence at 1024^3 resolution. The density-field on the LHS is highly compressed, showing large dilute regions where the mass-density is considerably smaller than 10^{-1}. The bright yellow regions show the compressed high-density regions, where the density reaches values higher than 10^2. On the RHS of Figure 6.1, the absolute

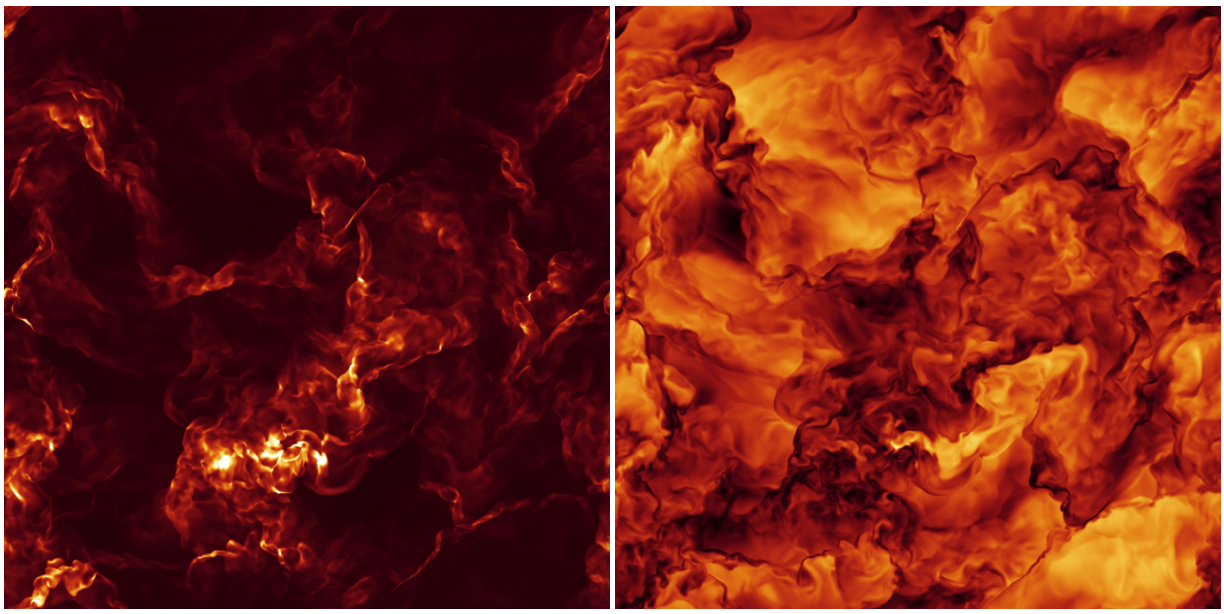

Fig. 6.1: Cuts through the density field on left side and the velocity-field intensity on the right side in fully developed hydrodynamic turbulence at Mach 3. The black color indicates small values of the density and the velocity-field intensity, yellow colors indicate large values. Strong compression is observed where the velocity-field intensity is almost zero due to compression flows at the edges of counter-rotating eddies.

value of the velocity is shown for the same plane. Regions with low absolute velocity-values are regions between counter-rotating eddies. These regions roughly correspond to the high-density regions on the LHS of Figure 6.1.

6.1.1 Diagnostics

The ensemble averages of power spectra of the form $\langle u^2 \rangle$ are measured by replacing the ensemble average $\langle . \rangle$ by a time average. Replacing the ensemble average by the time average is possible when the flow is statistically-stationary over time scales larger than the time scales of the fluctuations (see *e.g.* [10]). The argument of equality of time and ensemble averages follows from the quasi-ergodicity hypothesis, often used in turbulence studies. However, this hypothesis has not been proved formally for the Navier-Stokes and MHD equations [28].
The time averages for statistically-stationary turbulence are obtained by averaging over a number of spectral snapshots. For example, the time-averaged power spectrum of velocity fluctuations for a fixed sonic Mach number is obtained as

$$v_k^2|_{\mathcal{M}_s=\text{const}} = \frac{1}{N} \sum_{\mathcal{M}_s \approx \text{const}} v_k^2(t). \tag{6.1}$$

Here, $v_k^2(t)$ is the t-th time-snapshot of the 1D, k-shell integrated and squared Fourier velocity field. N is the number of time snapshots, for which the sonic Mach number is approximately constant. The time snapshots are computed at fixed time intervals in units of the sound speed. For the 512^3 run, this interval is 0.005 in units of the sound speed. The power spectra are computed at run time. Thereby, the simulation runs provide for a large number of power-spectra in time without producing large amounts of data. 1D power spectra are computed for the following flow quantities:

- Velocity fluctuations $|v|^2(k)$
- Solenoidal (or rotational) part of the velocity $|v_\perp|^2(k)$
- Dilatational (or compressional) part of the velocity $|v_{||}|^2(k)$
- Kinetic-energy fluctuations $\frac{1}{2}|\rho^{1/2}v|^2(k)$
- Density-weighted velocity fluctuations $\frac{1}{2}|\rho^{1/3}v|^2(k)$

- Momentum fluctuations $|\rho v|^2(k)$
- Mass-density fluctuations $|\rho|^2(k)$

After each time interval, a Fast-Fourier-Transform is used to compute the Fourier components from the according real space fields [14].
In addition to the power spectra, mass-density PDFs are computed at the same time intervals. The probability density function of the mass density ρ to occur is measured as

$$f(\rho) = \frac{1}{N} \sum_{i=1}^{n_x n_y n_z} W(\rho - \rho_i), \qquad \text{with } W(\rho - \rho_i) = \begin{cases} 1 & \text{if } |\rho - \rho_i| < \Delta\rho \\ 0 & \text{else} \end{cases} . \tag{6.2}$$

Here, N is the number of grid cells in the domain and ρ_i is the mass-density value of the i-th grid cell. The size of the density bin is chosen as $\Delta\rho = (\rho_{\max} - \rho_{\min})/1000$. In addition to the density PDFs and the power spectra, domain-averages of the kinetic energy and the sonic Mach number are computed at each snapshot.

6.1.2 Time evolution of the sonic Mach number

The flow is initialized with a constant mass-density $\rho_0 = 1$ and zero flow velocity. The constant sound speed is set to 1. The solenoidal force at large scales injects energy and the flow becomes turbulent and statistically stationary after approximately 2 dynamical times. Figure 6.2 shows the time evolution of the RMS sonic Mach number $\mathcal{M}_s$ and the RMS kinetic-energy. The transition to turbulence is not taken into consideration, the spectral snapshots are taken only after the flow has evolved into fully developed turbulence. The simulation ends after 25 dynamical times with $\mathcal{M}_s \approx 5$.
The sonic Mach number evolves from just above unity at $t/t_d = 4$ to 5.5 at $t/t_d = 23$. The kinetic energy covers values of 0.5 to 11 in the same time interval. Both $\mathcal{M}_s$ and E_{kin} display considerable fluctuations in time. This behavior is seen in other high resolution simulations of compressible hydrodynamic turbulence (see e.g. [62] and [36]). It can be explained by the sudden change in the kinetic energy dissipation caused by isothermal shocks. The effect of strong fluctuations is less pronounced in the mildly-supersonic regime $1 \leq \mathcal{M}_s \leq 2$, where the flow is still more smooth and dominated by eddies. For higher Mach numbers, the fluctuations in time become more pronounced as shocks become more prominent.

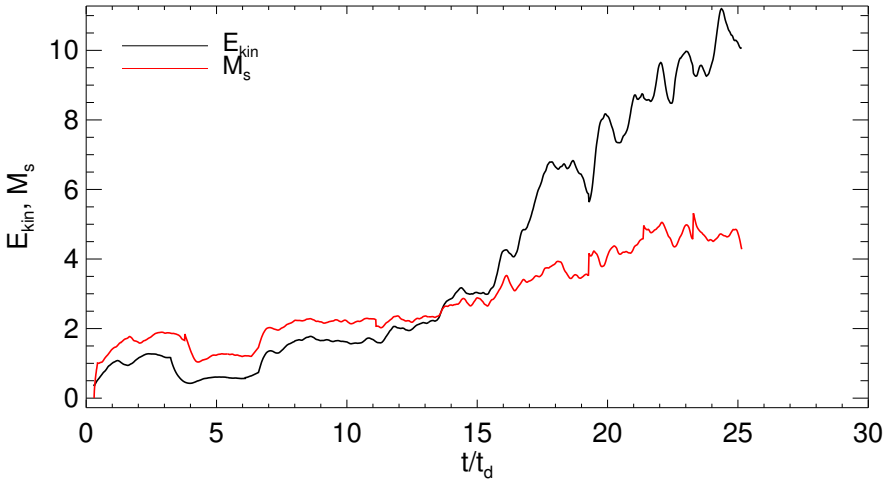

Fig. 6.2: Time evolution of kinetic energy and RMS Mach number in the 512^3 simulation run. After t/t_d=2, the flow is fully turbulent. The run covers sonic Mach numbers between 1 and 5.

6.1.3 Spectral scaling

Power spectra of the various flow quantities are averaged within bins of approximately constant $\mathcal{M}_s$. For each Mach number bin, the time-averaged power-spectra display a power-law scaling-range for wave-

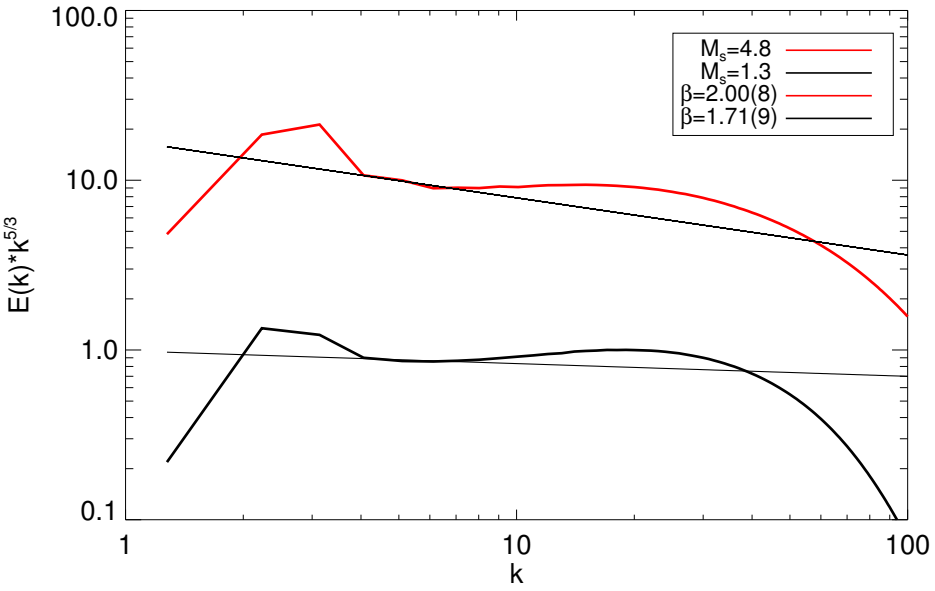

Fig. 6.3: Power spectra of the velocity fluctuations for the transonic and supersonic regime. The spectra are compensated by $k^{5/3}$ and taken from the 512^3-run. The spectra show a power-law scaling for wave-numbers $4 \leq k \leq 7$. The straight lines represent the best-fit to the scaling range. Larger scales are dominated by the energy injection of the forcing. Smaller scales are affected by the bottleneck phenomenon. For k larger than 20, numerical dissipation dominates and the spectra fall off steeply.

numbers greater than the forcing wave-numbers and smaller than the wave numbers affected by the bottleneck in the near dissipation range. In the 512^3 simulations, this range is limited to four wave numbers. In this range of four wave-numbers ($4 \leq k \leq 7$) the power spectra show power-law scaling. A fit to the scaling range of the power spectra is used to extract the scaling-exponent β from the results of the numerical simulations. The power spectra are predicted to scale as

$$E(k) \sim k^{-\beta}. \tag{6.3}$$

Here, $E(k)$ is used as the general term of a 1D power spectrum of a flow quantity. The statistical errors of measured scaling exponents β are computed as a combination of the goodness of the power-law fit and the RMS deviation of scaling-exponents of the individual snapshot spectra to the mean scaling of the time-averaged spectra. The statistical uncertainty of the sonic Mach number is computed as the RMS deviation from the average sonic Mach number within the Mach number bin. Both statistical errors are given in brackets. The digits that are given in brackets stand for the statistical error of the last digits of the stated results (*e.g.* $\beta = 1.71(9)$ stands for $\beta = 1.71 \pm 0.09$).
The power spectrum of the velocity fluctuations in the transonic regime of $\mathcal{M}_\mathrm{s} = 1.3(2)$ is measured to scale as $\beta = 1.71(9)$ (see Figure 6.3). The scaling-exponent agrees with the Kolmogorov scaling exponent of 5/3 within statistical errors. The Kolmogorov-like scaling is applicable to the subsonic regime of eddy-dominated turbulence. The scaling within the transonic regime thus appears to be mainly eddy-dominated, as well. In the highly-supersonic regime of $\mathcal{M}_\mathrm{s} = 4.8(2)$, the scaling-exponent is measured as $\beta = 2.00(8)$ and is significantly larger than the scaling exponent in the transonic regime. The measured steepening of the velocity power-spectrum in the scaling-range agrees with the prediction of the Fleck model (see equation (2.72)) as well as with results of other numerical simulations of compressible hydrodynamic turbulence [36].

The obtained kinetic-energy spectra show a power-law scaling-behavior in the same range of wave-numbers. Figure 6.4 illustrates the time-averaged power-spectra of $\rho^{1/2}v$ at the same flow-velocity regimes of $\mathcal{M}_\mathrm{s} = 1.3(2)$ and $\mathcal{M}_\mathrm{s} = 4.8(2)$. The according scaling exponent for the transonic regime is measured as $\beta = 1.64(7)$. This scaling exponent agrees within statistical error with the Kolmogorov scaling exponent and with the exponent of the velocity power-spectrum. The resulting scaling indicates as expected, that the density fluctuations do not contribute significantly to the kinetic-energy spectrum in the transonic regime. At $\mathcal{M}_\mathrm{s} = 4.8$, the scaling-exponent is measured to be $\beta = 1.54(7)$, significantly smaller than in

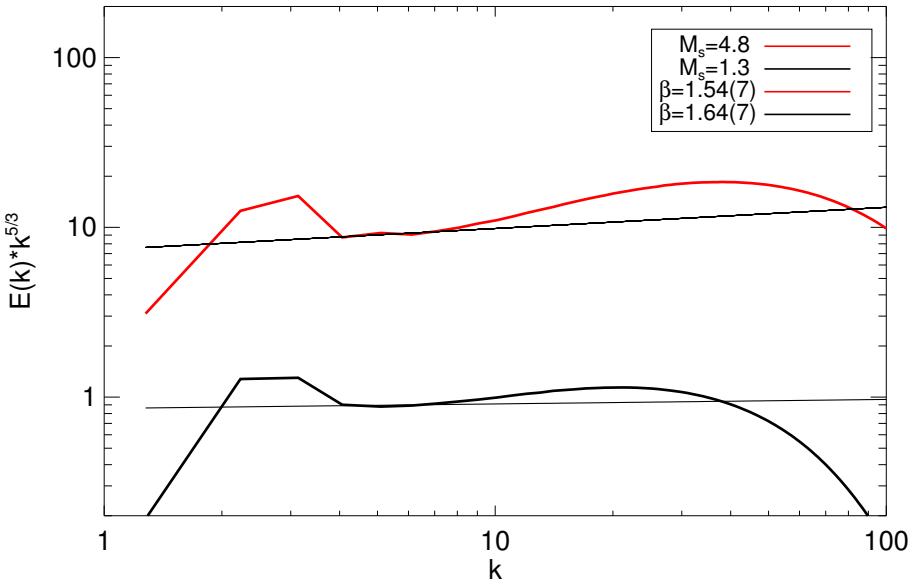

Fig. 6.4: Compensated kinetic-energy spectra for the transonic and supersonic regime. Power-law scaling is obtained for wave-numbers $4 \leq k \leq 7$. The spectral scaling exponents are measured as $\beta = 1.64(7)$ and $\beta = 1.54(7)$.

the transonic regime. An increase in the sonic Mach number leads to a flattening of the kinetic-energy spectrum in the self-similar scaling-range. This result also corresponds to the prediction of the Fleck model. The obtained scaling exponent also agrees with $\beta = 1.52(1)$, obtained in a Mach 6 high-resolution simulation by Kritsuk *et al.* in [36].

The power spectra of the density-weighted velocity $\rho^{1/3}v$, predicted to scale with a Kolmogorov-scaling exponents of 5/3 [36], are shown in Figure 6.5. The range of wave numbers with power-law behavior of the spectra is the same as for the velocity power-spectra and the kinetic-energy spectra. The scaling exponents obtained are $\beta = 1.70(6)$ and $\beta = 1.72(7)$. Both exponents correspond to Kolmogorov-scaling within error bars. The limited resolution and statistics prevent the measurement of a significant deviance from a Mach-number independent scaling, described by equation 2.73. Any influence of $\mathcal{M}_\mathrm{s}$ on the scaling-exponent of the density-weighted velocity, if such a dependence exists, cannot be resolved by 512^3 simulations and the obtained statistics.

Within the range of sonic Mach numbers between one and five, the spectral-scaling exponents of the velocity fluctuations change from 5/3 to 2. The functional dependence of the scaling exponent on $\mathcal{M}_\mathrm{s}$ can be shown by plotting the measured exponent of the fit to individual spectral snapshots *vs.* the sonic Mach number at the snapshot. Figure 6.6 shows this functional relation. The error bars represent the RMS fluctuations of the fit-exponents and the Mach number. At $\mathcal{M}_\mathrm{s}$ just above one, a mean scaling exponent of 1.69(17) is obtained. The value of the measured scaling exponent increases quickly in the transonic range until it saturates at $\mathcal{M}_\mathrm{s} = 3$ with an average scaling exponent of 1.99(12). From $\mathcal{M}_\mathrm{s} = 3$ to $\mathcal{M}_\mathrm{s} = 5$, the average scaling of the velocity power-spectrum does not increase significantly within statistical error. This functional behavior might reflect, that the transition of an eddy-dominated turbulence to a shock-dominated turbulence occurs within the mildly-supersonic regime.

The scaling-exponents of the velocity power-spectra and the kinetic-energy spectra, obtained from the 512^3-run, allow for a calculation of the degree of compression α, as proposed in the Fleck model equations (2.72)-(2.74). The degree of compression can be expressed by the velocity power-spectrum and the kinetic-energy spectrum in the self-similar range (see equations (2.72) and (2.74)) as

$$\frac{|\rho^{1/2}v|_k^2}{|v|_k^2} \sim k^{3\alpha}. \tag{6.4}$$

This scaling relation, evaluated at $\mathcal{M}_\mathrm{s} = 1.3$, reveals a scaling of the fraction of equation (6.4) of $\sim k^{0.07}$. Thus, $3\alpha = 0.07$ or $\alpha = 0.023$. At $\mathcal{M}_\mathrm{s} = 4.8$, the fraction in (6.4) scales as $k^{0.46}$, and thus $\alpha = 0.153$.

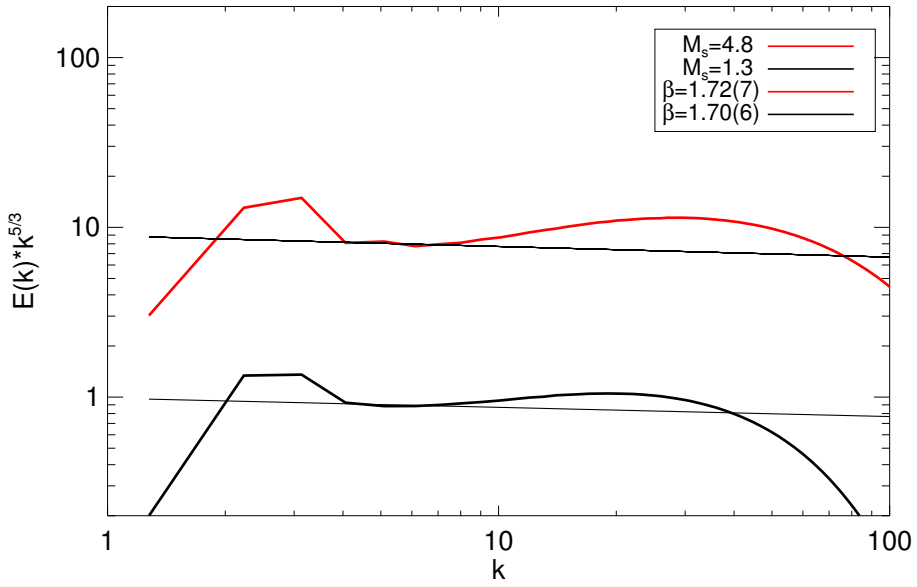

Fig. 6.5: Compensated power-spectra of the density-weighted velocity $\rho^{1/3}v$ for the transonic and supersonic regime. Power-law scaling is obtained for wave-numbers $4 \leq k \leq 7$. The spectral scaling exponents are measured as $\beta = 1.70(6)$ and $\beta = 1.72(7)$.

When the scaling of the density-weighted velocity is assumed to be independent of α, the degree of compression should also be reflected in the fraction of the power spectra of the density-weighted velocity and the velocity fluctuations (see equations (2.72) and (2.73)):

$$\frac{|\rho^{1/3}v|_k^2}{|v|_k^2} \sim k^{2\alpha}. \tag{6.5}$$

Furthermore, the degree of compression can be derived from the ratio of the power spectra of the kinetic energy to the density-weighted velocity, which is predicted to scale as (see equations (2.74) and (2.73))

$$\frac{|\rho^{1/2}v|_k^2}{|\rho^{1/3}v|_k^2} \sim k^{\alpha}. \tag{6.6}$$

These fractions can be evaluated at each sonic Mach-number bin. The comparison of the functional behavior of the obtained α, 2α, and 3α, respectively, allows for a consistency check of the Fleck model of compressible turbulence. In Table 6.2, the calculated values for α, 2α, and 3α are shown for five consecutive Mach numbers. In addition, the ratio of the calculated 2α over α is presented.

The calculation of the degree of compression reveals a fundamental flaw in the combined Fleck-model

$\mathcal{M}_s$	3α	2α	α	$2\alpha/\alpha$
1.2	0.078(62)	0.04(4)	0.038(21)	1.085
1.5	0.18(6)	0.10(4)	0.085(22)	1.204
1.8	0.22(6)	0.12(4)	0.10(2)	1.198
2.3	0.33(10)	0.19(7)	0.14(3)	1.293
3.6	0.47(13)	0.27(9)	0.20(4)	1.338
4.6	0.47(11)	0.27(8)	0.20(4)	1.363

Tab. 6.2: Degree of compression, calculated from the ratio of kinetic-energy spectra and velocity power-spectra (3α), the ratio of density-weighted velocity power-spectra and velocity power-spectra (2α), and the ratio of kinetic-energy spectra and density-weighted velocity power-spectra (α). The results are based on the analysis of the 512^3 simulation run.

and Kolmogorov-like density-weighted velocity predictions. The ratio of the measured $2\alpha/\alpha$ is considerably smaller than the predicted ratio of 2. The obtained ratio is not a constant, but increases from

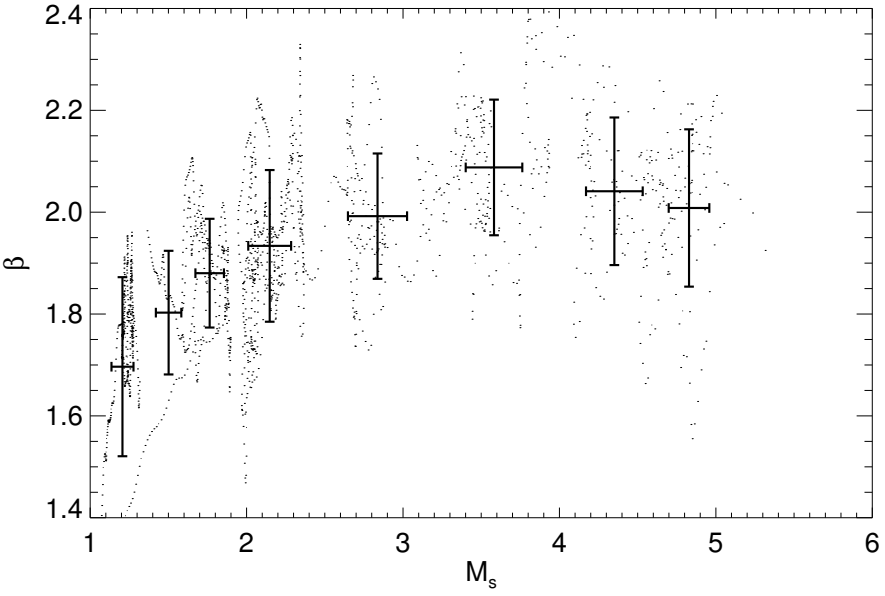

Fig. 6.6: Scaling exponents β of individual snapshots of the velocity power-spectrum *vs.* the average sonic Mach number of the flow. The value of the measured scaling-exponent increases from $\beta \approx 5/3$ at $\mathcal{M}_\mathrm{s} = 1.2$ to $\beta \approx 2$ at $\mathcal{M}_\mathrm{s} = 5$. The increase occurs mainly within the mildly-supersonic regime of $1 < \mathcal{M}_\mathrm{s} < 3$. Error bars represent the RMS deviations of β and $\mathcal{M}_\mathrm{s}$.

approximately 1.1 at $\mathcal{M}_\mathrm{s} = 1.2$ to approximately 1.36 at $\mathcal{M}_\mathrm{s} = 4.6$.
In order to evaluate the limited resolution as a potential source of error, the same analysis is carried out for the 1024^3 results. Here, the 380 spectra of the three dynamical times of a Mach 3 simulation of hydrodynamic turbulence are time-averaged. The according power spectra yield scaling exponents of 1.84(4) for the velocity, 1.54(3) for the kinetic energy, and 1.68(3) for the density-weighted velocity. The scaling-range of the according power spectra is larger than in the 512^3 case and covers wave numbers $4 \leq k \leq 12$. Table 6.3 shows the according degree of compression. The obtained ratio of $2\alpha/\alpha \approx 1.3$, significantly lower than the predicted value of 2. The quantitative analysis of the results of both 512^3 and

$\mathcal{M}_\mathrm{s}$	3α	2α	α	$2\alpha/\alpha$
2.8	0.30(5)	0.17(4)	0.13(2)	1.308

Tab. 6.3: Resulting degree of compression for the 1024^3 data, at a sonic Mach number of $\mathcal{M}_\mathrm{s} = 2.8$.

1024^3 simulations runs do not match the predictions of the Fleck-model scaling-behavior and the according degree of compression. Nevertheless, the qualitative prediction of a steepening velocity-fluctuation power-spectrum with increasing compression is reflected by the results of the KT code simulation runs.

6.1.4 Compressible and solenoidal parts of the velocity-fluctuations

The velocity in supersonic hydrodynamic turbulence, discussed in the previous section, consists of both compression and vortex motions. In order to distinguish between those two components, the velocity vector-field $\mathbf{v}$ is split into a rotational and a compressional part by a Helmholtz decomposition (see *i.e.* [22], page 227).

$$\mathbf{v} = \mathbf{v}_\perp + \mathbf{v}_{||}. \tag{6.7}$$

The rotational part $\mathbf{v}_\perp$ is divergence-free ($\nabla \cdot \mathbf{v}_\perp = 0$), and the compressional part is curl-free ($\nabla \times \mathbf{v}_{||} = 0$). In supersonic turbulence, the two components $\mathbf{v}_\perp$ and $\mathbf{v}_{||}$ lead to physically different effects. While the compressional part $\mathbf{v}_{||}$ leads to shocks, and thus to compression and rarefaction of the gas, the solenoidal

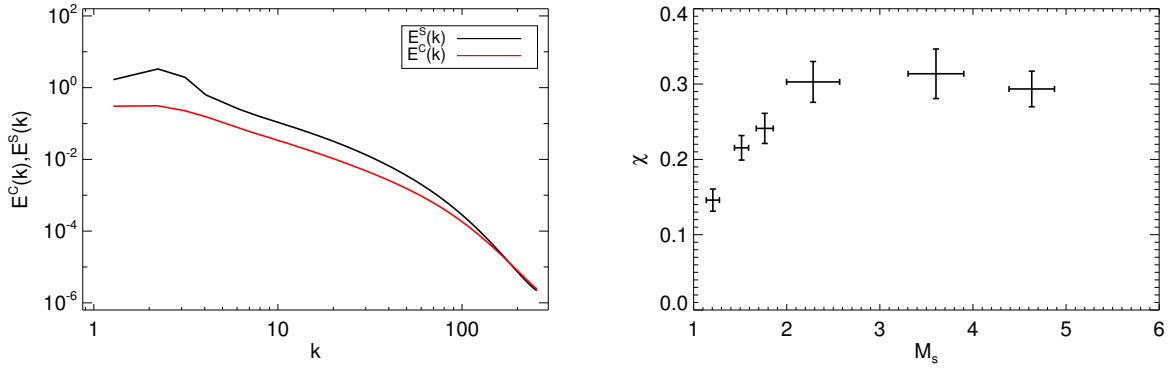

Fig. 6.7: Time-averaged solenoidal velocity power-spectrum and compressible velocity power-spectrum (LHS). The average sonic Mach number is approximately 3. The RHS shows the ratio of $E^{\mathrm{C}}/E^{\mathrm{S}}$ for different average sonic Mach numbers $\mathcal{M}_{\mathrm{s}}$.

component $\mathbf{v}_\perp$ is associated with vortex structures. Power-spectra of the flow-quantities $\mathbf{v}_\perp$ and $\mathbf{v}_{||}$ are the solenoidal velocity power-spectrum and the compressional velocity power-spectrum:

$$E^{\mathrm{S}}(k) = |\mathbf{v}_\perp|_k^2, \qquad E^{\mathrm{C}}(k) = |\mathbf{v}_{||}|_k^2. \tag{6.8}$$

The ratio of compressional squared velocity-fluctuations to rotational squared velocity-fluctuations is referred to as χ-function:

$$\chi(k) = \frac{E^{\mathrm{C}}(k)}{E^{\mathrm{S}}(k)}. \tag{6.9}$$

Integrated over all wave numbers k, this ratio χ is a measure of the relative importance of shock-related motions over vortex motions [5]:

$$\chi = \frac{E^{\mathrm{C}}}{E^{\mathrm{S}}}. \tag{6.10}$$

In compressible hydrodynamic turbulence, the relative importance of shock related motions over vortex motions is likely to depend on the RMS Mach number of the turbulence. In the subsonic and incompressible limit, the flow is mainly solenoidal and $\chi \to 0$. In the transonic regime, compressible motions begin to contribute to the turbulent velocity-fluctuations. Power-spectra of the solenoidal velocity-fluctuations and the compressible velocity-fluctuations, time-averaged onto the sonic Mach number bin $\mathcal{M}_{\mathrm{s}} = 2.8$, are shown on the LHS of Figure 6.7. The amplitude of the compressible velocity-fluctuations is smaller than the amplitude of the solenoidal velocity-fluctuations over all wave numbers k. In the forcing range, the ratio of $E^{\mathrm{C}}/E^{\mathrm{S}}(k)$ is artificially small, as the applied forcing is purely solenoidal. As spectral scales with wave numbers $k = \{2, 3\}$ yield the highest contribution to the total value of the velocity fluctuations, a computation of χ that includes the forcing range would lead to an artificially biased representation of the relative importance of compressible velocity-contributions. Here, the ratio χ is thus computed for scales of wave number $k > 3$.
On the RHS of Figure 6.7, the ratio χ is plotted as a function of the sonic Mach number, based on the data of the 512^3-run. In the transonic regime of $\mathcal{M}_{\mathrm{s}} = 1.2$, the ratio χ is obtained as 0.15(2). At higher sonic Mach numbers, χ increases. For $\mathcal{M}_{\mathrm{s}} > 2$, the ratio χ appears to saturate to a value of 0.30(3). This implies that the relative importance of compressible velocity-fluctuations over incompressible velocity-fluctuations within supersonic turbulence is much smaller than assumed by the model view of a 3D Burgers' turbulence of uncorrelated shocks. Solenoidal modes dominate in solenoidally driven supersonic turbulence.

6.1.5 Mass-density probability distribution

An increase in the sonic Mach number is reflected in the growing compression of the neutral gas. The compression is reflected in the width σ of the log-normal density PDFs. The density contrast, *i.e.* the

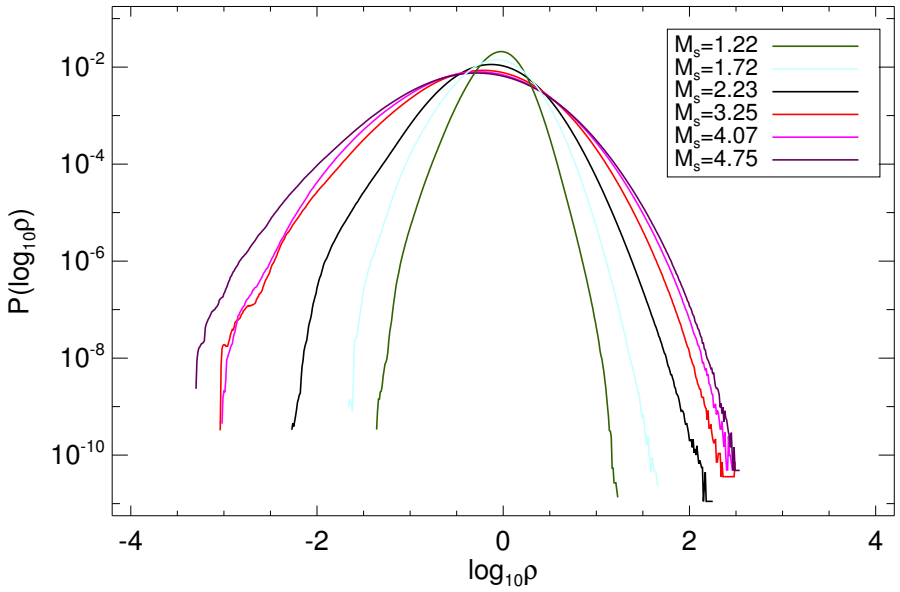

Fig. 6.8: Probability density function for the gas density of the 512^3-run, time-averaged onto six Mach number bins. The distributions follow a log-normal function.

difference of the fluid element with the lowest mass-density to the fluid element with the highest mass-density, spans several orders of magnitude. Figure 6.8 illustrates the mass-density PDFs, time-averaged onto Mach number bins. In the transonic regime, the density contrast is of the order of 10^4. An increase of the average Mach number is reflected by broader probability distributions. At the highest Mach number $\mathcal{M}_\mathrm{s} = 4.75$, the density contrast spans 6 orders of magnitude. Each of the time-averaged PDFs can be fitted by the log-normal distribution function (2.75). The departure of the PDFs from the log-normal distribution in the low-density tail results from strong head-on collisions is the gas. The head-on collisions are followed by strong rarefactions that lead to oscillations in the low-density tail. The most drastic change of the width of the PDFs with $\mathcal{M}_\mathrm{s}$ takes place in the mildly-supersonic regime $1 < \mathcal{M}_\mathrm{s} < 3$. Above $\mathcal{M}_\mathrm{s} = 3$, the increase in the width with the Mach number is less dramatic but still noticable. The broadening corresponds well with the steepening of the velocity power spectrum, where the steepening is also more pronounced in the mildly-supersonic regime.

The standard deviation σ was suggested by Padoan *et al.* [55] to be expressed as a function of the sonic Mach number

$$\sigma_\rho = b\mathcal{M}_\mathrm{s}. \tag{6.11}$$

Equation (6.11) denotes the function of the width of the linear mass-density PDF. For the logarithmic mass density, the width can be expressed as [55]

$$\sigma^2_{\ln\rho} = \ln\left(1 + b^2\mathcal{M}_\mathrm{s}^2\right). \tag{6.12}$$

The obtained width $\sigma_{\ln\rho}$ increases from a value of 0.425(4) at $\mathcal{M}_\mathrm{s} = 1.2$ to 1.209(7) at $\mathcal{M}_\mathrm{s} = 4.8$. The width of the lognormal fit to the logarithmic mass-density PDF can be plotted *vs.* the average sonic Mach number for each snapshot in time. The best-fit to the data (see Figure 6.9), following the model function (6.12) yields a value of $b = 0.416(2)$ for the 512^3 run. The model function reflects the obtained dependence of the PDF-width on the RMS Mach number remarkably well over the range of $\mathcal{M}_\mathrm{s} = 1.2 - 5.2$. The value of b deviates from the value of $b = 0.260(1)$, reported by Kritsuk *et al.* [36]. The results of this work are much closer to the results reported by Padoan *et al.* [55], where they obtain a value of approximately 0.5 for b in compressible MHD turbulence.

The same analysis of the width of mass-density PDFs on the 1024^3 data yields $b = 0.432(2)$, which is slightly bigger than the b obtained on the 512^3 data. Resolution thus seems to have an effect on the density PDFs. Limited resolution keeps the density probability distribution artificially narrow. This effect has been reported by Federrath *et al.* [24] regarding results from simulations with the FLASH3 code.

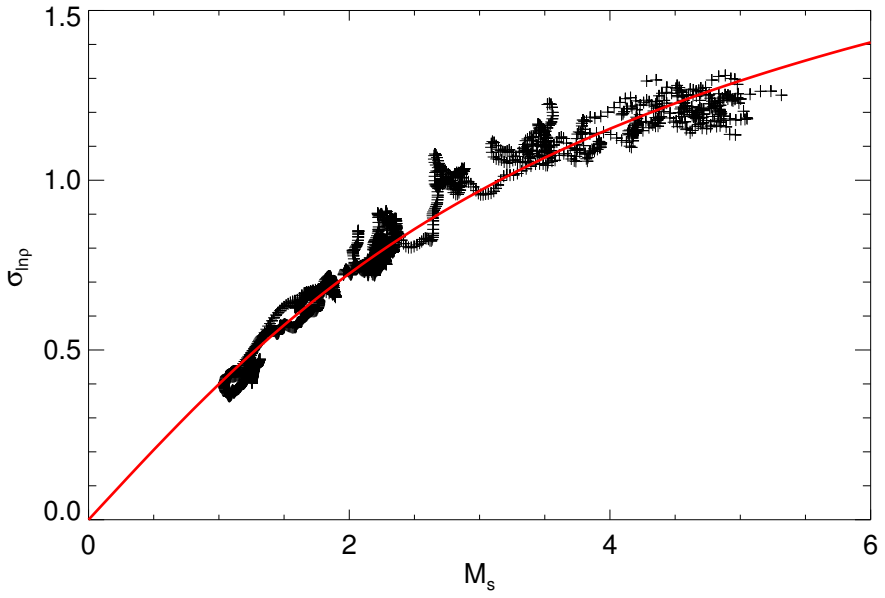

Fig. 6.9: Width σ of the logarithmic density PDF as a function of the RMS sonic Mach number $\mathcal{M}_\mathrm{s}$, based on the 512^3-run. The individual points are the width of the lognormal fit to the 2500 individual PDF snapshots. The red line shows the best-fit of the data to the model function $\sigma^2_{\ln\rho} = \ln(1 + b^2\mathcal{M}_\mathrm{s}^2)$. The fit results in an obtained parameter $b = 0.416(2)$.

For solenoidally forced isothermal hydrodynamic turbulence on a 1024^3 grid, they report a fit-parameter $b = 0.36(3)$, a value that is close to the results presented in this work.

6.1.6 *Scaling of mass-density and momentum power-spectra*

A self-similar scaling of the mass density is an assumption of the Fleck-model of compressible turbulence. The power spectrum of the mass-density fluctuations ρ should also exhibit a scaling range. The power-spectrum of the mass density is given by

$$|\rho|^2 \sim k^{-\beta}. \tag{6.13}$$

Time-averaged density power-spectra, binned to average sonic Mach numbers, are shown in Figure 6.10. The density power-spectra scale with the spectral wave-number in the wave-number range of $4 \leq k \leq 12$. The obtained β depends on $\mathcal{M}_\mathrm{s}$. In the mildly-supersonic regime with an average sonic Mach number just above unity, the scaling exponent is measured as $\beta = 1.20(6)$. With an increasing average flow-velocity, the density power-spectra become flatter. At $\mathcal{M}_\mathrm{s} = 4.8$, the measured scaling-exponent takes a value of $\beta = 0.77(4)$. The spectra at sonic Mach numbers in between these extremes become consecutively flatter. The flattening of density power-spectra indicates that the increase in the average flow-velocity favors compressible modes that couple to density fluctuations. This leads to a higher net energy-transfer from velocity fluctuations to density fluctuations at smaller scales. The self-similarity of density-fluctuations, assumed by von-Weizsäcker's argument of equation (2.65), is numerically reproduced by this work's results. The influence of $\mathcal{M}_\mathrm{s}$ on the value of the scaling exponent of density power-spectra is stronger than for velocity power-spectra, since density becomes a constant in the subsonic limit $\mathcal{M}_\mathrm{s} < 1$. In Table 6.4, the obtained scaling exponents of the mass-density power-spectra are outlined. Like in the case of velocity power-spectra, the rate of change of the obtained scaling-exponents is more pronounced in the mildly-supersonic range of $1 \leq \mathcal{M}_\mathrm{s} \leq 3$. In this regime, the spectra flatten more quickly. In the supersonic regime, the range of $\mathcal{M}_\mathrm{s} > 3$, the flattening saturates, and a self-similar scaling-exponent of 0.77(4) is obtained.
The power spectra of the momentum density ρv also display self-similar scaling. The range of wave numbers where power-law scaling is observed is $4 \leq k \leq 7$, just as for the velocity power-spectra. In the subsonic regime, the momentum power-spectrum is supposed to converge with the power spectrum

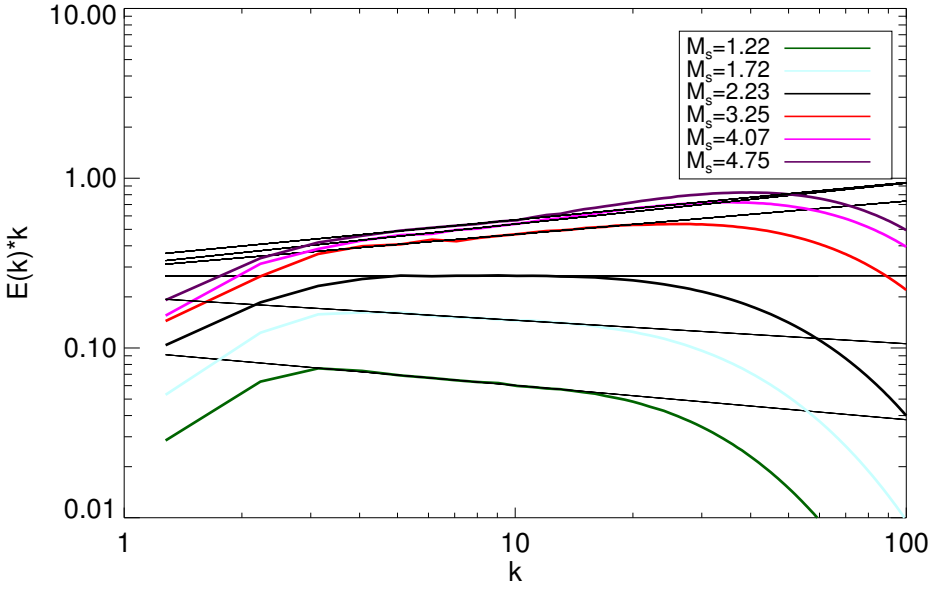

Fig. 6.10: Power spectra of the mass-density at sonic Mach numbers 1-5, based on the 512^3-run, and compensated by k. The spectra follow a power-law for wave numbers $4 \leq k \leq 12$. The scaling-exponents β decrease with an increase of the average sonic Mach number of the flow.

$\mathcal{M}_s$	1.22	1.75	2.23	3.25	4.07	4.75
$\beta_{\lvert\rho\mathbf{v}\rvert_k^2}$	1.45(6)	1.28(6)	1.16(8)	1.05(6)	0.96(8)	1.00(8)
$\beta_{\lvert\rho\rvert_k^2}$	1.20(6)	1.14(4)	1.01(6)	0.82(5)	0.76(5)	0.77(4)

Tab. 6.4: Time-averaged spectral scaling-exponents β of the momentum-density power-spectra and the mass-density power-spectra at six Mach number bins, at 512^3-resolution

of the velocity fluctuations. Both power spectra should agree with the Kolmogorov scaling prediction of $\beta = 5/3$. In the mildly-supersonic regime, the power spectra of the momentum become flatter as the density contribution to the momentum becomes more pronounced. Figure 6.11 shows the time-averaged momentum power-spectra for the six Mach number bins, that where used before for the density power-spectra. The scaling exponent in the transonic regime is measured as $\beta = 1.45(6)$. At $\mathcal{M}_s = 4.75$, the momentum power-spectrum scales with a scaling exponent of $\beta = 1.00(8)$. The decrease of the scaling exponent reflects the growing contribution of the density, which outweighs the increase of the scaling-exponent of the velocity contribution to the momentum.
In addition to the time-averaged spectra of the 512^3 run, the time-averaged momentum power-spectrum of the 1024^3 run is shown in Figure 6.12. The average sonic Mach number is 3, the obtained momentum power-spectrum shows a range of spectral scaling for wave numbers $4 \leq k \leq 12$. The scaling exponent of the 1024^3 momentum power-spectrum is measured as $\beta = 1.17(3)$. The corresponding scaling-exponent of the 512^3 power-spectrum is 1.16(6). These scaling exponents agree within statistical errors. The comparison of scaling exponents of the velocity power-spectra and the kinetic-energy spectra between 512^3 and 1024^3 yields a similar agreement. This shows that the resolution is unlikely to introduce a systematic source of error to this analysis.

6.1.7 Spectral shape of non-linear energy transfer

The partial time-derivative of the Fourier components of vector components of the momentum density $\hat{m}_i$ is described by equation (2.108). For the numerical assessment of the individual terms of this equation, discrete changes in time are computed to approximate the infinitesimal derivatives. The first term in equation (2.108) is the partial time-derivative of the momentum Fourier-components and it is approxi-

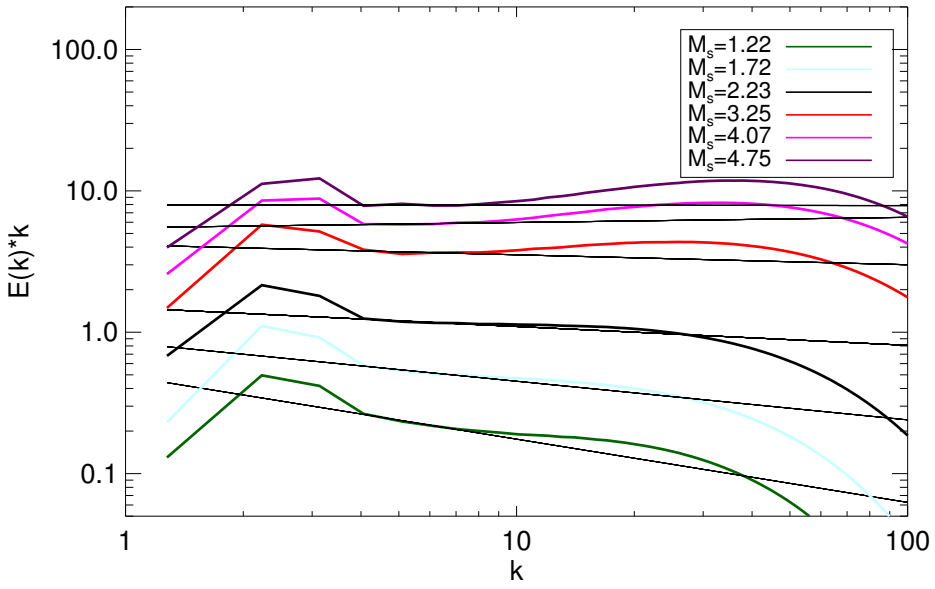

Fig. 6.11: Power spectra of the momentum-density, compensated by k, at sonic Mach numbers 1-5. The data is taken from the 512^3-resolution run. Self-similar scaling is exhibited for wave numbers $4 \leq k \leq 7$. The scaling-exponents β decrease with an increase of the average sonic Mach number of the flow.

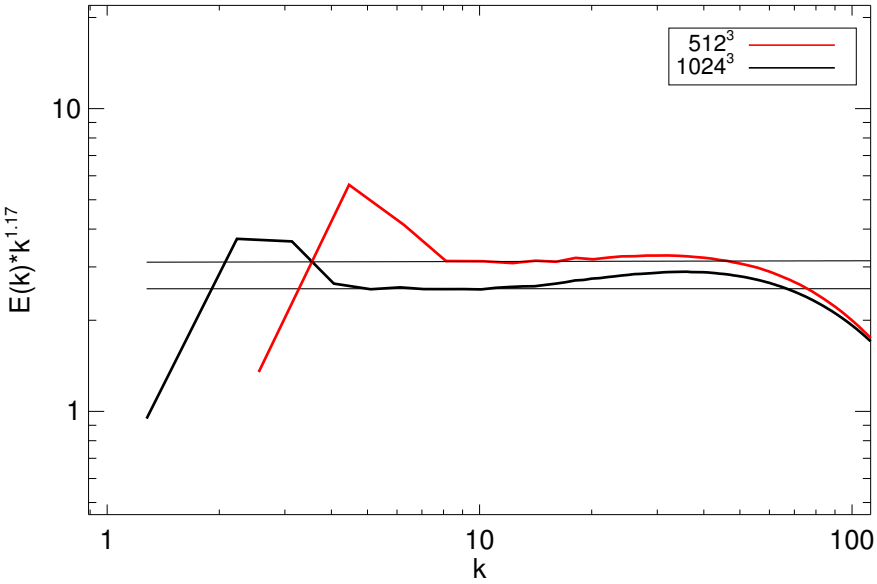

Fig. 6.12: Power spectra of the mass-density at a sonic Mach number of 3, compensated by $k^{1.17}$. Time averaged spectra of 1024^3 and 512^3 are shown to analyze the influence of the resolution. The wave numbers k are normalized to match k/k_{min}. A scaling-range is exhibited for wave numbers $4 \leq k \leq 12$ in the 1024^3 case. The 512^3 spectrum shows a similar scaling for $8 \leq k \leq 12$.

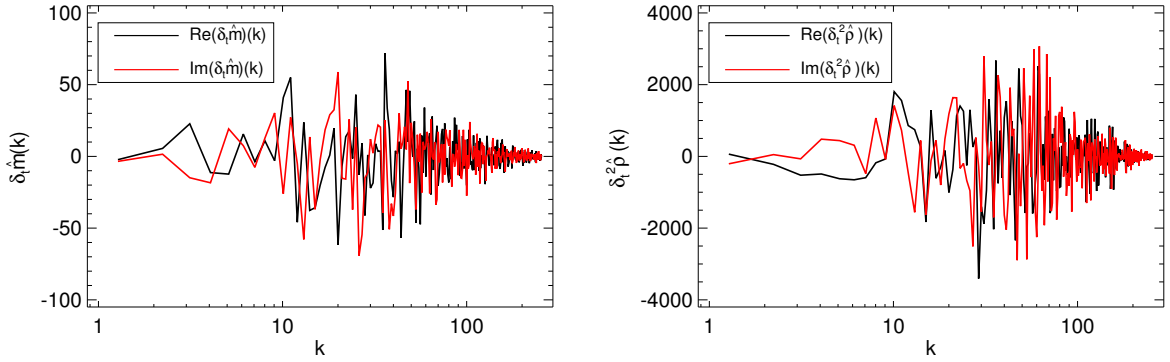

Fig. 6.13: Snapshot of the time-rate of change of the Fourier-components of the momentum-density on the LHS and the mass-density term on the RHS. Both real part and imaginary part oscillate around the time-average value of zero. The amplitude of the oscillation is larger for medium wave-numbers $10 \leq k \leq 40$. In the dissipation range, the amplitude of the oscillation is smaller.

mated by a first-order forward difference in time

$$\frac{\partial}{\partial t}(\hat{m}_i)(|k|) = \frac{\hat{m}_i(|k|)(t+\Delta t) - \hat{m}_i(|k|)(t)}{\Delta t} + O(\Delta t)^2 \tag{6.14}$$

The time step Δt is kept considerably smaller than the time scale on which the momentum-density Fourier-components change in time, in order to capture the turbulent dynamics. Due to spatial isotropy of the turbulence, no statistical differences among Fourier space-directions (k_x, k_y, and k_z) of the vector components are present. Thus the vector components are integrated over all spectral angles within a k-shell, indicated by $|k|$.
The density term in equation (2.108), a projection of the second partial time derivative of the mass-density Fourier-components, is numerically computed as a central difference in time:

$$i\frac{k_i}{k^2}\frac{\partial^2}{\partial t^2}(\hat{\rho}(\mathbf{k})) = \frac{i\frac{k_i}{k^2}\hat{\rho}(\mathbf{k})(t+\Delta t) - 2i\frac{k_i}{k^2}\hat{\rho}(\mathbf{k})(t) + i\frac{k_i}{k^2}\hat{\rho}(\mathbf{k})(t-\Delta t)}{(\Delta t)^2} + O(\Delta t)^2, \text{with} \quad i = \{1,3\} \tag{6.15}$$

The terms in equations (6.15) are computed for all wave-vectors $\mathbf{k}$. After the projection ik_i/k^2 of the individual components $i = \{1,3\}$, the result is integrated over all spectral angles within a wave-number shell $k + \Delta k$:

$$\hat{\rho}_{\partial^2,i}(k) = \sum_{\mathbf{q}} i\frac{q_i}{q^2}\frac{\partial^2}{\partial t^2}\hat{\rho}(\mathbf{q})W(k-q), \qquad \text{with } W(k-q) = \begin{cases} 1 & \text{if } |k-q| < \Delta k \\ 0 & \text{else} \end{cases}. \tag{6.16}$$

The finite time-step Δt in the approximations (6.14) and (6.16) is again kept small compared to the time scale on which the Fourier components change. As a result of equations (6.14) and (6.16), the real part and the imaginary part of three vector components of the Fourier-transformed momentum-density term and the components of the gradient of the mass-density term of equation (2.108) are numerically measured, integrated over k-shells in Fourier-space. Figure 6.13 shows a snapshot of the obtained k-shell integrated time-rate of change of the Fourier-components of the momentum-density term and the mass-density term. Both real part and imaginary part exhibit positive and negative values. The magnitude of momentum change is larger for wave numbers in the range $4 \leq k \leq 60$. Small scale changes (for $k \geq 60$) are dampened due to numerical viscosity. On large scales, that means in the forcing range $k \leq 3$, the obtained changes are smaller than within medium scales. The time-averages of both the imaginary part and the real part of the Fourier components go to zero for all k, since the turbulence is statistically stationary.

Due to isotropy, the time-rate of change of the momentum components statistically does not differ among the vector components in x-, y-, and z-directions. The absolute value of the vectors, $\left|\frac{\partial}{\partial t}(\hat{m})(|k|)\right|$

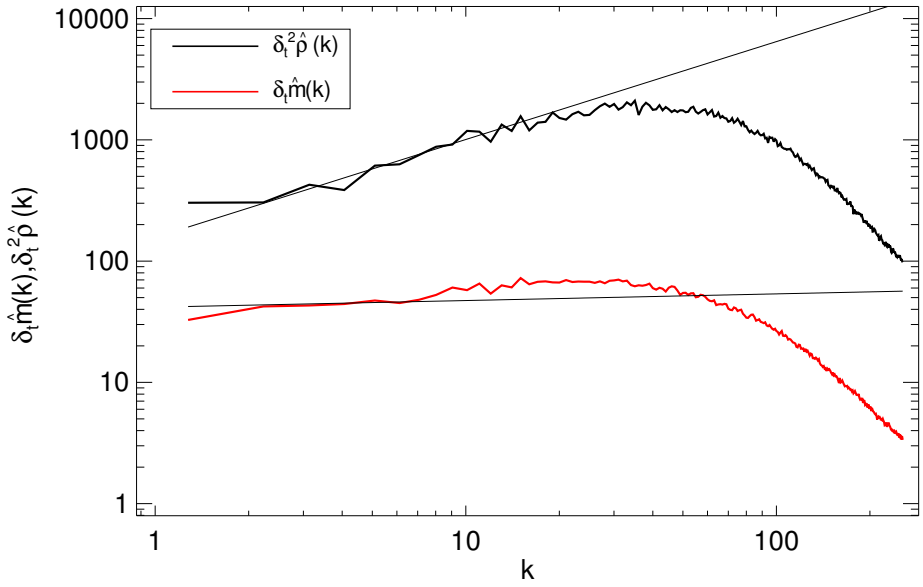

Fig. 6.14: Spectral shape of non-linear transfer to the momentum change and the second time-derivative of the mass density. The transfer terms are time-averaged and component-averaged. The sonic Mach number is approximately 4. The fitted lines are the best-fit to power-law scaling within the wave-number range $4 \leq k \leq 8$.

and $|\hat{\rho}_{\partial^2}(|k|)|$, are computed to be:

$$\left|\frac{\partial}{\partial t}(\hat{m})(|k|)\right| = \left[\sum_{i=1,3}\left|\frac{\partial}{\partial t}(\hat{m}_i)\right|^2\right]^{1/2}, \tag{6.17}$$

$$|\hat{\rho}_{\partial^2}(|k|)| = \left[\sum_{i=1,3}\left|\hat{\rho}_{\partial^2,i}\right|^2\right]^{1/2}. \tag{6.18}$$

The absolute value of the vector of the momentum-density change in Fourier space can now be time-averaged over statistically-stationary turbulent flows to obtain information about the statistical-ensemble behavior of the non-linear energy transfer. Time-averaged data (over 2 dynamical times) for both the momentum-change and the density-change terms are shown in Figure 6.14. The average sonic Mach number $\mathcal{M}_s$ is 4, the data is taken from the 512^3-resolution run. The time-averaged density term shows an increase within the range of obtained power-law scaling of the density power-spectra $4 \leq k \leq 10$. The increase of the density-term follows a power-law, scaling like $k^{0.85(9)}$. Within this range of wave numbers, the momentum-change term exhibits a rather flat spectral shape, followed by a range of higher average values for $k > 10$.

To obtain a total value of non-linear energy transfer to the momentum-fluctuations and the mass-density fluctuations, the time-averaged data is integrated over all k for both momentum and density terms:

$$\left|\frac{\partial}{\partial t}\hat{m}\right| = \sum_k \frac{\partial}{\partial t}(\hat{m}_i)(|k|), \tag{6.19}$$

$$|\hat{\rho}_{\partial^2}| = \sum_k \hat{\rho}_{\partial^2}(|k|). \tag{6.20}$$

A ratio of non-linear energy transfer to the momentum and the mass density is computed. The values for the mass-density term are larger than those for the momentum term on all spectral scales (see Figure 6.14). The ratio of $\partial_t^2\hat{\rho}/\partial_t\hat{m}$ at $\mathcal{M}_s = 4$ is approximately 30. Most of the non-linear energy transfer goes to the density-field fluctuations, compared to non-linear energy transfer to momentum fluctuations.

Because of the resolution limitations to the spectral characteristics of this data, the same statistical

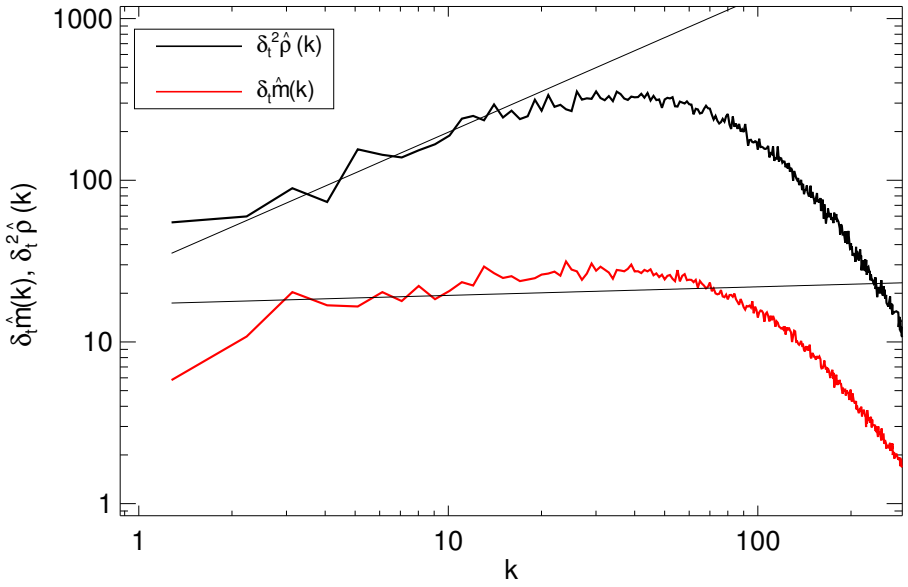

Fig. 6.15: Spectral shape of non-linear transfer to the momentum change and the second time-derivative of the mass-density, based on data from the 1024^3-resolution run. The transfer terms are time-averaged over approximately 0.5 dynamical time, and component-averaged. The sonic Mach number is approximately 3. The straight lines represent the best-fit to power-law scaling for $4 \leq k \leq 12$.

analysis is carried out using data from the 1024^3-run (see Figure 6.15). Similar to the Mach 4 data of the 512^3-run, the Mach 3 data of the 1024^3-run exhibits a flat range of momentum change for $4 \leq k \leq 12$. This implies the conclusion, that the non-linear energy transfer *via* triads of momentum and velocity Fourier components, leads to a self-similar scaling of momentum-density. At higher Mach numbers, the non-linear term of equation (2.108) transfers more and more energy to density fluctuations, while the spectral scaling of this transfer to the density-fluctuations becomes steeper. This can be interpreted as energy being preferentially transfered to density fluctuation at higher wave-numbers k within the range of power-law scaling. The observation of preferential transfer to higher-k density-fluctuations is reflected in the flattening of the density power-spectrum. The spectral shape of the non-linear transfer to the density fluctuations follows a power-law, and so the power-law shape of the density power-spectra is retained while the spectral scaling flattens for higher sonic Mach numbers. In addition, the ratio of $\partial_t^2 \hat{\rho} / \partial_t \hat{m}$ at $\mathcal{M}_\mathrm{s} = 3$ is approximately 10. This ratio is considerably smaller than the according ratio of 30 in the $\mathcal{M}_\mathrm{s} = 4$ analysis. At $\mathcal{M}_\mathrm{s} = 3$, most of the non-linear energy transfer goes to the density-field fluctuations, rather than to momentum-transfer. But the proportion of non-linear energy transfer to the density-fluctuations is smaller at lower RMS sonic Mach numbers. At $\mathcal{M}_\mathrm{s} = 1.5$, time-averaged over approximately 1.5 dynamical times, a ratio of $\partial_t^2 \hat{\rho} / \partial_t \hat{m} \approx 7.5$ is obtained. The higher the mean turbulent flow-velocity is, the more energy is non-linearly transfered to mass-density fluctuations, relative to the energy transfered to momentum-fluctuations.

The results of the non-linear energy-transfer indicate that the role of the non-linear advection term in the momentum equation (2.17) is similar to the role of the non-linear advection term in the incompressible Navier Stokes momentum equation (2.27). The non-linear advection term is responsible for energy distribution among spectral scales. In the incompressible case, the distributed energy goes only into velocity fluctuations. Thereby, in the absence of viscous forces, the self-similarity of the velocity power-spectrum in statistically-stationary Navier-Stokes turbulence is provided for. In compressible hydrodynamic turbulence, the non-linear advection term distributes energy among scales to both momentum-fluctuations and mass-density fluctuations. The non-linear energy transfer among momentum fluctuations appears to be scale-independent in the absence of viscous forces. The non-linear energy transfer to density-fluctuations is not independent of the spectral scale. Non-linear energy transfer to density-fluctuations is stronger at smaller scales. As a result, while momentum-transfer is flat and mass-density transfer is stronger at smaller scales, the transfer among velocity fluctuations is dampened, leading to steeper velocity power-

spectra in compressible turbulence.
Additionally, the ratio of energy that is transferred by non-linear interactions to density-fluctuations increases, the more the density-field is compressed. This observation might explain why power-spectra in compressible hydrodynamic turbulence are not universal, but subject to the degree of compression of the density-field, induced by the non-linear term in supersonic turbulence.

6.2 Compressible MHD turbulence

Magnetic fields alter the flow conditions of the turbulence. In addition to the sonic Mach number $\mathcal{M}_\mathrm{s}$, the Alfvén Mach number $\mathcal{M}_\mathrm{A}$ is likely to influence to the statistical-ensemble behavior of the turbulent system. The Alfvén Mach number, the ratio of the average flow velocity to the average Alfvén velocity, reflects the influence of the magnetic fields on the turbulence. Super-Alfvénic turbulence ($\mathcal{M}_\mathrm{A} > 1$) can be globally isotropic (see [5], page 200). In this case, the magnetic-field fluctuations are moved along with the plasma. In the sub-Alfvénic case, the velocity fluctuations are subject to a strong locally-homogeneous magnetic field, and the perpendicular motions become essentially incompressible. The focus of this work is the statistical-ensemble behavior of isotropic MHD turbulence (thus super-Alfvénic turbulence), reflected by time-averaged power-spectra and density PDFs, and the influence that both $\mathcal{M}_\mathrm{s}$ and $\mathcal{M}_\mathrm{A}$ exert on the statistical properties of the turbulence. Thus, the results of two simulation runs are presented. The first run covers approximately 18 dynamical times of supersonic and super-Alfvénic MHD turbulence, computed on a regular grid at 512^3 resolution. The parameter $\mathcal{M}_\mathrm{s}$ is varied from the mildly-supersonic regime to the highly-supersonic regime, covering $1.5 \leq \mathcal{M}_\mathrm{s} \leq 5.5$. $\mathcal{M}_\mathrm{A}$ is held fixed at approximately 1.6. Both the magnetic field and the velocity field are forced at wave numbers $2 \leq k \leq 3$, in a non-helical way. That means that the cross-helicity $\mathbf{v}_f \cdot \mathbf{b}_f$ of the forcing is zero. The ratio of forcing amplitudes F_v/F_b is kept constant at a value of 20. The choice of the forcing ratio yields an Alfvén-Mach number of $\mathcal{M}_\mathrm{A} \approx 1.66$ independent of the sonic Mach number $\mathcal{M}_\mathrm{s}$ of the turbulent flow.
The second run, computed on a regular grid with a resolution of 1024^3, reflects the influence of increasing magnetic-fields, while the sonic Mach number is held fixed at $\mathcal{M}_\mathrm{s} \approx 3$. In its saturated state, the ratio of magnetic energy to kinetic energy is approximately 1/3 and the average Alfvén Mach number reaches approximately 1.6. The parameters of the two runs are outlined in Table 6.5. Figures 6.16 and 6.17 show cuts through the computational domain at $z = 1/2$ of a statistically steady-state MHD turbulence with $\mathcal{M}_\mathrm{s} = 3$ and $\mathcal{M}_\mathrm{A} = 1.66$. The spatial structure of *e.g.* the velocity fluctuations of the MHD turbulence in Firgure 6.16 can be compared to the velocity fluctuations of a hydrodynamic turbulence at the same sonic Mach number (see Figure 6.1). This comparison shows the stretching of eddies in the MHD case. The structures of the velocity field in hydrodynamic turbulence (see Figure 6.1) are spatially homogeneous while the structures of the MHD velocity-fluctuations are spatially stretched. The cut through the absolute value of the magnetic field shows both the strong alignment of the density fluctuations with the magnetic-field fluctuations and the non-space filling characteristics of both magnetic-field and the density field. Absolute values of both the magnetic fields and the mass-density are concentrated in a small fraction of the overall computational domain, while large fractions of space are almost field-free (see [5], page 200).

run	MHD 512^3	MHD 1024^3
dynamical times	18.5	3.8
sonic Mach number $\mathcal{M}_\mathrm{s}$	1.5-5.5	2.8
Alfvén Mach number $\mathcal{M}_\mathrm{A}$	1.6 ± 0.6	$\infty - 1.6$
# of snapshots	1180	680
# of processes	512	512
Forcing	solenoidal	solenoidal
F_0^v/F_0^b	20	20
Forcing range	$2 \leq k \leq 3$	$2 \leq k \leq 3$

Tab. 6.5: Overview of the parameters in the forced MHD turbulence simulation-runs

All diagnostics applied to the hydrodynamic simulation runs are also studied for the MHD-simulation runs. In addition, power-spectra of the magnetic field are captured at each snapshot in time. Hence, total-energy spectra and residual-energy spectra are captured. The spectral quantities described above in the hydrodynamic diagnostics Chapter 6.1.1 are completed by:

- magnetic-field fluctuations $b^2(k)$
- total energy $1/2 \left|\rho v^2 + b^2\right| (k)$
- residual energy $1/2 \left|\rho v^2 - b^2\right| (k)$

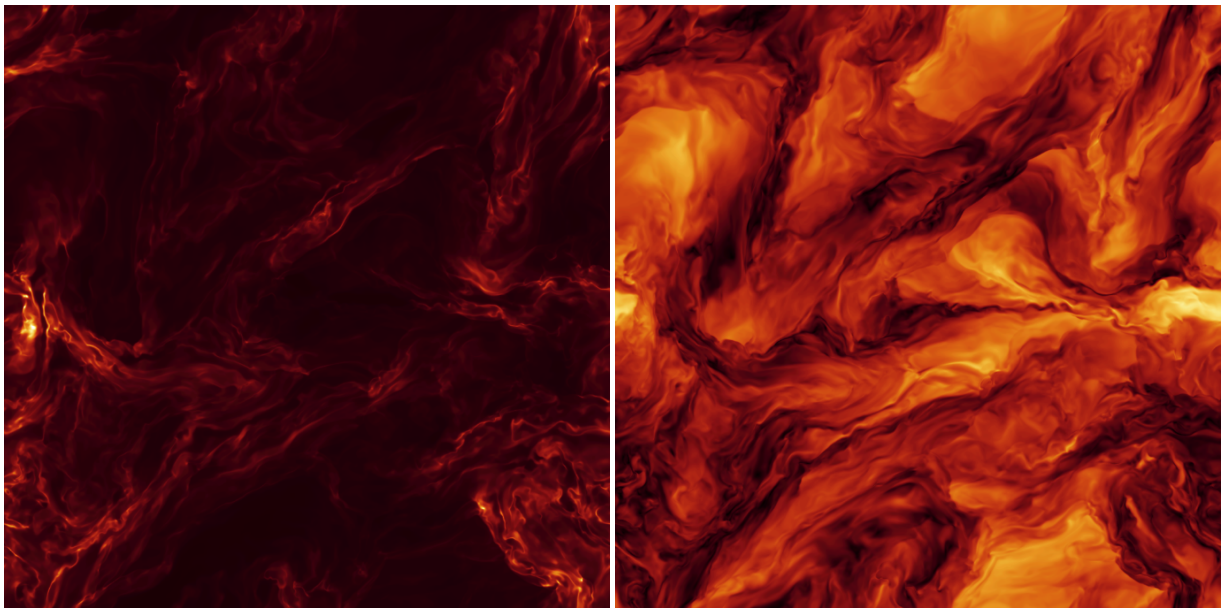

Fig. 6.16: Cuts through the density field (LHS) and the velocity-field intensity (RHS) in a fully developed $\mathcal{M}_s = 3$ and $\mathcal{M}_A = 1.66$ MHD turbulence. High values of the according intensities are marked by bright yellow colors, small values are black. Strong compression is observed where the velocity is almost 0 due to compression flows at the edges of counter-rotating eddies.

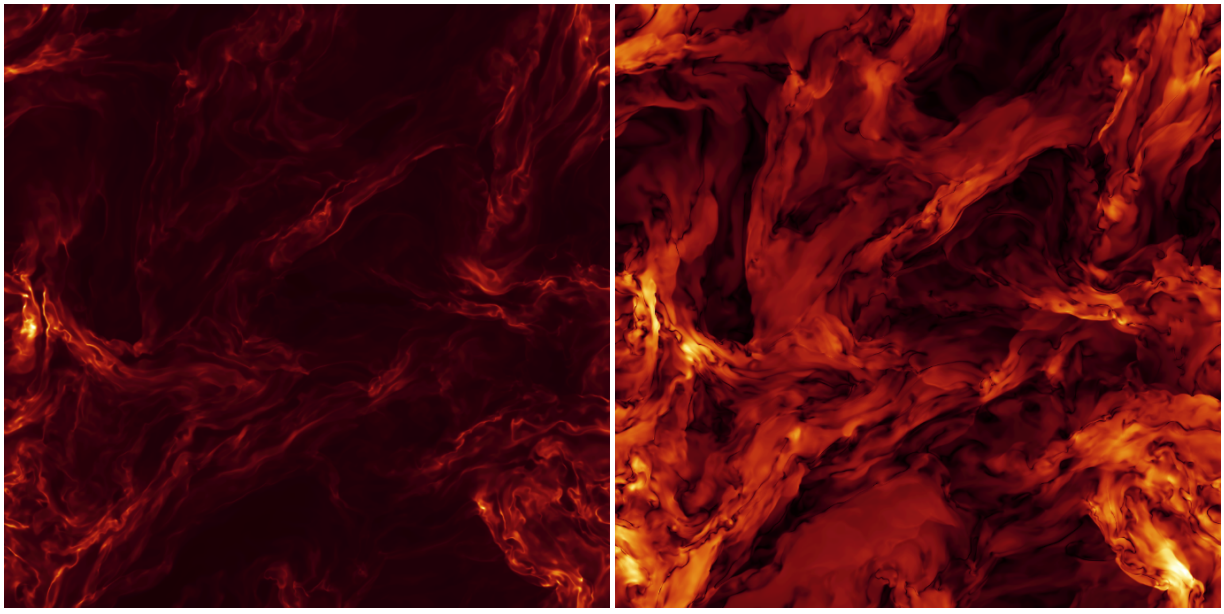

Fig. 6.17: Cuts through the density field (LHS) and the magnetic-field intensity (RHS) in a fully developed $\mathcal{M}_s = 3$ and $\mathcal{M}_A = 1.66$ MHD turbulence. The color scheme is identical to that of Figure 6.16. The magnetic-field strength and the density field are spatially aligned.

6.2.1 Time evolution of the characteristic flow quantities

In the 512^3-run, the flow is initialized with a constant mass-density $\rho_0 = 1$ and zero flow velocity. The magnetic field is also initially set to 0. The combined kinetic and magnetic forcing at large scales injects energy into the system and the flow becomes turbulent and statistically stationary after approximately one dynamical time. Figure 6.18 shows the time evolution of both the kinetic and magnetic energies, averaged over the computational domain. As described in the hydrodynamic case, the strong fluctuations of the kinetic energy in time are again more pronounced at higher average flow-velocities. The magnetic energy does not reflect strong time changes around its mean value.
Figure 6.19 shows the time evolution of the sonic Mach number and the Alfvén Mach number in the same run. While $\mathcal{M}_\mathrm{s}$ covers the range between 1.5 and 5.5, $\mathcal{M}_\mathrm{A}$ is held constant in an interval around 1.6(6). Towards the end of the simulation, for $t/t_\mathrm{d} > 15$, $\mathcal{M}_\mathrm{A}$ increases slightly to values around 2.2.
The time evolution of the kinetic and magnetic energies of the 1024^3 run are shown in Figure 6.20. The

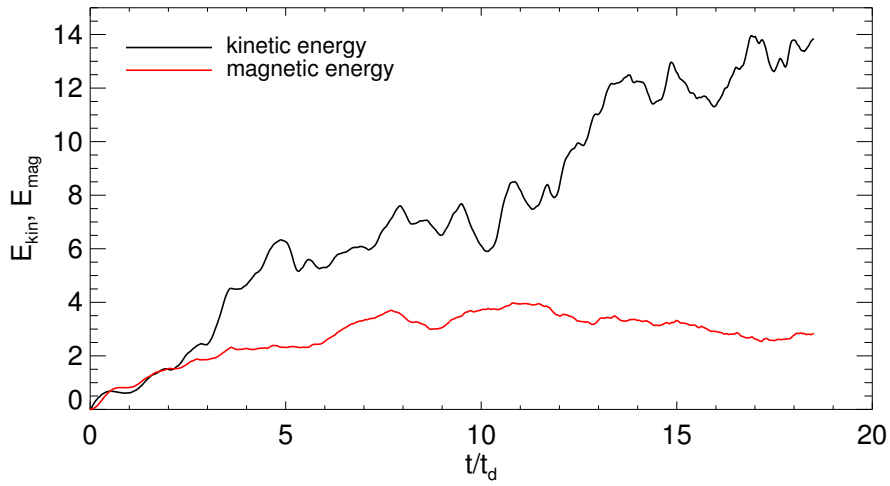

Fig. 6.18: Time evolution of kinetic energy and magnetic energy in the 512^3 simulation run. After t/t_d=2, the flow is fully turbulent. The run covers sonic Mach numbers between 1 and 5.

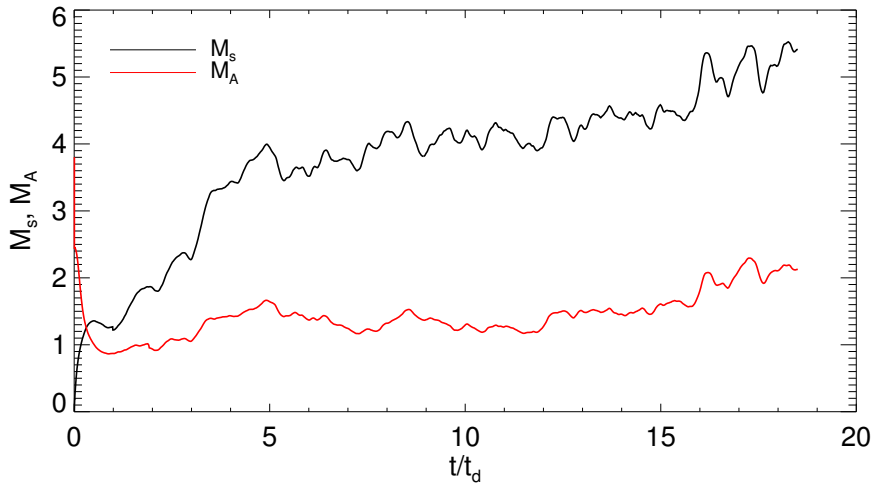

Fig. 6.19: Time evolution of the sonic Mach number and the Alfvén Mach number in the 512^3 simulation run. While $\mathcal{M}_\mathrm{A}$ is kept within an interval between 1.2 and 2.2, $\mathcal{M}_\mathrm{s}$ increases from 1.5 to 5.5.

starting point of this simulation is a fully-developed Mach 3, 1024^3 hydrodynamic turbulence, described in Chapter 6.1. The magnetic field is initially zero and increases within three dynamical times to its

saturation value of 1/3 of the kinetic energy of the turbulence. From the log-log plot of the magnetic energy evolution three phases of evolution can be distinguished. The first phase is characterized by a steep power-law increase of the magnetic energy, due to coupling of magnetic fluctuations to velocity fluctuations on small scales. In this first phase until $t/t_\mathrm{d} = 0.4$, magnetic energy grows with time as $t^{3.8(2)}$. When small-scale fluctuations reach equipartition, *i.e.* a comparable amount of kinetic energy and magnetic energy at small scales, the magnetic-energy increase slows down. A second phase of slower growth of the magnetic energy (with $t^{1.75(8)}$) follows until the system saturates at $t/t_\mathrm{d} = 2.8$.
The kinetic energy increases from an initial value of 2.9 to 3.7 in three dynamical times. During this increase, the RMS sonic Mach number of the flow is kept constant at approximately 2.8. During the initial flow-crossing times, the Alfvén Mach number decreases from an initially infinite value (due to $\mathcal{M}_\mathrm{A} \sim 1/|B|$) to 1.66 (see Figure 6.21).

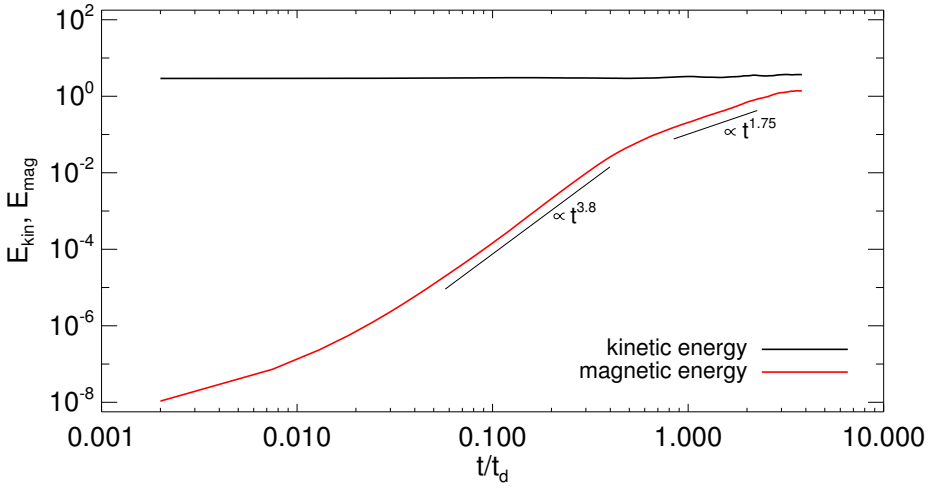

Fig. 6.20: Time evolution of kinetic energy and magnetic energy in the 1024^3 simulation run. The magnetic energy shows two phases of growth, then saturates after $t/t_\mathrm{d} = 3$.

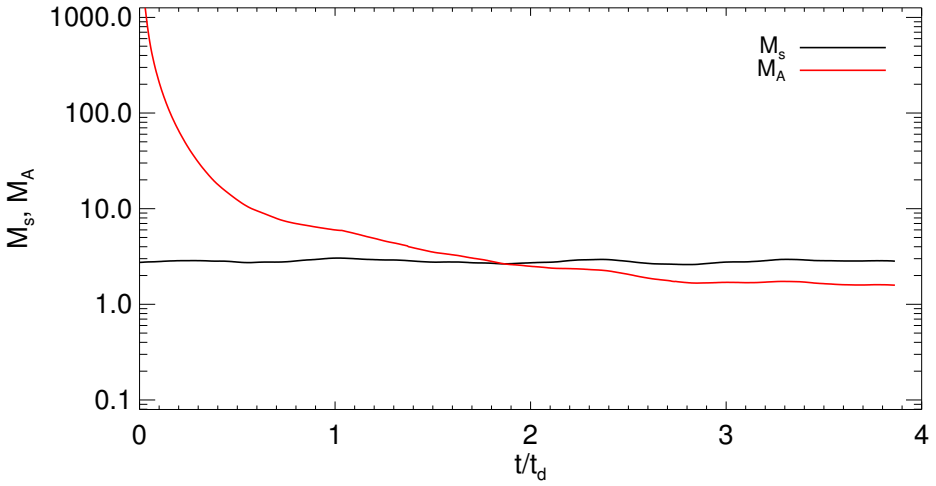

Fig. 6.21: Time evolution of the sonic Mach number $\mathcal{M}_\mathrm{s}$ and the Alfvén Mach number $\mathcal{M}_\mathrm{A}$ in the 1024^3 simulation run. $\mathcal{M}_\mathrm{A}$ saturates after $t/t_\mathrm{d} = 2.8$ to a value of 1.66.

6.2.2 Spectral-scaling in MHD turbulence

The influence of the RMS sonic Mach number of the flow on spectral scaling properties of MHD flow quantities are computed *via* time-averages of spectral snapshots within bins of approximately constant $\mathcal{M}_s$. The power-spectra of velocity-fluctuations are shown in Figure 6.22. Like in the hydrodynamic case, the time-averaged spectra yield a wave-number range with power-law scaling of the spectra for $4 \leq k \leq 7$. The best-fit scaling exponent β for mildly-supersonic turbulence ($\mathcal{M}_s = 1.6$) takes a value of 1.98(8). The MHD-velocity power-spectrum of the mildly-supersonic and super-Alfvénic regime is considerably steeper than the comparable hydrodynamic velocity power-spectrum. In the supersonic regime of $\mathcal{M}_s = 4.8$, the velocity power-spectrum yields an even steeper scaling. The best-fit scaling exponent is measured to be $\beta = 2.29(7)$. The bottleneck phenomenon in the wave-number range $8 \leq k \leq 30$ is more pronounced for the MHD power-spectra than for the hydro power-spectra (see Figure 6.3 for comparison). For wave numbers k greater than 30, dissipation becomes dominant and the power-spectra fall off steeply. The sonic Mach number $\mathcal{M}_s$ appears to have an effect on the scaling-exponent of velocity power-spectra, which is comparable to the hydrodynamic case. Higher sonic Mach numbers lead to steeper velocity power-spectra. Even the quantitative effect, an increase of β by approximately 0.3 (2.29(7)-1.98(8)) from transonic to supersonic is of similar magnitude to the increase of β by approximately 0.29 in the hydro case.

The kinetic energy spectra, subject to the two sonic Mach number regimes, are illustrated in figure 6.23.

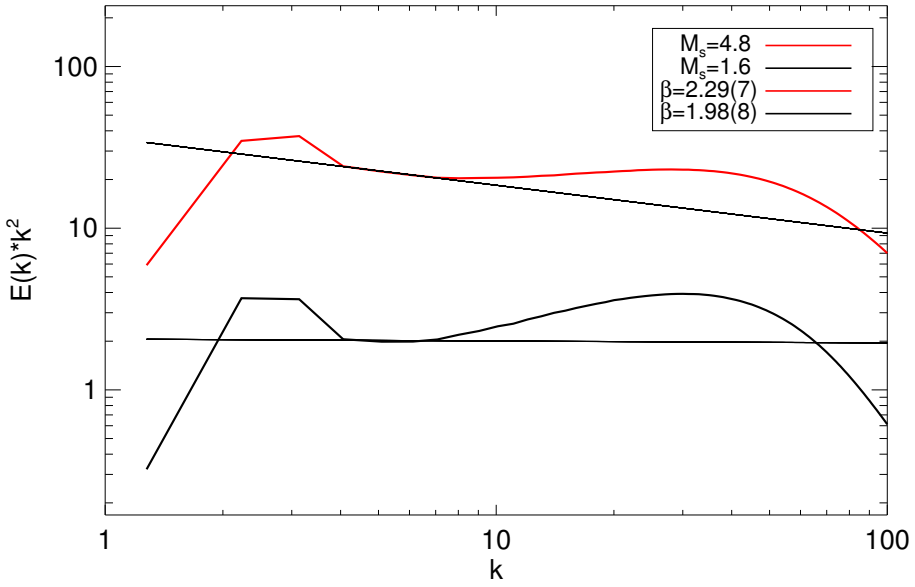

Fig. 6.22: Compensated and time-averaged velocity power-spectra within two sonic Mach number regimes ($\mathcal{M}_s = 4.8$ and $\mathcal{M}_s = 1.6$) at 512^3-resolution. Power spectra yield power-law scaling for wave numbers $4 \leq k \leq 7$, the best-fit scaling exponents are obtained as $\beta = 1.98(8)$ in the mildly-supersonic regime and $\beta = 2.29(7)$ in the highly-supersonic regime. The straight lines represent the best-fit to the scaling range.

In the mildly-supersonic regime, the kinetic-energy spectrum scales with $k^{-1.78(7)}$. The scaling is thus significantly steeper than under comparable hydrodynamic conditions. At high sonic Mach numbers, the kinetic-energy spectrum flattens. At $\mathcal{M}_s = 4.8$, the scaling exponent is measured to be $\beta = 1.64(7)$. Like in the hydrodynamic case, an increase of the average flow-velocity leads to a flattening of the kinetic-energy spectrum. The difference from kinetic energy-spectra in the MHD case to kinetic energy-spectra in the hydrodynamic case is the magnitude of the scaling exponents. Over all $\mathcal{M}_s$ the kinetic energy spectra in MHD turbulence are steeper than in hydrodynamic turbulence.

The power spectra of the density-weighted velocity $\rho^{1/3}v$ were proposed to scale with a Kolmogorov scaling exponent of $\beta = 5/3$ by Kowal and Lazarian, based on their results of 512^3 simulations of subsonic and supersonic MHD [34]. The results of the 512^3 simulations for the supersonic, super-Alfvénic regime of this work yield steeper scaling for the power spectra of the density-weighted velocity. Figure 6.24 shows

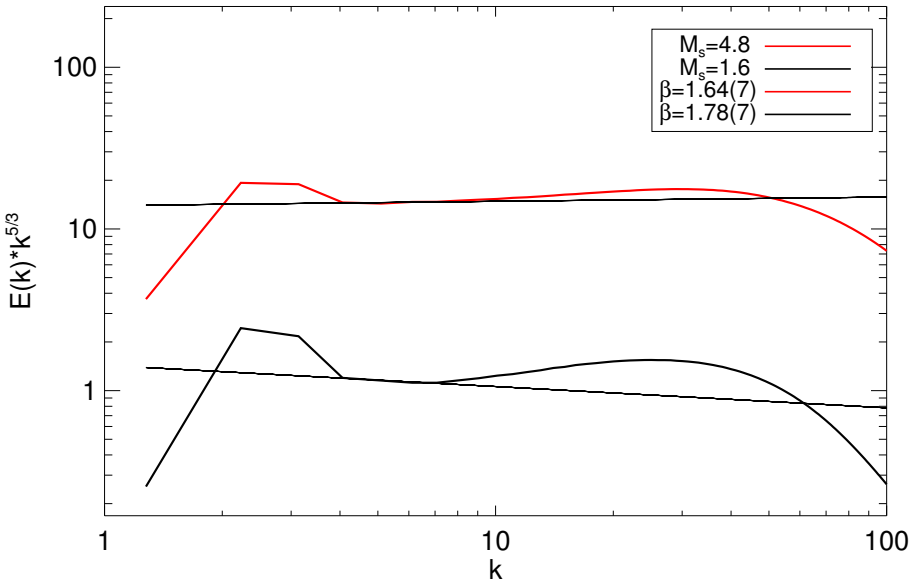

Fig. 6.23: Time-averaged kinetic-energy spectra within two sonic Mach number regimes ($\mathcal{M}_\mathrm{s} = 4.8$ and $\mathcal{M}_\mathrm{s} = 1.6$), compensated by $k^{5/3}$, at 512^3-resolution. The energy spectra yield a scaling range for $4 \leq k \leq 7$, the best-fit scaling exponents are obtained as $\beta = 1.78(8)$ in the mildly-supersonic regime and $\beta = 1.64(7)$ in the highly-supersonic regime.

the power spectra for the mildly-supersonic and highly-supersonic regime. The best-fit scaling-exponent is measured to be $\beta = 1.88(7)$ for $\mathcal{M}_\mathrm{s} = 1.6$ and $\beta = 1.91(6)$ for $\mathcal{M}_\mathrm{s} = 4.8$. In both regimes, the scaling is significantly steeper than the Kowal and Lazarian spectra. A clear influence of the sonic Mach number on the scaling of the density-weighted velocity cannot be extracted from the obtained results. The scaling exponents at $\mathcal{M}_\mathrm{s} = 1.6$ and $\mathcal{M}_\mathrm{s} = 4.8$ agree within statistical errors. The sonic Mach number of the flow does not have a significant impact on the scaling exponents of the density-weighted velocity power-spectra, either in MHD or hydrodynamic results.

The scaling properties of the velocity power-spectrum, the kinetic-energy spectrum, and the density-weighted velocity spectrum exhibit an influence of the sonic Mach number on the scaling exponents. This appears to happen in a comparable way the hydrodynamic scaling-exponents are influenced by the sonic Mach number. The difference of the scaling exponents of the MHD velocity fluctuations to the kinetic-energy fluctuations can be plotted *vs.* $\mathcal{M}_\mathrm{s}$ (see Figure 6.25). The difference of the scaling exponents can be parametrized with 3α, as in the hydrodynamic case, using:

$$\frac{|\rho^{1/2} v|_k^2}{|v|_k^2} \sim k^{3\alpha}. \tag{6.21}$$

Figure 6.25 shows the obtained 3α, computed at each spectral snapshot. Like in the hydrodynamic case, higher average flow-velocity lead to an increase in the parameter 3α. The parameter 3α can be associated with the degree of compression. For the highest sonic Mach number bin $\mathcal{M}_\mathrm{s} = 4.9(4)$, a value of $3\alpha = 0.65(11)$ is obtained. The steepening of the velocity power spectra with regard to the flattening of the kinetic energy spectrum corresponds to $\alpha = 0.22(4)$ at $\mathcal{M}_\mathrm{s} = 4.9(4)$. This value agrees well with the value of α given by Kowal and Lazarian [34], stated as $\alpha \approx 0.23$. Kowal and Lazarian's value for the degree of compression results from numerical simulations of strongly magnetized MHD turbulence at resolution of 512^3, $\mathcal{M}_\mathrm{s} = 7$, and $\mathcal{M}_\mathrm{A} = 0.7$. Their value of α does not differ significantly from ours, even though Kowal and Lazarian simulated MHD turbulence subject to a strong mean magnetic-field. The agreement gives rise to the question, whether the Alfvén Mach number significantly influences the difference in the power spectrum of the velocity and the kinetic energy spectrum. Data of the KT code's 1024^3 run is used to illuminate the influence of the Alfvén Mach number on the degree of compression. In the high $\mathcal{M}_\mathrm{A}$ limit, the turbulence behaves like a compressible hydrodynamic turbulence with little magnetic effect on the dynamics (see figure 6.26). The scaling-exponent of the velocity power-spectrum is measured to be $\beta = 1.87(4)$. The kinetic-energy spectrum scales with a measured exponent of $\beta = 1.54(3)$. The difference

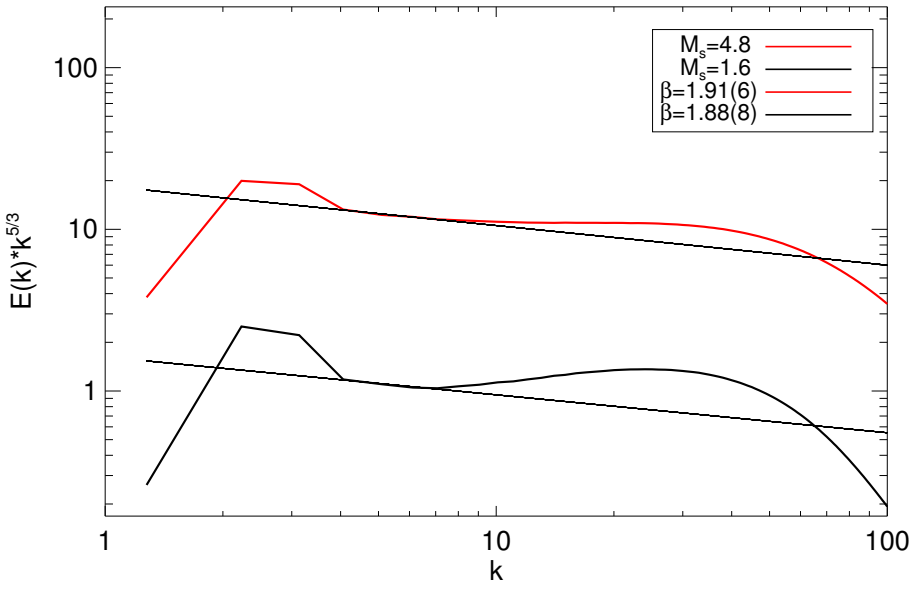

Fig. 6.24: Power-spectra of the density-weighted velocity $\rho^{1/3}v$, at 512^3-resolution. The spectra are time-averaged on two sonic Mach number regimes ($\mathcal{M}_\mathrm{s} = 4.8$ and $\mathcal{M}_\mathrm{s} = 1.6$), and compensated by $k^{5/3}$. The power-spectra yield a scaling range for $4 \leq k \leq 7$, the best-fit scaling exponents are obtained as $\beta = 1.88(8)$ in the mildly-supersonic regime and $\beta = 1.91(6)$ in the highly-supersonic regime.

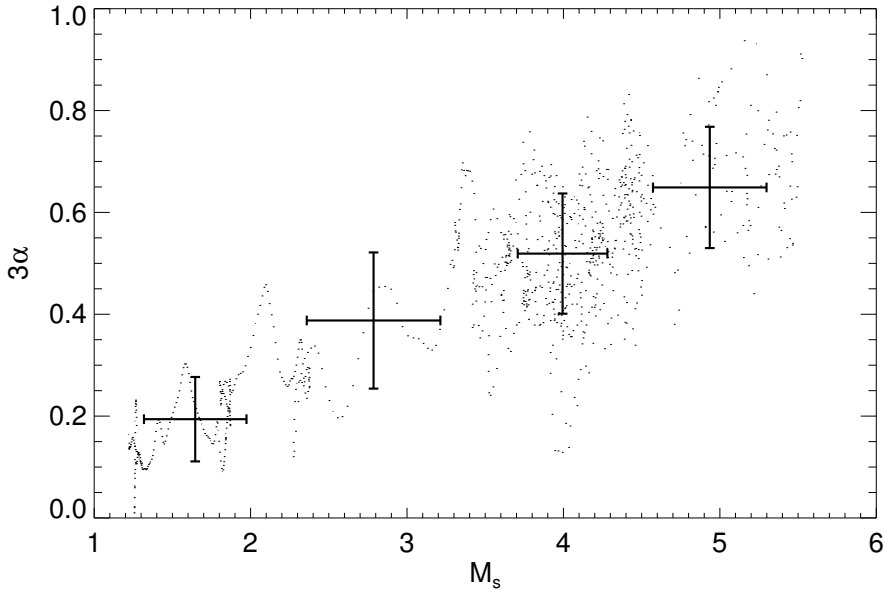

Fig. 6.25: Difference of the scaling exponents of the kinetic-energy spectrum and the velocity power-spectrum, denoted by 3α *vs.* $\mathcal{M}_\mathrm{s}$, from the 512^3-run. The parameter 3α grows approximately linearly with $\mathcal{M}_\mathrm{s}$ for $1.2 \leq \mathcal{M}_\mathrm{s} \leq 5.5$.

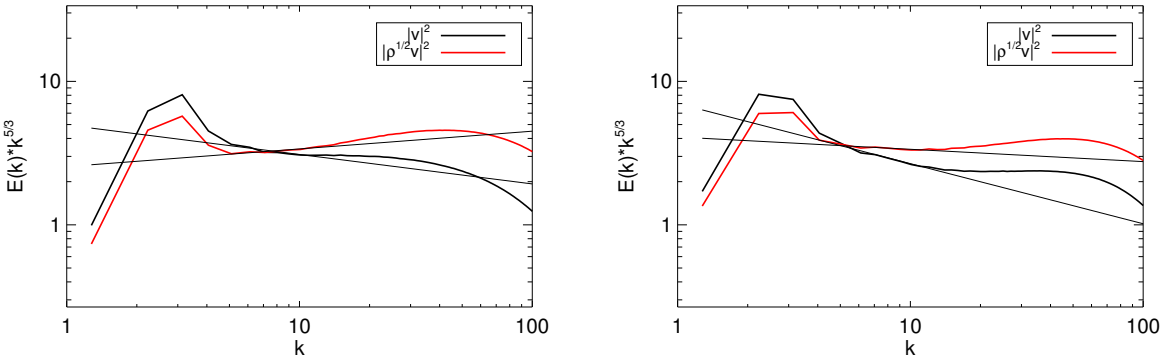

Fig. 6.26: Power-spectra of the kinetic-energy fluctuations and the velocity fluctuations, both at $\mathcal{M}_\mathrm{s} = 3$ and 1024^3-resolution. The LHS shows the time-averaged spectra at high Alfvén Mach numbers $\mathcal{M}_\mathrm{A} \gg 10$, the RHS shows the according time-averaged spectra at $\mathcal{M}_\mathrm{A} \approx 1.7$.

of the scaling exponents of the velocity power-spectrum and the kinetic-energy spectrum averaged over half a dynamical time is $3\alpha = 0.33(3)$. In the saturated state of $\mathcal{M}_\mathrm{A} \approx 1.66$, the velocity power-spectrum is steeper than in the high $\mathcal{M}_\mathrm{A}$-limit. The best-fit to the spectrum for wave numbers $4 \leq k \leq 12$ yields $\beta = 2.09(2)$. The kinetic-energy spectrum also steepens and the scaling exponent is $\beta = 1.75(3)$. The degree of compression, calculated by the scaling difference, is measured to be $3\alpha = 0.34(4)$. This indicates that even though the scaling exponents for the individual spectra steepen drastically with a decrease in $\mathcal{M}_\mathrm{A}$, the difference of the scaling is not significantly influenced by the relative magnetic-field strength. In the bottleneck range of wave numbers $12 < k < 40$, the power-spectrum of the velocity-fluctuations becomes shallower at $\mathcal{M}_\mathrm{A} = 1.7$, compared to $\mathcal{M}_\mathrm{A} > 10$. This might explain the large difference of the KT code's results and those obtained by Kritsuk *et al.* [37]. They report scaling exponents for the velocity power-spectra at $\mathcal{M}_\mathrm{s} = 10$ for three Alfvén Mach number regimes $\mathcal{M}_\mathrm{A} \approx 10, \approx 3, \approx 1$. The reported scaling-exponents are $\beta = 1.94$ at $\mathcal{M}_\mathrm{A} \approx 10$, $\beta = 1.62$ at $\mathcal{M}_\mathrm{A} \approx 3$, and $\beta = 1.51$ at $\mathcal{M}_\mathrm{A} \approx 1$, obtained on time-averages of 512^3 simulations. It appears that the spectral range of power-law fitting was chosen for larger k than in this work, possibly including fitting the bottleneck.

6.2.3 Power-spectrum of the magnetic-field fluctuations

In decaying compressible MHD turbulence, the magnetic-energy spectrum does not show a clear range of power-law scaling (see Figure 4.11). For forced MHD turbulence, the magnetic-energy spectrum is shown in figure 6.27, for $\mathcal{M}_\mathrm{s} \approx 3$ and $\mathcal{M}_\mathrm{A} \approx 1.66$. For comparison, the spectrum of the kinetic energy is plotted with the magnetic-energy spectrum. The obtained best-fit scaling exponent for the time-averaged magnetic-energy spectrum is $\beta = 0.52(10)$. The magnetic energy is smaller than the kinetic energy for all wave numbers k. In the dissipation range, $k > 60$, the magnetic-energy spectrum falls off with a steepness comparable to the kinetic energy fall-off. In the driving range of $k = 2$ and 3, the forcing determines the ratio $E_\mathrm{kin}/E_\mathrm{mag}$. In the KT code simulations, the ratio of forcing magnitudes $F_0^v/F_0^b = 20$, and thus the amplitude of the large-scale magnetic-field fluctuations is small relative to the amplitude of the kinetic energy.

6.2.4 Compressible and solenoidal part of velocity-fluctuations

In compressible MHD turbulence, the ratio of compressible to rotational part of the velocity power-spectrum, denoted by $\chi(k)$, is defined as in the hydrodynamic case (see equation (6.9)). Integrated over all wave numbers k, the ratio χ measures the importance of compressible and shock-related motions over rotational motions within the MHD turbulence. In figure 6.28, time-averaged power-spectra of the compressible velocity-fluctuations and the rotational velocity-fluctuations are shown. Solenoidal forcing of the velocity field is used for both MHD simulation runs. This forcing causes the ratio $\chi(k)$ to be artificially large in the spectral wave-number range of $k = 2, 3$. The spectra are computed using data from the 1024^3 run at $\mathcal{M}_\mathrm{s} \approx 3$ and $\mathcal{M}_\mathrm{A} \approx 1.66$. The amplitude of the solenoidal velocity-fluctuations is larger than the amplitude of the compressible velocity-fluctuations for all wave numbers $k < 250$. In the far dissipation-range, *i.e.* for wave numbers $k > 250$, numerical dissipation dampens solenoidal fluctua-

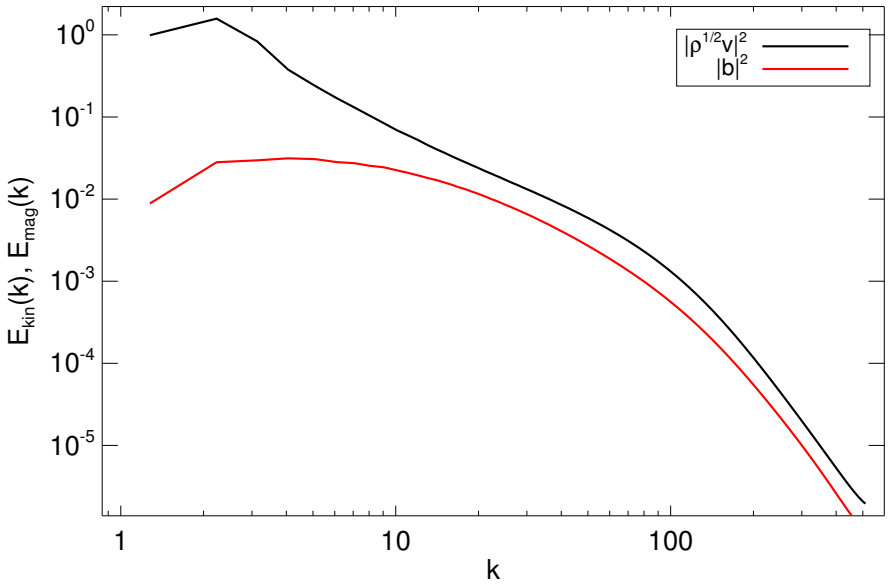

Fig. 6.27: Time-averaged magnetic-energy spectrum and kinetic-energy spectrum at $\mathcal{M}_s \approx 3$ and $\mathcal{M}_A \approx 1.66$. The resolution is 1024^3, and the plots are uncompensated. The amplitude of the magnetic energy is smaller than the amplitude of the kinetic energy over all wave numbers k.

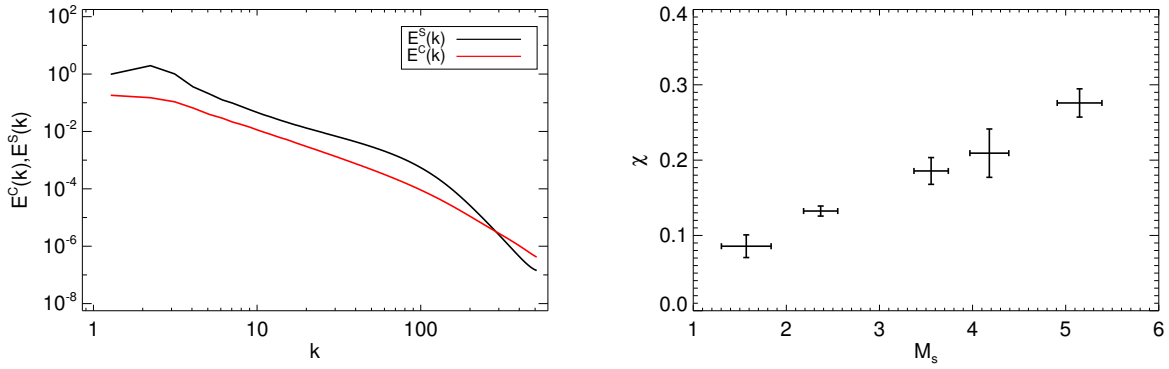

Fig. 6.28: The LHS shows power-spectra of the compressible velocity-fluctuations and the solenoidal velocity-fluctuations at $\mathcal{M}_s = 3$ and $\mathcal{M}_A = 1.66$, at 1024^3-resolution. On the RHS, the ratio χ is plotted for several sonic Mach number bins, based on the 512^3-run. In MHD, the ratio χ grows less steeply with $\mathcal{M}_s$ than in the hydrodynamic turbulence.

tions stronger than dilatational fluctuations. The stronger dampening of solenoidal modes might explain the fact that only the solenoidal velocity power-spectrum exhibits the bottleneck phenomenon, while the compressible velocity power-spectrum does not show a bump in the near-dissipation range (see LHS of Figure 6.28). According to Falkovich [23], the amplitude of bottleneck depends on the spectral-scaling of power-spectra in the dissipation range, with wave number k. The bottleneck is stronger when dissipation grows faster than k^2 (see *e.g.* [36]). A power-law fit to the obtained power-spectra in the dissipation range shows that the solenoidal part is clearly dissipated faster than k^2, while the dilatational part is dissipated only slightly faster than k^2 (see LHS of Figure 6.28, for $k > 200$).
The ratio χ is computed as the ratio of k-integrated compressible over solenoidal velocity power-spectra (see equation (6.10)). For the statistically-stationary MHD turbulence at $\mathcal{M}_\mathrm{s} = 3$ and $\mathcal{M}_\mathrm{A} = 1.66$, the ratio of compressible over solenoidal strength is $\chi = 0.21(2)$. This ratio is significantly smaller than in solenoidally-forced hydrodynamic turbulence at $\mathcal{M}_\mathrm{s} = 3$, where $\chi = 0.30(3)$. Magnetic-field fluctuations thus increase the importance of the solenoidal velocity motions over compressible motions in the turbulence. This result can be explained by the fact that compressible velocity motions in MHD compress the plasma against the combined magnetic and thermal pressure. Since both magnetic pressure and thermal pressure are highly aligned in compressible MHD, the compressible velocity motions are more strongly dampened than in the pure hydrodynamic case.

6.2.5 Total energy and residual energy in MHD turbulence

For the total-energy spectrum of compressible MHD, $1/2(\rho v^2 + b^2)(k)$, scaling-predictions based on the models for incompressible MHD exist. The total-energy spectrum of incompressible MHD turbulence is predicted to scale with $k^{-\beta}$, with $\beta = 3/2$ in the IK-phenomenology and $\beta = 5/3$ in the GS-phenomenology. Shivamoggi's prediction, based on the two models, includes a steepening of the total-energy spectrum with an increase of the sonic Mach number and the according compression of the mass-density (see equation (2.87)). In addition to the sonic Mach number, the Alfvén-Mach number might influence the scaling properties of the total-energy spectrum. In Figure 6.29, the total-energy spectra, time-averaged onto sonic Mach number bins $\mathcal{M}_\mathrm{s} = \{2.4, 3.6, 4.2, 5.2\}$, are illustrated. Like for the flow quantities described above, the total-energy spectra yield a wave-number range of scaling for $4 \leq k \leq 7$. The spectra are compensated by $k^{3/2}$. The obtained scaling exponents take values around $3/2$, with no obvious influence of the average flow velocity on the scaling exponents. Table 6.6 outlines the values of β and their statistical errors. The obtained values lead to the conclusion, that the scaling exponent of the total-energy spectrum is more likely to be $3/2$ as predicted by Iroshnikov-Kraichnan in equation (2.50), rather than $5/3$ predicted by Goldreich-Shridar in equation (2.51). The prediction of steeper total-energy spectra for higher compression, proposed by Shivamoggi in equation (2.87), is not supported by the results of this work's numerical simulations.
The residual-energy spectra, subject to different sonic Mach number regimes, are shown in Figure 6.30.

$\mathcal{M}_\mathrm{s}$	2.4(2)	3.6(2)	4.2(2)	5.2(2)
β	1.48(4)	1.54(6)	1.52(6)	1.53(7)

Tab. 6.6: Resulting scaling exponents β of total-energy spectra for several sonic Mach number regimes of the 512^3-run. $\mathcal{M}_\mathrm{A}$ is held approximately constant at 1.6 ± 0.6.

The four time-averaged spectra scale with the wave number k in the range of scales $4 \leq k \leq 8$. The scaling exponent appears to depend strongly on $\mathcal{M}_\mathrm{s}$. The residual-energy spectrum becomes significantly flatter at higher sonic Mach numbers. The scaling exponent decreases from a value of $\beta = 2.63(12)$ at $\mathcal{M}_\mathrm{s} = 2.4$ to $\beta = 1.70(9)$ at $\mathcal{M}_\mathrm{s} = 5.2$. The reason for this large change in β may not be determined by the sonic Mach number of the turbulence, but by the change of the ratio $E_\mathrm{kin}/E_\mathrm{mag}$. This ratio becomes larger for higher Mach numbers (see Figure 6.18). An increase in the ratio $E_\mathrm{kin}/E_\mathrm{mag}$ means that the residual-energy spectrum is dominated by the kinetic energy while the magnetic energy contribution becomes less important. In the limit of $\mathcal{M}_\mathrm{A} \to \infty$, thus $E_\mathrm{kin}/E_\mathrm{mag} \to \infty$, the residual-energy spectrum corresponds to the kinetic-energy spectrum, $E_\mathrm{res}(k) \to E_\mathrm{kin}(k)$. In Table 6.7, the scaling exponents of residual-energy spectra are outlined together with the sonic Mach number and the ratio $E_\mathrm{kin}/E_\mathrm{mag}$.
The scaling prediction of the residual energy with $E_\mathrm{res}(k) \sim k^{-2}$ for incompressible MHD turbulence is not observed in the results of the KT code's simulation of compressible MHD turbulence. In incom-

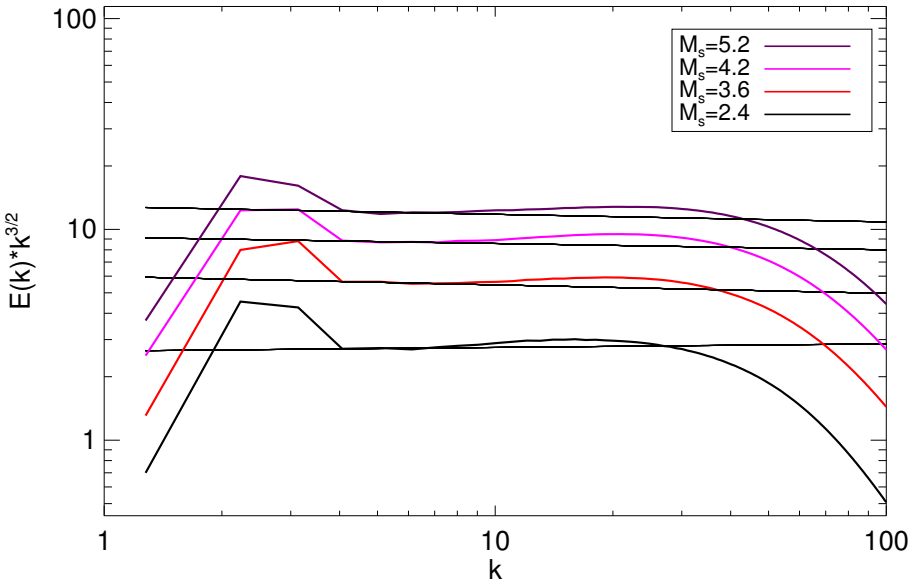

Fig. 6.29: Time-averaged total-energy spectra of the 512^3-run, compensated by $k^{3/2}$. The power-spectra yield a power-law scaling-range for $4 \leq k \leq 7$. The spectra scale as $k^{-3/2}$ within the statistical error, independent from the sonic Mach number of the turbulence. The obtained scaling exponents are outlined in Table 6.6. The straight lines represent the best-fit to the scaling-range.

$\mathcal{M}_\mathrm{s}$	2.4(2)	3.6(2)	4.2(2)	5.2(2)
β	2.63(8)	2.12(9)	1.98(8)	1.70(5)
$E_\mathrm{kin}/E_\mathrm{mag}$	1.4(2)	2.1(2)	2.7(7)	4.8(4)

Tab. 6.7: Resulting scaling exponents β of residual-energy spectra for several sonic Mach number regimes $\mathcal{M}_\mathrm{s}$. In addition, the ratio of $E_\mathrm{kin}/E_\mathrm{mag}$ is given to highlight the relative contribution of the magnetic energy to the residual energy.

pressible MHD turbulence, the absolute equilibrium argument includes that the magnitude of magnetic energy at all wave numbers is bigger than the magnitude of the kinetic energy. For small scales, this difference becomes infinitely small. In compressible MHD turbulence, due to the weighting of velocity fluctuations with the density, the ratio of kinetic energy to magnetic energy at larger scales can take any value. This ratio is reflected by the Alfvén Mach number $\mathcal{M}_\mathrm{A}$. But even in incompressible MHD the $E_\mathrm{res}(k) \sim k^{-2}$ prediction has not been unambiguously verified. Müller and Grappin [50] propose that the residual-energy spectrum scales with the kinetic-energy spectrum, so that $E_\mathrm{res}(k) \sim kE^2_\mathrm{kin}(k)$. They accordingly obtain a steeper than k^{-2} residual-energy spectrum, with $\beta \approx 7/3$, in direct numerical simulations at a resolution of 1024^3.

6.2.6 Mass-density probability distribution

The mass-density PDFs in isothermal MHD turbulence can also be described by a lognormal distribution [55]. Mass-density PDFs, time-averaged onto sonic-Mach number bins for the 512^3-run, are shown in Figure 6.31. Like in the hydrodynamic case, the width $\sigma_{\ln\rho}$ of the lognormal fit to the PDFs increases with the sonic Mach number. The obtained best-fit to the model equation (6.12) yields a parameter $b = 0.36(3)$, which is slightly lower than the b obtained in hydrodynamic case. A smaller parameter b indicates, that the magnetic-field fluctuations and the according magnetic pressure lessen the compression of the density-field, which is induced by the turbulent compression-flows. This might be related to the strong correlation of the density-fluctuations with the fluctuations of the magnetic pressure, that occur in the presence of compressional Alfvén waves.
In addition to the sonic Mach number, the Alfvén Mach number of the turbulence influences the width of the mass-density PDF. A such influence has not been systematically studied before. Figure 6.32 shows

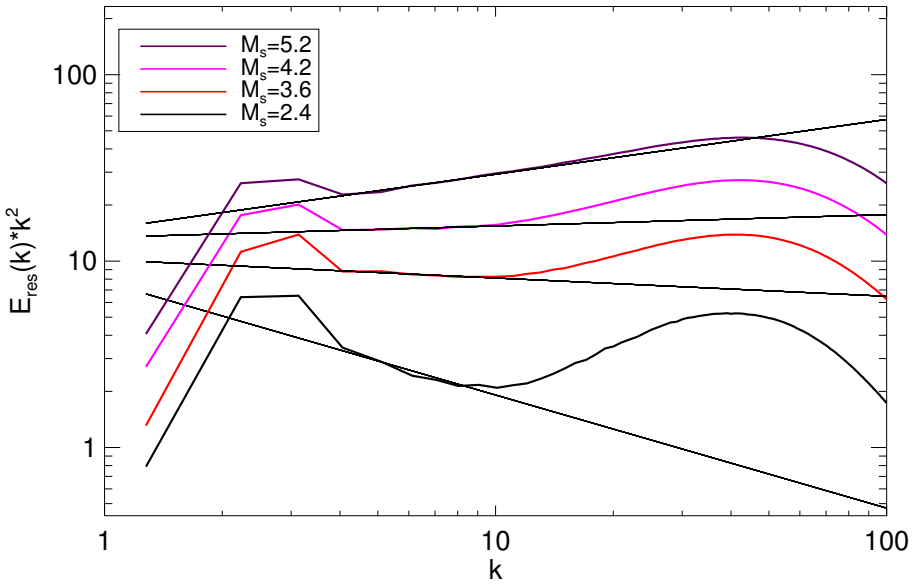

Fig. 6.30: Time-averaged residual-energy spectra, compensated by k^2, from the 512^3-run. The power-spectra yield a power-law scaling-range for $4 \leq k \leq 8$. The spectral scaling-exponent depends strongly on the ratio $E_{\rm kin}/E_{\rm mag}$, which increases during the run as the sonic Mach number increases. The straight lines represent the best-fit to the scaling range.

the width of the logarithmic-density lognormal fit as a function of the inverse RMS Alfvén Mach number $1/\mathcal{M}_{\rm A}$. In the high $\mathcal{M}_{\rm A}$ limit, the width of the lognormal fit to the logarithmic density pdf yields $\sigma_{\ln\rho} = 0.976(7)$. In the saturated state of the RMS magnetic-field strength at $\mathcal{M}_{\rm A} = 1.66$, the width of the best-fit is $\sigma_{\ln\rho} = 0.890(8)$. The density PDF narrows as the relative strength of the magnetic-field fluctuations increases. This observation can also be explained by the nature of compressional Alfvén waves. MHD compression flows are balanced by the combined magnetic and thermal pressure. With an increase in the Alfvén Mach number $\mathcal{M}_{\rm A}$, the magnetic pressure increases. Thus, velocity fluctuations lead to a smaller amount of density-compression. The functional form of the 1024^3 data (see RHS of Figure 6.32) implies a linear Ansatz to model the width of the density PDF as a function of $\mathcal{M}_{\rm A}$:

$$\sigma_{\ln\rho}(\mathcal{M}_{\rm A}) = \sigma_{\ln\rho}^{\rm hydro}\left(d\frac{1}{\mathcal{M}_{\rm A}}\right), \tag{6.22}$$

where d is a parameter. The model parameter d characterizes the dependence of $\sigma_{\ln\rho}$ on $1/\mathcal{M}_{\rm A}$ analogous to b, the model parameter that charactarizes the influence of $\mathcal{M}_{\rm s}$ on $\sigma_{\ln\rho}$. A fit of the 680 snapshots of the 1024^3-run to this model function (6.22) yields $d = -0.16(1)$, at $\mathcal{M}_{\rm s} = 2.8$. The model parameter $d = -0.16(1)$ differs significantly from zero. The width of the density PDF in compressible MHD turbulence is thus shown to depend on both $\mathcal{M}_{\rm s}$ and $\mathcal{M}_{\rm A}$ by the results of the KT-code's MHD simulations.

6.2.7 *Scaling of mass-density and momentum power-spectra*

The power-spectrum of momentum-density ρv is likely to yield power-law behavior, due to the mathematical structure of the time-rate of change of the Fourier-space components of the momentum-density (see equation (2.118)). The obtained power-spectra of momentum-density are shown in Figure 6.33, time-averaged on four sonic Mach number bins. At 512^3-resolution, the time-averaged momentum spectra follow a power-law within the spectral range of wave numbers $4 \leq k \leq 8$. The magnitude of the scaling exponent β depends strongly on the average sonic Mach number. In the mildly-supersonic regime, the best-fit to the spectrum within the scaling-range yields $\beta = 1.45(7)$. An increase in the RMS velocity is reflected in flatter momentum power-spectra. At the highest average sonic Mach number of $\mathcal{M}_{\rm s} \approx 5$, the momentum power-spectrum scales with $k^{-\beta}$, where $\beta = 0.92(7)$. Table 6.8 summarizes the scaling exponents for each Mach number bin. The strongly pronounced bottleneck of the spectrum in the mildly-supersonic regime becomes smaller for higher sonic Mach numbers. At $\mathcal{M}_{\rm s} \approx 5$, no bottleneck is

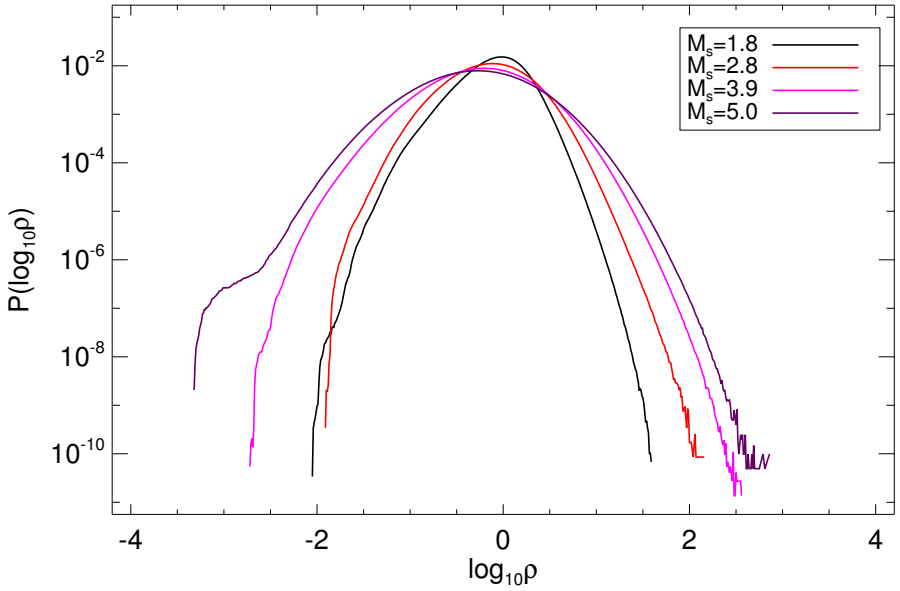

Fig. 6.31: Probability density function of the mass-density in MHD turbulence, time-averaged on Mach number bins. The distributions follow a log-normal function. The width of the distribution increases with $\mathcal{M}_\mathrm{s}$.

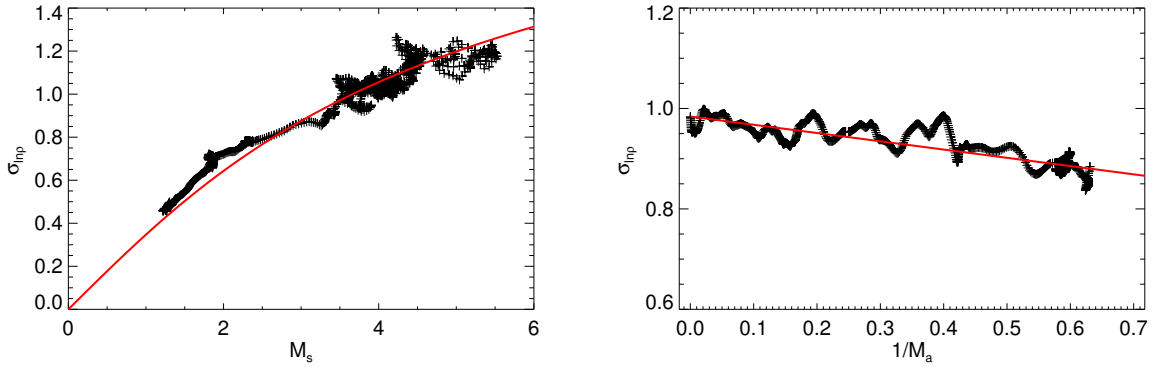

Fig. 6.32: Width σ of the logarithmic density PDF as a function of the RMS sonic Mach number $\mathcal{M}_\mathrm{s}$ (left). The individual points are the width of the lognormal fit to the 1180 individual PDF snapshots of the 512^3-run. The red line shows the best-fit of the data to the model function $\sigma^2_{\ln\rho} = \ln\left(1 + b^2\mathcal{M}_\mathrm{s}^2\right)$. The fit results in an obtained parameter $b = 0.36(3)$. The RHS shows the width $\sigma_{\ln\rho}$ plotted *vs.* the inverse Alfvén Mach number at fixed $\mathcal{M}_\mathrm{s} = 2.8$, based on all 680 snapshots of the 1024^3 run. The red line shows the fit of the data to the model function of equation (6.22).

$\mathcal{M}_\mathrm{s}$	1.6(2)	2.8(4)	4.0(3)	5.0(3)
$\beta_{\lvert\rho\mathbf{v}\rvert_k^2}$	1.45(7)	1.30(8)	1.05(7)	0.92(7)
$\beta_{\lvert\rho\rvert_k^2}$	0.94(7)	1.01(5)	0.84(6)	0.71(6)

Tab. 6.8: Resulting scaling-exponents β of momentum-density power-spectra and mass-density power-spectra for several sonic Mach number regimes $\mathcal{M}_\mathrm{s}$ of the 512^3-run.

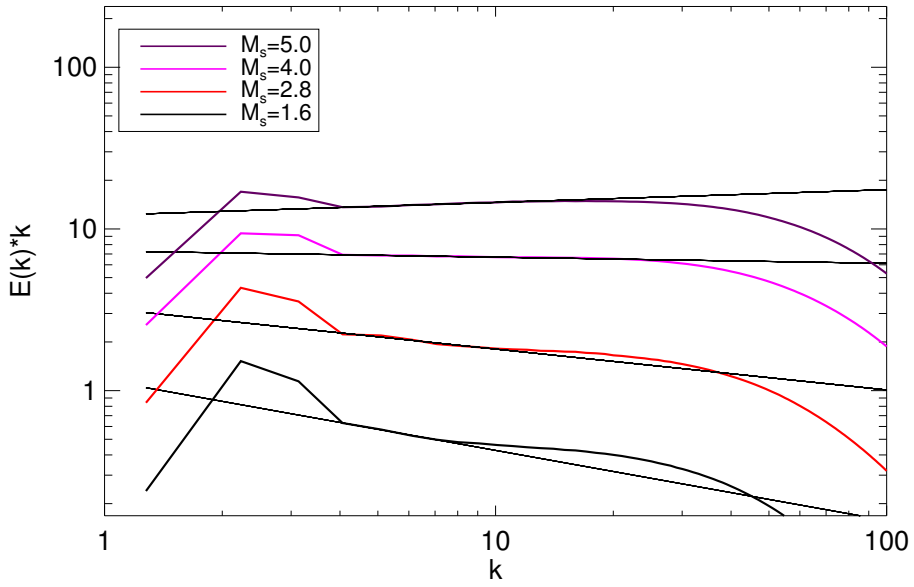

Fig. 6.33: Momentum-density power-spectra, time-averaged onto sonic Mach number bins. The spectra, from the 512^3-run, are compensated by k. The four spectra show a power-law behavior in the wave-number range $4 \leq k \leq 8$. At higher sonic Mach numbers, the power-spectrum becomes flatter.

present and the self-similar scaling-range spans a wave-number range of $4 \leq k \leq 14$. At $k \approx 30$, dissipation dominates the spectral shape and the power-spectrum falls off. In the mildly-supersonic regime, the spectral-scaling exponent of the momentum-density power-spectrum agrees with those obtained from transonic hydrodynamic turbulence (see Table 6.4). At higher sonic Mach numbers, the flattening of the momentum power-spectra is more pronounced in MHD turbulence than in hydrodynamic turbulence ($\beta = 0.92(7)$ in MHD *vs.* $\beta = 1.00(8)$ in hydro).
The power spectrum of the mass-density ρ is shown in Figure 6.34. Higher sonic Mach numbers lead to stronger compression and to a flattening of the mass-density power-spectrum. The time-averaged power-spectra at $\mathcal{M}_\mathrm{s} = 1.6$ and $\mathcal{M}_\mathrm{s} = 2.8$ yield spectral scaling in the range of wave numbers $4 \leq k \leq 10$, both scaling with an exponent of $\beta \approx 1.0$. At higher RMS sonic Mach numbers, the density power-spectra flatten and a scaling exponent of $\beta = 0.71(6)$ is obtained. Table 6.8 summarizes the scaling exponents of the best-fit to the time-averaged density power-spectra. Further evidence for a cascade led by momentum-density in compressible MHD turbulence is found from the scaling properties of the momentum-density power-spectrum measured at 1024^3 resolution. Power-spectra from the 512^3-resolution simulations reveal a limited 'separation of scales', a measurement of the spectral distance of energy-injection scales and dissipation scales. The near-dissipation range bottleneck in the power-spectra affects the wave-number range for $k > 8$, while the energy-injection affects the wave-number range of $k \leq 3$. The time-averaged momentum power-spectrum of the 1024^3 simulation results in a self-similar scaling range that covers the wave-number range of $4 \leq k \leq 14$. Within this range of wave-numbers, the momentum-density power-spectrum follows a power-law behavior and the statistical deviations of excitations levels from this power-law scaling are remarkably small. Figure 6.35 shows the according time-averaged momentum power-spectrum of the 1024^3-simulation run. The scale-separation is well developed, and the injection scales can be clearly distinguished from power-law scales and the bottleneck scales. The scaling-exponent of the power-law range is $\beta = 1.30(3)$, in agreement with the scaling exponent of the momentum-density power-spectrum of the corresponding 512^3-results ($\beta = 1.30(8)$).

6.2.8 Nonlinear-transfer of momentum in compressible MHD turbulence

The non-linear terms in the compressible MHD equations provide for the distribution of energy among all spectral scales. The non-linear transfer to momentum-density and mass-density is induced by the non-linear terms in Fourier space in equation (2.118). Both the time-rate of change of the momentum-density and the projected second time-derivative of the mass density exchange energy with the non-linear terms.

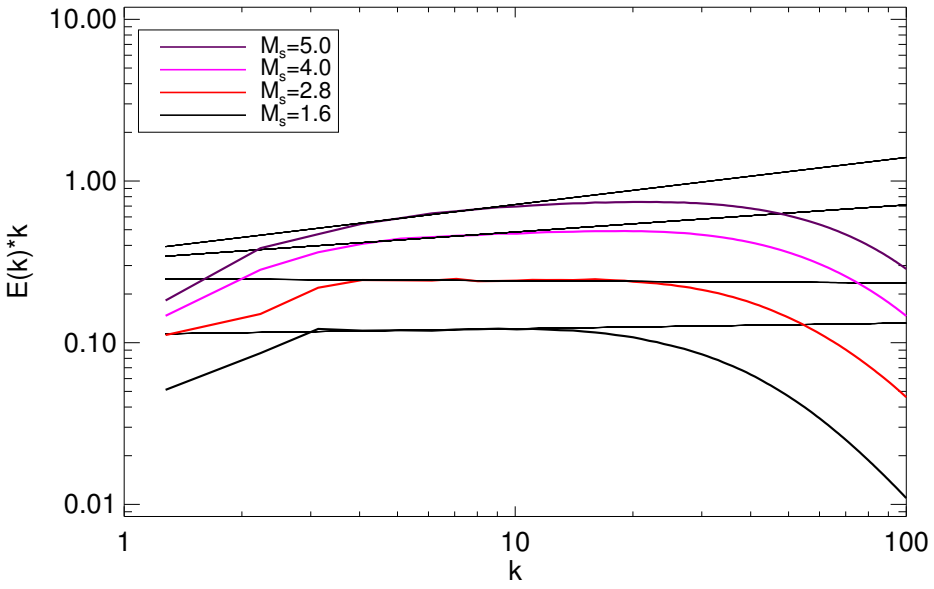

Fig. 6.34: Mass-density power-spectra in MHD turbulence, time-averaged onto sonic Mach number bins. The spectra are calculated during the 512^3-run and are compensated by k. The straight lines represent the best-fit to the scaling range.

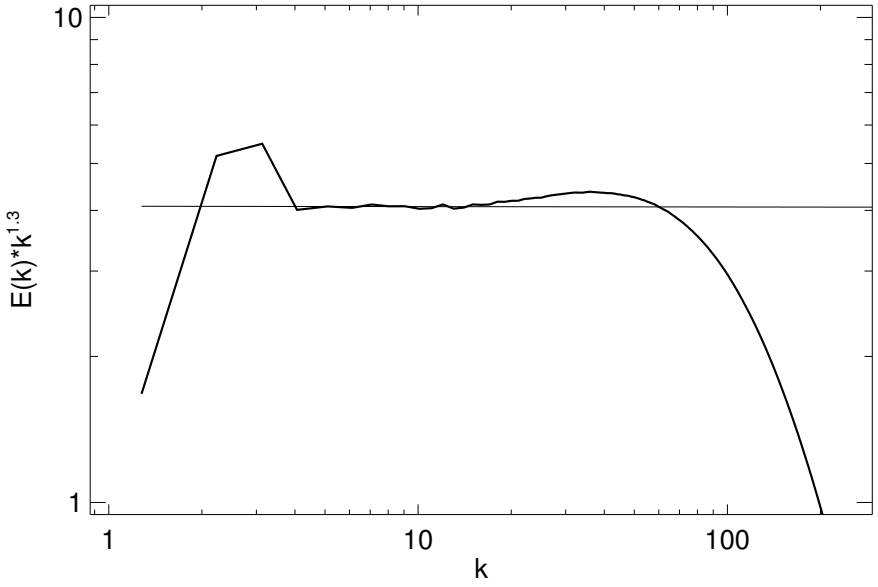

Fig. 6.35: Momentum-density power-spectrum, time-averaged over one flow-crossing time. At 1024^3-resolution, the injection range, the scaling range, and the near-dissipation bottleneck-range are clearly distinguished.

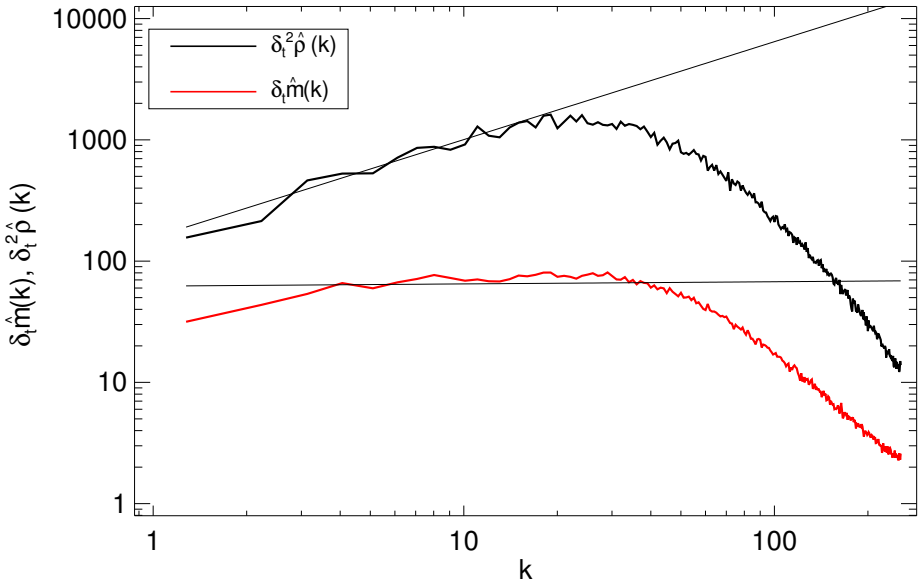

Fig. 6.36: Spectral shape of non-linear transfer to the momentum change and the second time-derivative of the mass-density in compressible supersonic and super-Alfvénic MHD-turbulence. The transfer terms are time-averaged and component-averaged. The sonic Mach number is $\mathcal{M}_\mathrm{s} \approx 4.5$, the Alfvén Mach number is $\mathcal{M}_\mathrm{A} \approx 1.5$. The straight lines represent power-law fits to the wave-number range $4 \leq k \leq 8$.

The analysis of the non-linear energy transfer in MHD turbulence is based on the k-shell integrated, absolute values of the Fourier-components described in equations (6.17) and (6.18). The snapshots of these wave-number dependent absolute values of the Fourier-components are time-averaged over several dynamical times of a statistically-stationary $\mathcal{M}_\mathrm{s} = 4.5$ and $\mathcal{M}_\mathrm{A} = 1.5$ MHD turbulence. In Figure 6.36, the resulting spectral distributions of the time-averaged transfer-terms are illustrated. The transfer to the mass-density term shows a higher amplitude over all spectral scales. In the range of power-law power-spectra $4 \leq k \leq 8$, the mass-density term exhibits an power-law increase in amplitude. The spectral shape of the obtained momentum term is flat in the according range of scales $4 \leq k \leq 8$. The results do not differ significantly from the $\mathcal{M}_\mathrm{s} = 4$ results of hydrodynamic turbulence. However, the ratio of the k-integrated total energy-transfer to mass-density over momentum-density (following equations (6.19) and (6.20)) is much smaller than in the hydrodynamic case. The ratio $\partial_t^2\hat{\rho}/\partial_t\hat{m}$ in MHD turbulence is approximately 15, while a value of approximately 30 is obtained in the hydrodynamic case of a comparable sonic Mach number of $\mathcal{M}_\mathrm{s} = 4$ (see Chapter 6.1.7). This smaller value of the ratio of non-linear energy transfer to mass-density fluctuations over momentum-density fluctuations may be related to the alignment of mass-density and magnetic pressure within compressible MHD waves. More energy is thus needed to excite mass-density fluctuations in MHD compared to hydrodynamics.
The flat shape of the non-linear energy-transfer to the momentum fluctuations indicates, that also in compressible MHD turbulence, the self-similar scaling of spectra results from a scale-independent non-linear energy transfer, governed by momentum-conservation.

7. CONCLUSION AND OUTLOOK

In this work, numerical studies of isotropic compressible turbulence in both magnetic and non-magnetic cases are presented. These numerical studies have been carried out using the KT-code, a solver for compressible hydrodynamics and MHD that has been developed in the course of this work. The numerical tools that the code employs are shock-capturing schemes for solving the ideal Euler gas equations and the compressible MHD equations. In high-resolution simulations, the KT-code has shown to efficiently compute the time evolution of compressible turbulence. At resolutions up to 1024^3, the time dynamics of the turbulent flows have been observed for multiple flow-crossing times. The numerical scheme has proved to yield power spectra with adequate scale separation, *i.e.* the separation of energy-injection scales from the bottleneck-affected near-dissipation scales. For scales between the injection and bottleneck scales, the large number of spectral snapshots that are taken lead to high statistics and thereby to low statistical uncertainty in the measurement of spectral scaling-exponents. The high-statistics property is enabled by computing power spectra at run time, which is a clear competitive advantage of the KT-code over established solvers presented in Chapter 4. One possible direction for future work is enlarging the spectral extent of power-law scaling ranges by replacing the Kurganov-Tadmor (KT) flux formulation by the Kurganov-Noelle-Petrova (KNP) flux formulation [38]. The KNP fluxes distinguish between right-hand and left-hand maximum speeds of propagation, unlike the KT fluxes that use the maximum of right-hand and left-hand speeds of propagation. This separation of left and right-hand speeds of propagation is already part of the KT-code, changing the flux formulation does not increase computational effort. The KNP flux formulation has proved to provide for lower numerical viscosity. Thereby, larger extents of self-similar scaling ranges of power spectra could be reached [77]. The time efficiency of the KT-code could be further improved, when 3D Fast-Fourier transformations (FFT) that are parallel in two spatial dimensions become available. Currently, a 1D-parallel 3D FFT is used. The 1D-parallel FFT limits the number of processes to the number of grid cells in one spatial dimension, and thus at maximum 1024 processes at 1024^3 resolution. A 2D-parallel 3D FFT would allow the number of processes to be increased further, thereby speeding-up the code, accordingly.

The results on isotropic hydrodynamic turbulence are largely in agreement with results of previous numerical studies of other groups. The velocity power-spectrum steepens with higher sonic Mach numbers, while the kinetic-energy spectrum flattens. The scaling-exponent of the power spectrum of the density-weighted velocity is not significantly influenced by the sonic Mach number of the turbulent flow. The resulting scaling-exponents were used to test the quantitative validity of the combined-Fleck model-predictions with a universal scaling-exponent for the density-weighted velocity. Although the results qualitatively exhibit the predicted steepening and flattening, the quantitative prediction by the parameter α, the degree of compression, is not supported by the results of this work.

Complementing numerical work of other groups, this work showed the systematic influence of the sonic Mach number on the scaling exponents of power spectra in the transonic to supersonic regime. The spectral scaling-exponents are shown to mainly change in the mildly-supersonic regime of $1 < \mathcal{M}_\mathrm{s} < 3$. From Mach numbers of 3 on, the scaling exponent for the velocity power-spectrum saturates to a value around $\beta = 2$. The velocity-power spectrum is dominated by rotational velocity. The ratio of the compressible part over the rotational part of the velocity fluctuations reaches a maximum value of $\chi \approx 0.3$ for the range of sonic Mach number $1 < \mathcal{M}_\mathrm{s} < 5.5$. The model view of a pure shock-turbulence, as suggested by the Burgers' turbulence, does thus not apply to solenoidally-driven supersonic turbulence.

This work also presents a new approach towards investigating the mechanisms that govern self-similar scaling in compressible hydrodynamic turbulence, based on momentum-density. The power spectra of momentum-density exhibit spectral scaling-ranges, and flatten considerably for higher sonic Mach numbers. This behavior is also observed for the power spectra of the mass-density. An analysis of the energy-transfer, induced by the non-linear term of the momentum equation, results in a scale independent, flat energy-transfer to momentum in the spectral range of self-similar power-spectra. A higher amount of energy is non-linearly transfered to density-fluctuations, showing a self-similar increase of transfered energy for smaller scales. In addition, the ratio of non-linearly transfered energy to mass-density fluctuations

over momentum-fluctuations increases with the sonic Mach number. This analysis provides insight into the reason for the flattening of density power-spectra at higher sonic Mach numbers.
Padoan's prediction of broadening mass-density PDFs at higher Mach numbers is supported by the numerical results obtained in this work. The obtained model parameter b was measured to be approximately 0.4, in agreement with results of other numerical studies of solenoidally-driven hydrodynamic turbulence. For future work, the systematic increase of the width of mass-density PDFs with the sonic Mach numbers might be investigated in compressibly-driven turbulence.
In statistically-stationary MHD turbulence, the influence of both the RMS sonic Mach number and the Alfvén Mach number on scaling exponents of power spectra have been investigated. All runs have been driven solenoidally. The numerical studies have been limited to isotropic, super-Alfvénic MHD turbulence. The MHD velocity power-spectra show a steeper spectral-scaling than in the non-magnetic case. Spectral scaling exponents are $\beta = 1.98(8)$ in the transonic regime, and $\beta = 2.29(7)$ in the supersonic regime at $\mathcal{M}_\mathrm{s} \approx 5$. We have shown that like in the non-magnetic case, an increase of the sonic Mach number of the flow leads to a steepening of velocity power-spectra within the power-law scaling-range. Another similarity to the non-magnetic case is the flattening of kinetic-energy spectra with increasing sonic Mach numbers. The obtained scaling exponents of the kinetic-energy spectra change from $\beta = 1.78(7)$ at $\mathcal{M}_\mathrm{s} \approx 1.6$ to $\beta = 1.64(7)$ at $\mathcal{M}_\mathrm{s} \approx 4.8$. The scaling exponent of the density-weighted velocity power-spectrum is not significantly influenced by the sonic Mach number. It is $\beta \approx 1.89(8)$, significantly steeper than the scaling exponent of $\beta \approx 1.66$, reported by Kowal and Lazarian in [34]. These scaling exponents show properties similar to those in the non-magnetic case, but steeper. The total energy scales with a scaling exponent of $\beta \approx 1.5$, independently of the sonic Mach number and the Alfvén Mach number. The scaling exponent of the total energy shows an interesting agreement with the prediction of the Iroshnikov-Kraichnan theory for incompressible MHD turbulence.
The scaling of the residual energy is strongly influenced by the parameters $\mathcal{M}_\mathrm{s}$ and $\mathcal{M}_\mathrm{A}$ and the according ratio of kinetic energy over magnetic energy of the turbulent fluctuations. In the non-magnetic limit, the residual energy is determined only by the kinetic energy. The scaling exponent of the residual energy increases with a higher contribution of the magnetic energy to the total energy. Unlike in incompressible MHD turbulence, compressible MHD turbulence does not yield a universal power-law for the residual energy. The residual-energy scaling in compressible MHD is strongly influenced by the parameters $\mathcal{M}_\mathrm{s}$ and $\mathcal{M}_\mathrm{A}$.
The systematic measurement of the mass-density PDFs in compressible MHD turbulence, subject to varying $\mathcal{M}_\mathrm{s}$ and $\mathcal{M}_\mathrm{A}$, has resulted in mainly two findings: (1.) The width of the logarithmic density PDF increases with the sonic Mach number of the turbulence. The model parameter $b = 0.36(3)$ of equation (6.12) is slightly smaller than in non-magnetic turbulence. The compression induced by MHD turbulence is smaller than the compression in pure hydrodynamic turbulence. (2.) The width of the logarithmic density PDF also depends on the relative strength of the magnetic-field fluctuations, parametrized by $\mathcal{M}_\mathrm{A}$. It was shown that the width of the density PDF decreases linearly with the inverse of the Alfvén Mach number $1/\mathcal{M}_\mathrm{A}$, in a first-order model approximation.
In compressible MHD turbulence, both the density power-spectrum and the momentum power-spectrum exhibit power-law scaling. The scaling exponents of the density power-spectra decrease at higher sonic Mach numbers. A flattening of power spectra with higher sonic Mach numbers is also observed for momentum-density. The power spectra of momentum-density in the 1024^3-run at $\mathcal{M}_\mathrm{s} \approx 3.0$ and $\mathcal{M}_\mathrm{A} \approx 1.6$ reveal a low statistical deviation from power-law scaling within the range of spectral wave-numbers $4 \leq k \leq 14$. In addition, a clear separation of the injection scales from the near-dissipations range bottleneck-scales is observed in power spectra from the 1024^3-run.
In both the hydrodynamic and MHD cases, the non-linear energy transfer to momentum-density and mass-density has been measured in statistically-stationary turbulence. In MHD, the non-linear energy-transfer to momentum density, induced by both the non-linear momentum term and the non-linear magnetic-field term of equation (2.118), shows a flat, scale-independent spectral-shape in the range of power-law scaling. However, the non-linear energy-transfer to density-fluctuation shows a power-law increase with the wave-number k, until dissipation dampens the transfer. The obtained energy transfers in MHD turbulence correspond to those obtained in hydrodynamic turbulence. The main difference is the ratio of non-linearly transfered energy to the density fluctuations over the momentum fluctuations. In MHD, this ratio is considerably smaller than in the pure hydrodynamic case.
The results of power-law behavior of the momentum power-spectra, combined with a flat and scale-independent non-linear energy transfer to momentum-fluctuations suggest that the cascade in compressible turbulence is governed by non-linear momentum conservation. This result reflects the main difference

to incompressible turbulence, where energy conservation governs the turbulent cascade. The momentum-based cascade in compressible turbulence might be key to understand, why power-law behavior is observed in compressible turbulence, even though the argument of detailed conservation of kinetic energy, or total energy, is lost by compression.
The next logical step to gain more insight into compressible-turbulence properties would be a variation in the forcing method. All results presented in this work are based on solenoidally-driven turbulence. In recently published work, compressional driving of the velocity has shown to change the degree of compression in turbulent hydrodynamic flows tremendously (see [24]). It would be interesting to see whether this higher degree of compression, manifested in much broader density PDFs, affects the scaling properties of power spectra. The KT simulation-code is already equipped with the possibility of compressible forcing. The presented campaigns that measure the systematic influence of the sonic Mach number and the Alfvén Mach number on scaling properties can thus be repeated using compressional forcing of velocity fluctuations.
For future work, the restriction to the isothermal case, which has been chosen for this work, should be abolished. This restriction to isothermality inhibits several physical effects that are likely to change the statistical-ensemble behavior of compressible turbulence. These effects include *e.g.* coupling of momentum-fluctuations to thermal fluctuations and baroclinic vorticity generation [22]. The necessary extensions to the KT simulation-code are small, versions with an adiabatic equation of state have already been implemented and tested. To keep the turbulence in a statistical stationary state, the simulation codes will have to be supplemented by an adequate cooling function. In addition, the simulation codes can be used to simulate compressible convective turbulence.

APPENDIX

A. SIMULATION CODE, FLOW-CHARTS AND ROUTINE DESCRIPTION

This Appendix gives a brief overview of the implementation of the compressible MHD simulation code. The code itself is relatively short. The whole implementation entails only 5000 lines of Fortran90 code. The main Kurganov-Tadmor algorithm spans over approximately 1000 lines of source code. Here, flow charts of the main program and the main numerical algorithms are presented. In addition, the organization of the data dumps and the location and meaning of free parameters are described. This appendix is thus primarily addressing scientists, who will work with the KT-MHD code. The main program and the subroutines are spread over two source-code files:

- `MHD3P.f90`: Main program and power-spectra computation
- `P_KT_3D.f90`: Time-evolution by Runge-Kutta and evaluation of numerical fluxes (Kurganov-Tadmor), plus IO routines and forcing

The main program and the subroutines, with a short description, as follows:

- `Program MHD_3DP`: Main program, 3D and MPI parallel
- `subroutine MHD3D_KT_3rd:`computes the time evolution of the conserved quantities using the third order Runge Kutta scheme
- `subroutine du_dt`: approximates the total time derivative of the conserved quantities by approximating point values from cell averages in the three space dimensions
- `subroutine comp_flux_x`: computes the fluxes for the MHD equations in x-direction as well as the maximum speed of propagation in x
- `subroutine comp_flux_y`: computes the fluxes for the MHD equations in y-direction as well as the maximum speed of propagation in y
- `subroutine comp_flux_z`: computes the fluxes for the MHD equations in z-direction as well as the maximum speed of propagation in z
- `subroutine comp_weights`: computes the non-linear weights of the CWENO point value reconstruction
- `subroutine set_boundary`: sets the 3D periodic boundary conditions
- `subroutine file_put`: dumps the full data cube in raw format and the meta file, formatted
- `subroutine file_meta_read`: reads the meta file when restart from dump
- `subroutine file_data_read`: reads the raw data cube of a frame
- `subroutine file_put_single`: dumps the projection of the maximum of a scalar field along the x-axis to a file, raw data; for visualization purposes
- `subroutine file_put_spectrum`: dumps formatted 1D power spectrum as a text file
- `subroutine get_force_field`: computes the random force-field via an Ornstein-Uhlenbeck process
- `subroutine read_force_field`: reads the force field from frame dump, text file
- `subroutine write_force_field`: force-field frame-dump, text file
- `subroutine compute_energy`: computes the mean total energy, kinetic energy, magnetic energy, rms Mach number, rms Alfvén Mach number

- `subroutine file_put_energy`: write the above computed mean energy and Mach number values to a formatted text file
- `subroutine compute_fftw`: computes the Fourier transform of fields and computes the 1D power-spectrum

The top-level flow-chart, shown in Figure A.1, depicts the execution of the KT-code from a higher level perspective. It consists of two nested time-loops. After every step of the outer loop, full data dumps are written. After each step of the inner loop, spectral diagnostics, density PDFs, and average values (of *e.g.* Mach number, kinetic energy, magnetic energy) are written. Within the inner loop, the main numerical algorithm is invoked. This main numerical algorithm is the Runge-Kutta time evolution of the fields (`subroutine MHD3D_KT_3rd`). In the Runge-Kutta subroutine, the fields are evolved in time. The time evolution in one time step calls the evaluation routine of the right-hand side of equations (3.1) and (3.16), named `subroutine du_dt`. `Subroutine du_dt` is called three times within one discrete time step, since the Runge Kutta scheme is of the 3rd order.
At each time step, the forcing fields for kinetic-energy and magnetic-energy injection are computed. The force field, following the Ornstein-Uhlenbeck process described in Chapter 3.2, are computed in the subroutine `Subroutine get_force_field`.

A.1 Main parameters

The main parameters in the KT-code are defined in the module file `module K_T_parameters`. This module is used in most of the subroutines. The following parameters can be set in the module file:

- `nx`, `ny`, `nz`: Spatial resolution, that means number of grid points in x-, y-, and z-direction. Any combination of {`nx`, `ny`, `nz`}=2^n, with n={4,5,6,7,8,9,10} works.
- `mn`: Number of conserved quantities. In isothermal MHD, it is 7 (density, momentum in x, momentum in y, momentum in z, x-component of magnetic field, y-component of magnetic field, z-component of magnetic field).
- `md`: Number of ghost cells. In isothermal MHD, minimum is 4. In hydro, minimum is 2.
- `IO`: Switch for restart on data dump / restart with initial conditions.
- `procs`: Number of MPI processes.
- `proc_y`: Number of processes in y-direction.
- `proc_z`: Number of processes in z-direction. Make sure `proc_y` $\cdot$ `proc_z` = `procs`.
- `factor`: Parameter for restart on smaller resolution data dumps. When doubling the resolution on an existing data dump, set this switch to 2. When data dump resolution is equal to the computation resolution, set this switch to 1.
- `fac_proc_y`: Parameter for restart with more processes. When doubling the number of processes in y-direction on an existing data dump, set this switch to 2. When the number of processes of the computation is the same as the data dump, set it to 1.
- `fac_proc_z`: Parameter for restart with more processes. When doubling the number of processes in z-direction on an existing data dump, set this switch to 2. When the number of processes of the computation is the same as the data dump, set it to 1.

In addition to the parameters of the module file, some parameters are defined in the main program and in subroutines. The important parameters in the main program are:

- `time_steps`: Number of inner loops per outer loop. Is determined by `intervall_2`/ `invervall`.
- `intervall_2`: Time-interval of full data dumps, in units of the constant sound speed.
- `intervall`: Time-interval of spectral diagnostics, in units of the constant sound speed.
- `soundspeed`: Constant, isothermal sound speed

Other important parameters are spread across the subroutines, where they are required. The most important parameters are:

- `cfl`: located in `subroutine du_dt`, Courant number for dynamic time-step allocation
- `w_epsilon`, `c_left`, `c_right,c_central`: located in `subroutine comp_weights`, weights of the CWENO scheme, see equation (3.7)
- `F_0`, `F_0_mag`, `spectral_weight`: located in `subroutine get_force_field`, amplitudes of the kinetic-energy force, the magnetic-energy force, and the solenoidal over compressible weight of the kinetic-energy force.

A.2 Files

Finally, the files written in full data dumps are described. For each full data dump, a meta file and the full real-space fields of the conserved quantities are dumped. The meta file contains header information such as the current time, the resolution and the number of processes. Only process 0 writes the meta file. The real-space fields are dumped by each process, individually. The distribution of the fields over the processes is described in Chapter 4.1. In isothermal MHD, seven times the number of processes files are dumped at each snapshot. The naming convention is:

- 'meta'+time(F7.2)+'.dat': meta file
- 'rho_'+process number(I4)+'_'+time(F7.2)+'.dat': mass-density
- 'xmt_'+process number(I4)+'_'+time(F7.2)+'.dat': momentum, x-component
- 'ymt_'+process number(I4)+'_'+time(F7.2)+'.dat': momentum, y-component
- 'zmt_'+process number(I4)+'_'+time(F7.2)+'.dat': momentum, z-component
- 'bx_'+process number(I4)+'_'+time(F7.2)+'.dat': magnetic-field, x-component
- 'by_'+process number(I4)+'_'+time(F7.2)+'.dat': magnetic-field, y-component
- 'bz_'+process number(I4)+'_'+time(F7.2)+'.dat': magnetic-field, z-component

In addition to the full data dumps, density PDFs and power spectra are written to text files.

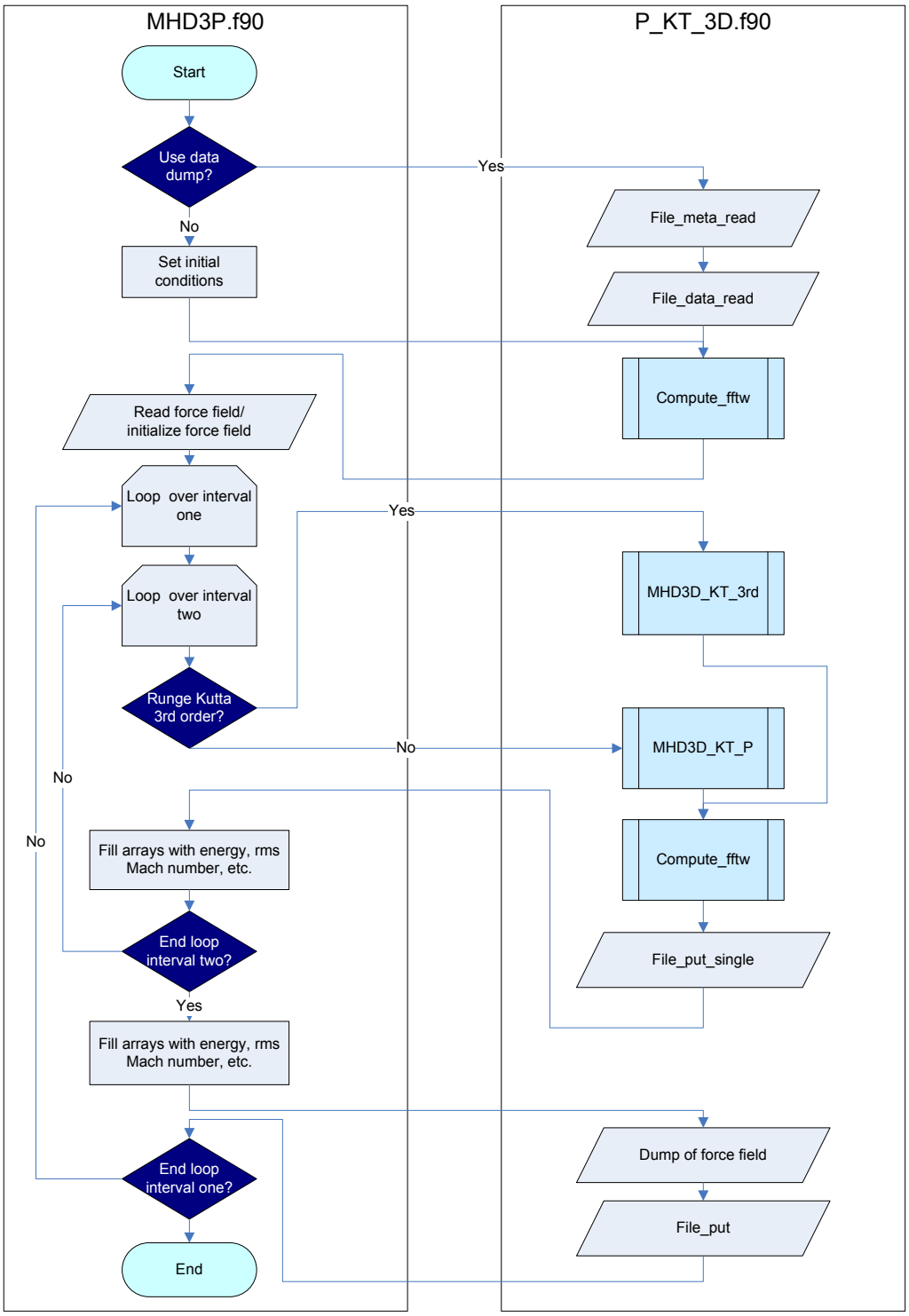

Fig. A.1: Flow chart top-level view.

B. GHOST-CELL COMPUTATION

The usage of ghost-cells differs between the hydro KT code and the MHD-KT code. The reason for the difference and a detailed explanation of the ghost-cell computation is provided in this Appendix.
In central-difference schemes, the update of the edge-located grid cells requires information of their surrounding neighbor cells. In parallel codes, the computational domain is distributed over a number of processes. Within one process, a certain number of ghost-cells are locally added to the grid in order to provide this neighboring grid-cell information for the central difference of the first real grid cell. The required number of ghost-cells depends on the length of the numerical stencil, that means the local reach of the numerical scheme from the perspective of an updated grid-cell. In Figure B.1 a floor-plan of real grid cells and their surrounding ghost-cells is depicted for a 2D grid. In the hydro case, the first real grid cell (0,0) is updated in the x-direction *via* the finite difference of the edge-located numerical fluxes $\mathbf{H}_{-1/2,0}$ and $\mathbf{H}_{+1/2,0}$. The numerical flux vector $\mathbf{H}_{-1/2,0}$ is computed from point values $\mathbf{u}^{\mathrm{East}}_{-1,0}$ and $\mathbf{u}^{\mathrm{West}}_{0,0}$. For the reconstruction of the most 'West'-located point value, $\mathbf{u}^{\mathrm{East}}_{-1,0}$, the cell averages $\bar{\mathbf{u}}_{-2,0}$, $\bar{\mathbf{u}}_{-1,0}$, and $\bar{\mathbf{u}}_{0,0}$ are used (see computation of $\mathbf{u}^{\mathrm{East}}_{-1,0}$ of equation (3.14)). For the update of cell average at (0,0), the local reach of the numerical scheme extends to the grid cell (-2,0), to the left hand side. As the scheme is central-in-space, this reach, and thus the length of the numerical stencil, is 2 grid cells in all spatial directions, in the hydrodynamic case. This length of 2 of the numerical stencil determines the number of ghost-cells, that added around the real computational grid for each process.

In the MHD-KT code, the constrained transport method enlarges the numerical stencil. The source

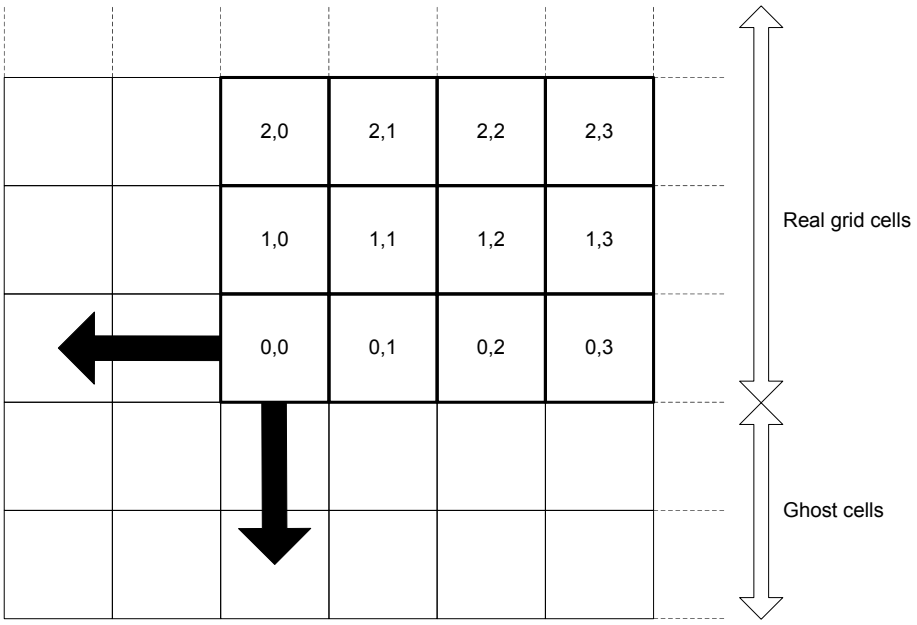

Fig. B.1: 2D floor-plan of the grid cells within one process. The real computation grid cells are surrounded by ghost cells. The numerical stencil, the black marked vector that starts at grid cell 0,0, reaches over two cells. The values of the grid cells are the copied values of the neighboring processes real-grid cells.

of this is the 2^{nd} order interpolation of the edge-centered electric-field components (3.21)-(3.23) from interface-located electric-field flux vectors. A lower-order interpolation method reduces the size of the numerical stencil, but has shown to decrease the order of convergence of the complete hybrid scheme. The 2^{nd} order interpolation is a compromise between the order of convergence, a meadure of the accuracy of

the scheme, and the numerical viscosity, slightly enlarged by the increased length of the numerical stencil. The values of the ghost cells are set before each Runge-Kutta step. The values of the first real grid cells of the neighboring process are copied to the ghost-cells. In Figure B.2, the copying process is depicted.

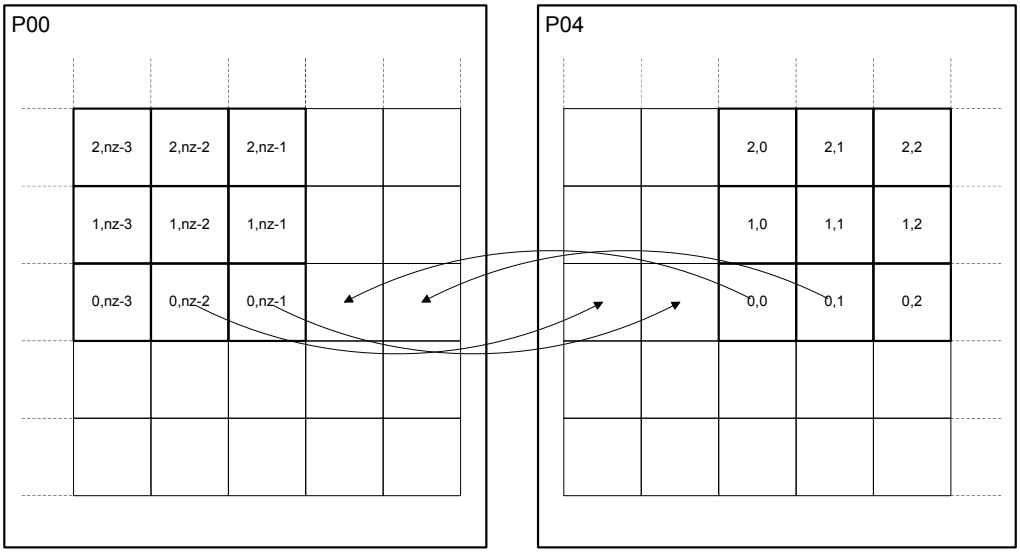

Fig. B.2: Two neighboring processes exchange edge-located grid cell information before each Runge-Kutta step. In this example, P00 and P04 are neighbors in z-direction. The copying process is exemplified by the arrows for two ghost cells in each process.

BIBLIOGRAPHY

[1] A. Arneodo, C. Baudet, F. Belin, R. Benzi, B. Castaing, B. Chabaud, R. Chavarria, S. Ciliberto, R. Camussi, F. Chillà, B. Dubrulle, Y. Gagne, B. Hebral, J. Herweijer, M. Marchand, J. Maurer, J. F. Muzy, A. Naert, A. Noullez, J. Peinke, F. Roux, P. Tabeling, W. van de Water, and H. Willaime. Structure functions in turbulence, in various flow configurations, at Reynolds number between 30 and 5000, using extended self-similarity. *Europhysics Letters*, 34:411–416, May 1996.

[2] J. Balbás and E. Tadmor. Nonoscillatory central schemes for one- and two-dimensional magnetohydrodynamics equations. ii: High-order semidiscrete schemes. *SIAM J. Sci. Comput.*, 28(2):533–560, 2006.

[3] J. Ballesteros-Paredes, R. S. Klessen, M.-M. Mac Low, and E. Vazquez-Semadeni. Molecular Cloud Turbulence and Star Formation. *Protostars and Planets V*, pages 63–80, 2007.

[4] F. Bensch, J. Stutzki, and V. Ossenkopf. Quantification of molecular cloud structure using the Delta -variance. *Astronomy and Astrophysics*, 366:636–650, February 2001.

[5] D. Biskamp. *Magnetohydrodynamic Turbulence*. Cambridge University Press, Cambridge, 2003.

[6] D. Biskamp and H. Welter. Dynamics of decaying two-dimensional magnetohydrodynamic turbulence. *Physics of Fluids B: Plasma Physics*, 1(10):1964–1979, 1989.

[7] S. Boldyrev. Kolmogorov-Burgers Model for Star-forming Turbulence. *The Astrophysical Journal*, 569:841–845, April 2002.

[8] S. Boldyrev, P. Padoan, R. Jimenez, and Å. Nordlund. Scaling Relations of Supersonic Turbulence in Molecular Clouds. *Astrophysics and Space Science*, 292:61–68, August 2004.

[9] A. Brandenburg and K. Subramanian. Astrophysical magnetic fields and nonlinear dynamo theory. *Physics Reports*, 417:1–209, October 2005.

[10] R. Bruno and V. Carbone. The Solar Wind as a Turbulence Laboratory. *Living Reviews in Solar Physics*, 2:4–188, September 2005.

[11] A. Busse. *Lagrangesche statistische Eigenschaften hydrodynamischer und magnetohydrodynamischer Turbulenz*. PhD thesis, Universität Bayreuth, 2009.

[12] A. Chepurnov, A. Lazarian, S. Stanimirović, C. Heiles, and J. E. G. Peek. Velocity Spectrum for H I at High Latitudes. *The Astrophysical Journal*, 714:1398–1406, May 2010.

[13] J. Cho and A. Lazarian. Compressible magnetohydrodynamic turbulence: mode coupling, scaling relations, anisotropy, viscosity-damped regime and astrophysical implications. *Monthly Notices of the RAS*, 345:325–339, October 2003.

[14] James W. Cooley and John W. Tukey. An algorithm for the machine calculation of complex fourier series. *Mathematics of Computation*, 19(90):297–301, 1965.

[15] J. Crovisier and J. M. Dickey. The spatial power spectrum of galactic neutral hydrogen from observations of the 21-cm emission line. *Astronomy and Astrophysics*, 122:282–296, June 1983.

[16] A. A. Deshpande, K. S. Dwarakanath, and W. M. Goss. Power Spectrum of the Density of Cold Atomic Gas in the Galaxy toward Cassiopeia A and Cygnus A. *The Astrophysical Journal*, 543:227–234, November 2000.

[17] J. M. Dickey, N. M. McClure-Griffiths, S. Stanimirović, B. M. Gaensler, and A. J. Green. Southern Galactic Plane Survey Measurements of the Spatial Power Spectrum of Interstellar H I in the Inner Galaxy. *The Astrophysical Journal*, 561:264–271, November 2001.

[18] J. Dreher and R. Grauer. Racoon: a parallel mesh-adaptive framework for hyperbolic conservation laws. *Parallel Comput.*, 31(8+9):913–932, 2005.

[19] B. Dubrulle. Intermittency in fully developed turbulence: Log-Poisson statistics and generalized scale covariance. *Physical Review Letters*, 73:959–962, August 1994.

[20] B. G. Elmegreen, D. M. Elmegreen, and S. N. Leitner. A Turbulent Origin for Flocculent Spiral Structure in Galaxies. *The Astrophysical Journal*, 590:271–283, June 2003.

[21] B. G. Elmegreen, S. Kim, and L. Staveley-Smith. A Fractal Analysis of the H I Emission from the Large Magellanic Cloud. *The Astrophysical Journal*, 548:749–769, February 2001.

[22] B. G. Elmegreen and J. Scalo. Interstellar turbulence i: Observations and processes. *Annual Review of Astronomy and Astrophysics*, 42:211–273, September 2004.

[23] G. Falkovich. Bottleneck phenomenon in developed turbulence. *Physics of Fluids*, 6:1411–1414, April 1994.

[24] C. Federrath, R. S. Klessen, and W. Schmidt. The Density Probability Distribution in Compressible Isothermal Turbulence: Solenoidal versus Compressive Forcing. *The Astrophysical Journal*, 688:L79–L82, December 2008.

[25] R. C. Fleck, Jr. Scaling Relations for the Turbulent, Non–Self-gravitating, Neutral Component of the Interstellar Medium. *Astrophysical Journal*, 458:739–741, February 1996.

[26] U. Frisch. *Turbulence: The Legacy of A.N. Kolmogorov*. Cambdridge University Press, 1995.

[27] B. Fryxell, K. Olson, P. Ricker, F. X. Timmes, M. Zingale, D. Q. Lamb, P. MacNeice, R. Rosner, J. W. Truran, and H. Tufo. FLASH: An Adaptive Mesh Hydrodynamics Code for Modeling Astrophysical Thermonuclear Flashes. *The Astrophysical Journal, Supplement*, 131:273–334, November 2000.

[28] B. Galanti and A. Tsinober. Is turbulence ergodic? *Physics Letters A*, 330(3-4):173–180, 2004.

[29] P. Goldreich and S. Sridhar. Toward a theory of interstellar turbulence. 2: Strong alfvenic turbulence. *Astrophysical Journal*, 438:763–775, January 1995.

[30] M. H. Heyer and C. M. Brunt. The Universality of Turbulence in Galactic Molecular Clouds. *Astrophysical Journal, Letters*, 615:L45–L48, November 2004.

[31] P. S. Iroshnikov. Turbulence of a Conducting Fluid in a Strong Magnetic Field. *Soviet Astronomy*, 7:568, February 1964.

[32] S. Kida. Asymptotic properties of Burgers turbulence. *Journal of Fluid Mechanics*, 93:337–377, July 1979.

[33] A. N. Kolmogorov. A refinement of previous hypotheses concerning the local structure of turbulence in a viscous incompressible fluid at high Reynolds number. *Journal of Fluid Mechanics*, 13:82–85, 1962.

[34] G. Kowal and A. Lazarian. Scaling Relations of Compressible MHD Turbulence. *Astrophysical Journal, Letters*, 666:L69–L72, September 2007.

[35] R. H. Kraichnan. Inertial-Range Spectrum of Hydromagnetic Turbulence. *Physics of Fluids*, 8:1385–1387, July 1965.

[36] A. G. Kritsuk, M. L. Norman, P. Padoan, and R. Wagner. The Statistics of Supersonic Isothermal Turbulence. *Astrophysical Journal*, 665:416–431, August 2007.

[37] A. G. Kritsuk, S. D. Ustyugov, M. L. Norman, and P. Padoan. Simulations of Supersonic Turbulence in Molecular Clouds: Evidence for a New Universality. 406:15–22, April 2009.

[38] A. Kurganov, S. Noelle, and G. Petrova. Semi-discrete central-upwind schemes for hyperbolic conservation laws and hamilton-jacobi equations. *SIAM J. Sci. Comput*, 23:707–740, 2000.

[39] A. Kurganov and E. Tadmor. New High-Resolution Central Schemes for Nonlinear Conservation Laws and Convection-Diffusion Equations. *Journal of Computational Physics*, 160:241–282, May 2000.

[40] M. Lesieur. *Turbulence in fluids*. Kluwer Academic Publishers, Dordrecht, 1997. Includes bibliographical references and index.

[41] D. Levy, G. Puppo, and G. Russo. Central weno schemes for hyperbolic systems of conservation laws. *M2AN*, 33(3):547–571, may 1999.

[42] P. S. Li, C. F. McKee, R. I. Klein, and R. T. Fisher. Sub-Alfvénic Nonideal MHD Turbulence Simulations with Ambipolar Diffusion. I. Turbulence Statistics. *The Astrophysical Journal*, 684:380–394, September 2008.

[43] P. S. Li, M. L. Norman, M.-M. Mac Low, and F. Heitsch. The Formation of Self-Gravitating Cores in Turbulent Magnetized Clouds. *The Astrophysical Journal*, 605:800–818, April 2004.

[44] M. J. Lighthill. The Effect of Compressibility on Turbulence. In *Gas Dynamics of Cosmic Clouds*, volume 2 of *IAU Symposium*, pages 121–130, 1955.

[45] Y. Q. Lou, R. Rosner, and P. Ulmschneider. A computational code for two-dimensional unsteady magnetohydrodynamics by the method of characteristics. *Astrophysical Journal*, 315:349–370, April 1987.

[46] F. J. Low, E. Young, D. A. Beintema, T. N. Gautier, C. A. Beichman, H. H. Aumann, F. C. Gillett, G. Neugebauer, N. Boggess, and J. P. Emerson. Infrared cirrus - New components of the extended infrared emission. *Astrophysical Journal, Letters*, 278:L19–L22, March 1984.

[47] M.-M. Mac Low, R. S. Klessen, A. Burkert, and M. D. Smith. Kinetic energy decay rates of supersonic and super-alfvénic turbulence in star-forming clouds. *Phys. Rev. Lett.*, 80(13):2754–2757, Mar 1998.

[48] A. Mignone. A simple and accurate Riemann solver for isothermal MHD. *Journal of Computational Physics*, 225:1427–1441, August 2007.

[49] W.-C. Müller and D. Biskamp. Scaling Properties of Three-Dimensional Magnetohydrodynamic Turbulence. *Physical Review Letters*, 84:475–478, January 2000.

[50] W.-C. Müller and R. Grappin. Spectral energy dynamics in magnetohydrodynamic turbulence. *Phys. Rev. Lett.*, 95(11):114502, Sep 2005.

[51] M. L. Norman. Introducing ZEUS-MP: A 3D, Parallel, Multiphysics Code for Astrophysical Fluid Dynamics. In S. J. Arthur, N. S. Brickhouse, & J. Franco, editor, *Revista Mexicana de Astronomia y Astrofisica Conference Series*, volume 9 of *Revista Mexicana de Astronomia y Astrofisica Conference Series*, pages 66–71, May 2000.

[52] NATO Advanced Study Institute on the Physics of Star Formation, Early Stellar Evolution, Charles J. Lada, and N. Kylafis. *The physics of star formation and early stellar evolution / edited by Charles J. Lada and Nikolaos D. Kylafis*. Kluwer Academic, Dordrecht ; Boston :, 1991.

[53] B. W. O'Shea, G. Bryan, J. Bordner, M. L. Norman, T. Abel, R. Harkness, and A. Kritsuk. Introducing Enzo, an AMR Cosmology Application. *ArXiv Astrophysics e-prints*, March 2004.

[54] P. Padoan, R. Jimenez, Å. Nordlund, and S. Boldyrev. Structure Function Scaling in Compressible Super-Alfvénic MHD Turbulence. *Physical Review Letters*, 92(19):191102, May 2004.

[55] P. Padoan, B. J. T. Jones, and A. P. Nordlund. Supersonic Turbulence in the Interstellar Medium: Stellar Extinction Determinations as Probes of the Structure and Dynamics of Dark Clouds. *Astrophysical Journal*, 474:730–734, January 1997.

[56] P. Padoan and Å. Nordlund. A Super-Alfvénic Model of Dark Clouds. *Astrophysical Journal*, 526:279–294, November 1999.

[57] P. Padoan, Å. Nordlund, A. G. Kritsuk, M. L. Norman, and P. S. Li. Two Regimes of Turbulent Fragmentation and the Stellar Initial Mass Function from Primordial to Present-Day Star Formation. *The Astrophysical Journal*, 661:972–981, June 2007.

[58] T. Passot, A. Pouquet, and P. Woodward. The plausibility of Kolmogorov-type spectra in molecular clouds. *Astronomy and Astrophysics*, 197:228–234, May 1988.

[59] D. Porter, A. Pouquet, and P. Woodward. Measures of intermittency in driven supersonic flows. *Phys. Rev. E*, 66(2):026301, Aug 2002.

[60] D. J. Price and C. Federrath. A comparison between grid and particle methods on the statistics of driven, supersonic, isothermal turbulence. *ArXiv e-prints*, April 2010.

[61] D. J. Schlegel, D. P. Finkbeiner, and M. Davis. Maps of Dust Infrared Emission for Use in Estimation of Reddening and Cosmic Microwave Background Radiation Foregrounds. *The Astrophysical Journal*, 500:525, June 1998.

[62] W. Schmidt, W. Hillebrandt, and J. C. Niemeyer. Numerical dissipation and the bottleneck effect in simulations of compressible isotropic turbulence. *Computers & Fluids*, 35(4):353–371, 2006.

[63] R. A. Shaw. Particle-turbulence interactions in atmospheric clouds. *Annual Review of Fluid Mechanics*, 35(1):183–227, 2003.

[64] J. V. Shebalin, W. H. Matthaeus, and D. Montgomery. Anisotropy in MHD turbulence due to a mean magnetic field. *Journal of Plasma Physics*, 29:525–547, June 1983.

[65] B. K. Shivamoggi. Spectral laws for the compressible isotropic turbulence. *Physics Letters A*, 166(3-4):243–248, 1992.

[66] B. K. Shivamoggi. Magnetohydrodynamic turbulence: Generalized formulation and extension to compressible cases. *Annals of Physics*, 323(6):1295–1303, 2008.

[67] F. H. Shu. *Physics of Astrophysics, Vol. II.* University Science Books, 1992.

[68] K. R. Sreenivasan. On the universality of the Kolmogorov constant. *Physics of Fluids*, 7:2778–2784, November 1995.

[69] S. Sridhar and P. Goldreich. Toward a theory of interstellar turbulence. 1: Weak Alfvenic turbulence. *Astrophysical Journal*, 432:612–621, September 1994.

[70] R. Teyssier. Cosmological hydrodynamics with adaptive mesh refinement. A new high resolution code called RAMSES. *Astronomy and Astrophysics*, 385:337–364, April 2002.

[71] G. Tóth. The div b = 0 constraint in shock-capturing magnetohydrodynamics codes. *J. Comput. Phys.*, 161(2):605–652, 2000.

[72] E. Vazquez-Semadeni. Hierarchical Structure in Nearly Pressureless Flows as a Consequence of Self-similar Statistics. *Astrophysical Journal*, 423:681–692, March 1994.

[73] M. K. Verma. Statistical theory of magnetohydrodynamic turbulence: recent results. *Physics Reports*, 401:229–380, November 2004.

[74] C. F. von Weizsäcker. The Evolution of Galaxies and Stars. *Astrophysical Journal*, 114:165–186, September 1951.

[75] K. Yoshida and T. Arimitsu. Inertial-subrange structures of isotropic incompressible magnetohydrodynamic turbulence in the lagrangian renormalized approximation. *Physics of Fluids*, 19(4):045106, 2007.

[76] Y. T. Zhang, J. Shi, C. W. Shu, and Y. Zhou. Numerical viscosity and resolution of high-order weighted essentially nonoscillatory schemes for compressible flows with high reynolds numbers. *Phys. Rev. E*, 68(4):046709, Oct 2003.

[77] U. Ziegler. personal correspondence. *MHD days 2009, Potsdam.*

[78] U. Ziegler. A central-constrained transport scheme for ideal magnetohydrodynamics. *J. Comput. Phys.*, 196(2):393–416, 2004.

ACKNOWLEDGEMENTS

This work was supported by the DFG cluster of excellence "Origin and Structure of the Universe" (www.universe-cluster.de). It is a pleasure to thank those who supported me during the three years of my PhD. I would like to thank:

- Priv. Doz. Dr. Wolf-Christian Müller-Nutzinger for supervision, good suggestions, and fruitful discussions
- Prof. Sibylle Günter for the opportunity to carry out this thesis at IPP, as well as for her support and feedback
- Prof. Andreas Burkert for undertaking the PhD correction task
- All my collegues of the Junior Research group, with special thanks to Jane Pratt, Angela Busse, and Dan Škandera
- Viola, for her patience, her consideration, and her appreciation
- My family, for encouragment and assistence
- All my friends, for enduring me during tough times